Tuning CeO_2 Particle Size in Ni/CeO_2 for CO_2 Methanation

Master's Thesis

Author
Aurielle Margareth Tioli Simitro 2384892

Supervisors
Dr. Zhang ShuChi
Dr. N.A. Kosinov
Dr. Samir Bensaid

Graduation Committee
Dr. Ivo Filot

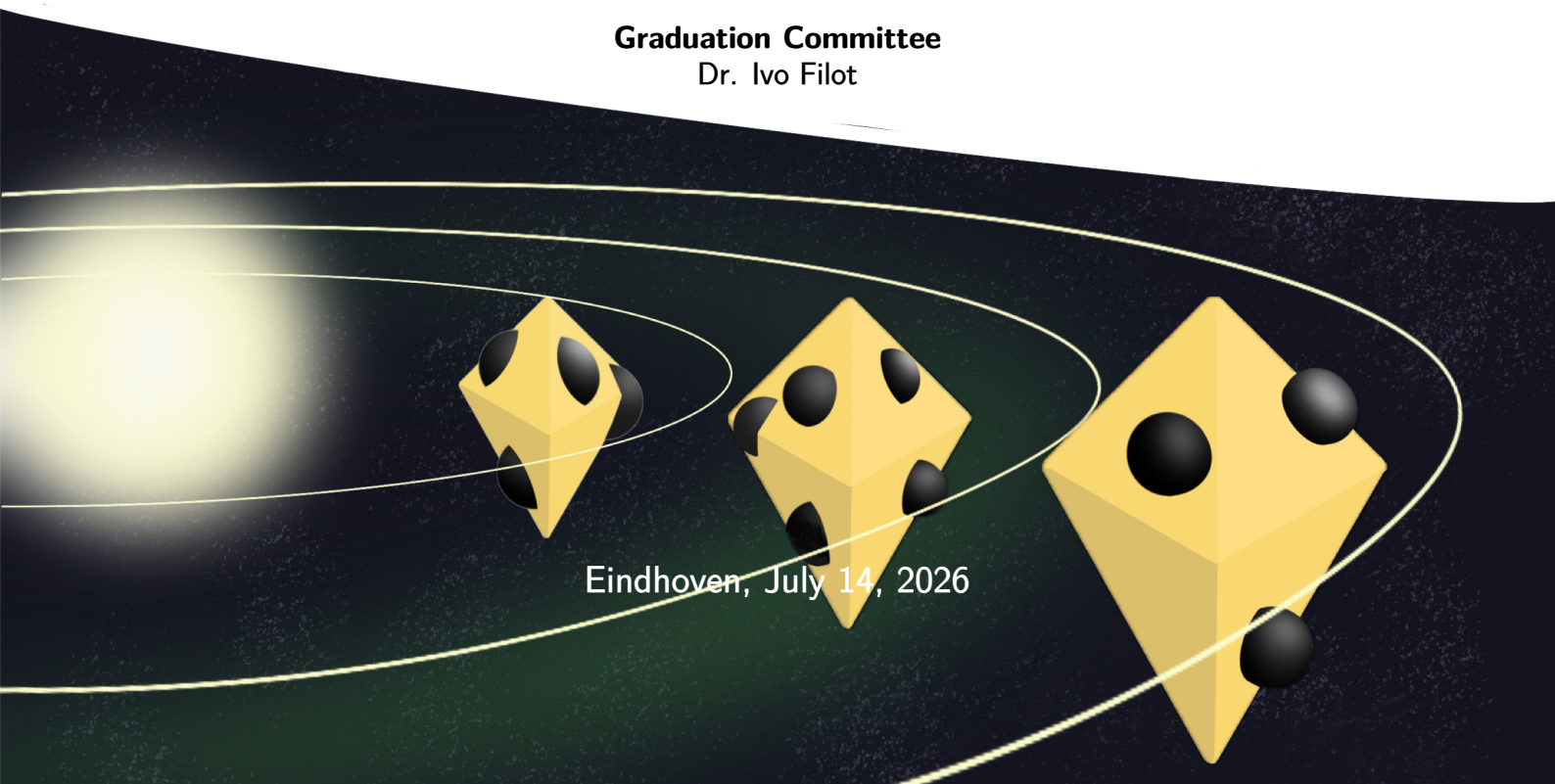

Eindhoven, July 14, 2026

Abstract

CO_2 methanation via the Sabatier reaction is a promising carbon utilization strategy to convert captured CO_2 into natural gas with green hydrogen as feedstock. Ni/CeO_2 is considered as one of the most promising catalysts for CO_2 methanation owing to the synergistic effect of H_2 activation from Ni, CO_2 activation from CeO_2, and an appropriate metal-support interaction (MSI) that promotes interfacial catalysis. However, the influence of CeO_2 properties on catalytic performance remains unclear.

In this work, CeO_2 particle size was tuned using flame spray pyrolysis (FSP) across a range of 9-29 nm, and its effect on CO_2 methanation was systematically investigated in Ni/CeO_2 catalysts calcined at 400 °C. A volcano-shaped relationship between methane formation rate and CeO_2 particle size was observed, with the catalyst supported on 20 nm CeO_2 exhibiting the highest activity (226.2 $\mathrm{mmol_{CH_4}\ g_{Ni}^{-1}\ h^{-1}}$). Rather than arising from a single underlying mechanism, this particle-size effect is shown to reflect two largely distinct CeO_2 particle size effect pathways. A redox-mediated pathway, reflected in the spillover-linked change in support reduction state upon Ni exposure (ΔCe^{3+}, decreasing monotonically from +16.4% at 9 nm to −5.2% at 29 nm), governs the initial CO_2 activation step and tracks CO_2 consumption rate most closely at low calcination temperature. A textural pathway, driven by particle-size-dependent pore volume and pore collapse during synthesis (pore-diameter retention: 44% at 9 nm vs. 96% at 29 nm), instead governs Ni dispersion and hence methanation completion, correlating strongly with calculated Ni-CeO_2 interfacial site density ($R^2 = 0.982$) and producing the CH_4-specific activity optimum at 20 nm. Ni also became progressively more difficult to reduce as CeO_2 particle size decreased, tracking the same interfacial fraction and suggesting the redox pathway is largely a downstream electronic consequence of the textural one rather than an independent size effect. The optimum catalyst identified in this work, Ni/CeO_2 supported on 20 nm ceria, was found to be competitive with literature systems particularly at lower temperatures, achieving 3.93 $\mathrm{mmol_{CO_2}\ mol_{Ni}^{-1}\ s^{-1}}$ at 200 °C and a GHSV of 300,000 ml $\mathrm{g_{cat}^{-1}\ h^{-1}}$ ($CO_2/H_2/He = 1/4/15$), 1 bar.

Contents

List of Figures

List of Tables

1 | Theoretical Background

1.1 | Introduction

Carbon dioxide (CO_2) is one of the most significant greenhouse gases contributing to global climate change. Greenhouse gases trap heat in the Earth's atmosphere by absorbing and re-emitting infrared radiation, a natural process that helps maintain the planet's temperature at a habitable level. Along with water vapor, methane (CH_4), and nitrous oxide (N_2O), CO_2 plays a central role in the naturally occurring greenhouse effect. However, since the industrial revolution, human activities have substantially increased atmospheric concentrations of CO_2, intensifying the greenhouse effect and disrupting the global climate system [38].

Anthropogenic emissions originating from energy production, industrial activities, transportation, and land-use change are the primary drivers of the observed increase in greenhouse gas concentrations [39]. Among long-lived greenhouse gases, CO_2 does not exhibit the highest global warming potential on a per-molecule basis; nevertheless, it accounts for the largest share of total emissions due to its extensive release and long atmospheric lifetime. Consequently, CO_2 remains the dominant contributor to long-term climate forcing and global temperature rise.

The impacts of elevated atmospheric CO_2 concentrations are increasingly evident, including rising global temperatures, more frequent and severe extreme weather events, melting glaciers and polar ice caps, sea-level rise, and widespread ecological disruption [40]. Atmospheric CO_2 levels have exceeded 400 ppm in recent years, underscoring the urgency of developing effective strategies to mitigate emissions and manage existing carbon in the atmosphere [41].

From a chemical standpoint, CO_2 is a stable and inert linear molecule consisting of one carbon atom double-bonded to two oxygen atoms. Its high thermodynamic stability makes direct conversion challenging, often requiring substantial energy input and effective catalysts [42]. Under ambient conditions, CO_2 exists as a colorless, odorless, non-flammable gas and has a broad range of commercial applications, including food processing, refrigeration, fire suppression, and chemical manufacturing [43]. These characteristics also make CO_2 a promising feedstock for producing value-added products when appropriate conversion technologies are employed [44].

To mitigate rising emissions, carbon sequestration and carbon capture technologies have been developed to prevent CO_2 from entering the atmosphere. Carbon sequestration occurs naturally through biological and geological processes and can also be enhanced through engineered systems [45]. While conventional approaches such as afforestation and land management contribute to restoring the global carbon balance, they often require long implementation times and are constrained by land availability. As a result, technological solutions such as carbon capture and storage (CCS) and carbon capture, utilization, and storage (CCUS) have gained increasing attention [46].

CCUS extends the concept of CCS by incorporating pathways that convert captured CO_2 into useful products rather than treating it solely as waste. Although CO_2 utilization alone is unlikely to achieve net-zero emissions—given the additional energy and materials required for conversion—it can play a crucial role when integrated with low-carbon energy systems and efficient capture technologies. Continued research and technological development are therefore essential to improve conversion efficiency, reduce costs, and ensure that CO_2 management strategies contribute meaningfully to long-term climate change mitigation [47].

Utilization routes include physical, chemical, biological, and mineralization processes. CO_2 can be transformed into fuels and chemicals such as methane, urea, methanol, formic acid, and cyclic carbonates, offering both environmental and economic advantages [48]. Among these options, the catalytic conversion of CO_2 to methane is particularly attractive due to its simple product distribution and high selectivity of methane. In addition, the produced methane can be directly used with an existing natural gas infrastructure, including storage and transportation. The reaction of converting CO_2 to methane via hydrogenation is known as the Sabatier reaction.

Apart from the importance of the source of CO_2, the hydrogen used is also of importance. The Power-to-

Gas(PtG) concept, which uses renewable hydrogen from electrolysis to convert CO_2 provides a feasible, environmental friendly solution. This opens the possibility of using excess electricity during low demand seasons, such as in the summer, especially in high capacity electricity production plants with low turndown ratio. This ensures proper storage without wasting energy and higher stability. A life cycle analysis shows a lower emission rate of using methane produced by PtG than natural gas based Compressed Natural Gas (CNG) vehicles [49]. A technoeconomic study concludes that PtG may be competitive compared to fossil fuel derived methane in the future [50].

Apart from optimizing the reactants for the Sabatier reaction, the conditions and catalysts could also be improved. It is normally a high temperature heterogenous catalysis process. By understanding the underlying kinetics and thermodynamics of the catalysts, an efficient catalyst can be created.

1.2 | Heterogenous Catalysis and State of the Art

Catalysis is defined as a substance that increases the rate of reaction without being consumed in the process by offering alternative reaction pathways. Catalysts also enable reactions to occur under lower temperatures and with higher selectivity. A diagram of the catalytic process is as in Figure 1.1.

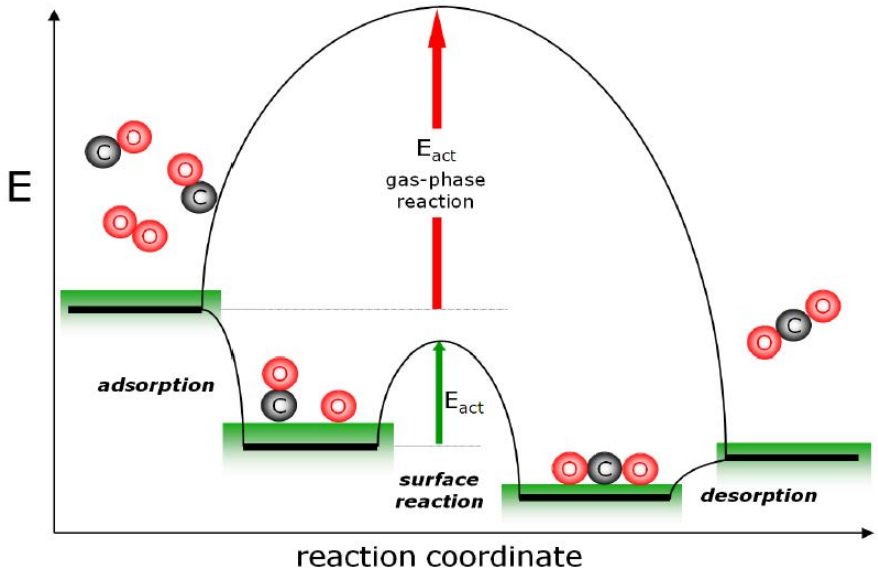

Figure 1.1: Potential energy diagram of a catalytic process [1].

Catalysts include transition metals due to its unique d-band filling properties. The commonly used industrial catalyst for the Sabatier process is nickel, due to its performance and cost effectiveness. An overarching highly researched metal support combination summary and its categorization can be seen in Figure 1.2. Often used Ni counterparts also include cobalt and ruthenium, as well as combination of nickel and cobalt, of which those metals offer comparable, or better, activity or selectivity but worse economic viability [51]. Therefore, nickel based catalysts are particularly interesting to develop.

Various nickel and cobalt based catalysts found in literature has been summarized in Figure 1.3. The exact values has been summarized in Table A.1. As observed, many factors can affect the performance, including its synthesis method, weight loading, and support chosen. These factors then affect different parameters such as reaction mechanism, metal support interaction, particle size of both the metal and support, etc. Among all the support used for Ni, ceria is particularly interesting as it is a reducible oxide, resulting in a capability to store and release oxygen i.e. oxygen storage capacity (OSC). This is particularly important for methanation as it needs to activate CO_2. Dispersing nickel particles over the ceria support has been shown to result in high catalytic activity.

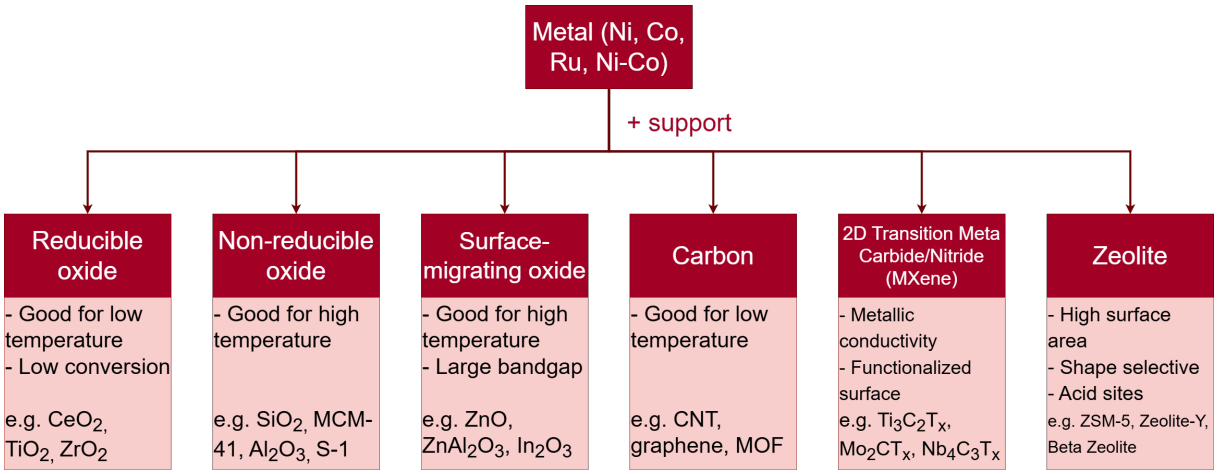

Figure 1.2: CO_2 methanation metal-support variation summary.

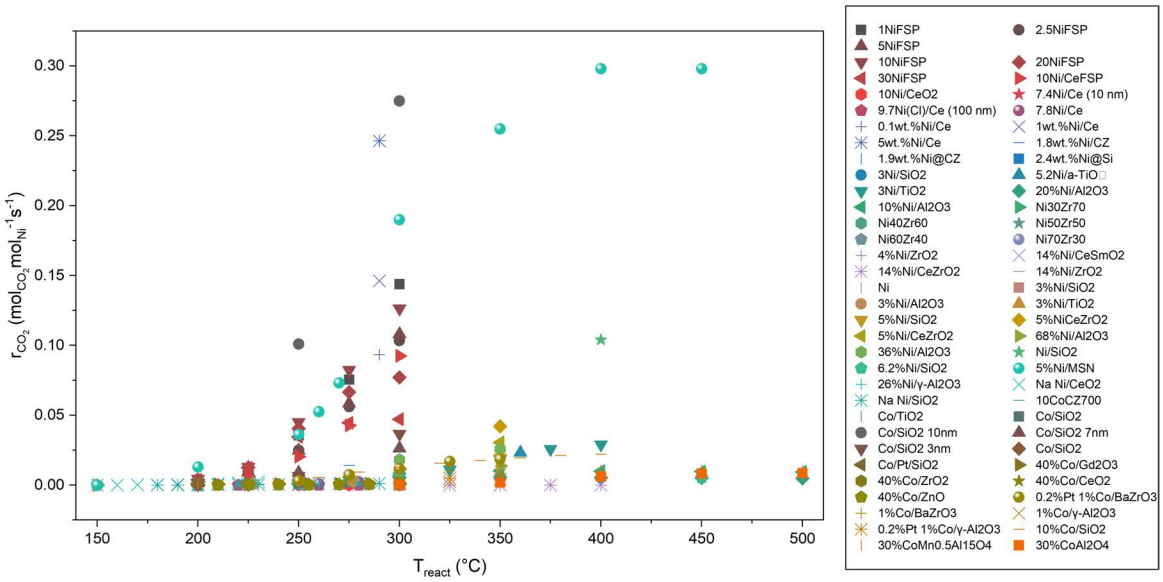

Figure 1.3: Catalytic performance in CO_2 hydrogenation: State of the Art [2–27].

1.3 | CO_2 Reaction Mechanism

The reactions that may occur in CO_2 hydrogenation with Sabatier as the main reaction is summarized as in Table 1.1. Side reactions of the Sabatier reaction includes reverse water gas shift (RWGS), coking reactions (including Boudouard reaction), and methane decomposition. Side reactions may be discouraged by optimal reaction conditions such as low temperature and 4:1 ratio at the inlet.

There is a great deal of debate regarding the step-by-step mechanism of the Sabatier reaction. The possible intermediates and reaction steps are summarized in Figure 1.4 [28]. The step-by-step mechanism itself occurs differently for different metals and support. Wang et al. (2017) identified that on Pd/Al_2O_3, the reaction occurs with formate intermediate with different rate-determining step (rds) for parallel RWGS and methanation. The authors proposed that when an oversaturation of CO* occurs, either due to rapid formate decomposition to CO* or slow CO* hydrogenation, the release of CO instead of conversion to methane may occur. In order to lower the CO selectivity, the sites for CO* hydrogenation should be increased (metal sites), or the sites for HCOO* decomposition (metal support interface) should be decreased [52]. In another study by Wang et al. (2016) using Ru/Al_2O_3, the pathway was found to be also competing RWGS and methanation with rds of CO* hydrogenation, while utilizing Ru/CeO_2 leads to methanol as an intermediate as formate pathway dominates. Catalysts with different metal

Table 1.1: CO_2 methanation and possible side reactions [30].

Eq.	Reaction	$\Delta H°$ (kJ mol^{-1})	$\Delta G°$ (kJ mol^{-1})
1.1	$CO_2 + 4\ H_2 \leftrightharpoons CH_4 + 2\ H_2O$	−165.01	−113.62
1.2	$CO_2 + H_2 \leftrightharpoons CO + H_2O$	41.16	28.67
1.3	$CO_2 + 2\ H_2 \leftrightharpoons C + 2\ H_2O$	−90.14	−90.14
1.4	$CO_2 + C \leftrightharpoons 2\ CO$	172.47	120.15
1.5	$CO + 3\ H_2 \leftrightharpoons CH_4 + H_2O$	−206.17	−142.29
1.6	$CO + H_2 \leftrightharpoons C + H_2O$	−131.30	−91.48
1.7	$CH_4 \leftrightharpoons 2\ H_2 + C$	77.91	42.28

leads to minimally different pathways while utilizing a different type of support with the same metal lead to fundamental pathway or intermediate differences. This is especially due to the fact that alumina is non-reducible while ceria is reducible, leading to different OSC properties [53].

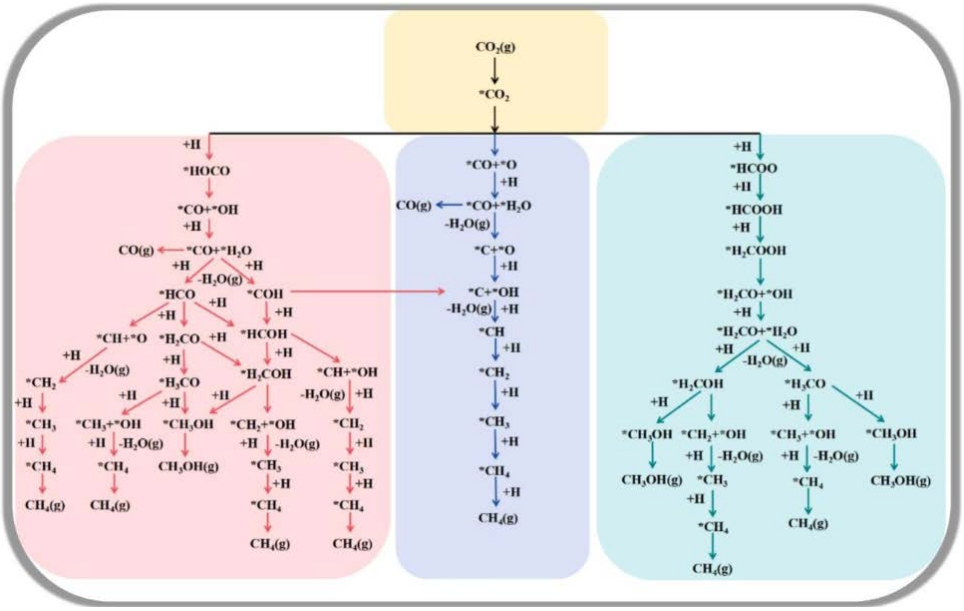

Figure 1.4: CO_2 methanation mechanism pathways summary reprinted from [28].

Taking the research of Struijs et al., ceria supported catalysts provided a more significant pool of active formates (two types) which results in a higher activity than non-reducible catalyst (only one type of formate produced by silica catalyst). Comparing the formate properties present on the support or metal-support interface of Ni/CeO_2, Co/CeO_2, and $Ni\text{-}SiO_2$, it was discovered that the support is the determining factor [54]. Comparing Ni/CeO_2 to Co/CeO_2, despite differing activation energies, the RDS is the same, which is the first CO* hydrogenation.

To analyze the mechanism of the reaction, some additional assumptions can be made. A dissociative adsorption of H_2, or chemisorption, directly happens as it is often preferred. The reaction of CO hydrogenation is assumed to produce methane over a dual active site mechanism indicated by θ and τ, of which CH_x with $x \in \{0, 4\}$ can only adsorb on site θ while hydrogen can adsorb on both. An asterisk (*) and pound sign (#) is used to indicate adsorbed compounds on sites θ and τ respectively. Following the mechanistic insights of Wang et al. and Struijs et al., the hydrogenation of adsorbed CO is taken as the RDS [52, 54]. The proposed mechanism for CO_2 on $Ni\text{-}CeO_2$ is indicated by Equations (1.8) to (1.21). The surface site balances for θ and τ sites are given by Equations (1.22) to (1.23).

$$H_2 + 2* \rightleftarrows 2H* \tag{1.8}$$
$$H_2 + 2\# \rightleftarrows 2H\# \tag{1.9}$$
$$CO_2 + * \rightleftarrows CO_2* \tag{1.10}$$
$$CO_2 * + H\# \rightleftarrows HCOO * + \# \tag{1.11}$$
$$HCOO * + H* \rightleftarrows CO * + H_2O* \tag{1.12}$$
$$H_2O* \rightleftarrows H_2O + * \tag{1.13}$$
$$CO + * \rightleftarrows CO* \tag{1.14}$$
$$CO * + H\# \longrightarrow HCO * + \# \tag{1.15}$$
$$HCO * + H\# \rightleftarrows H_2CO * + \# \tag{1.16}$$
$$H_2CO * + H\# \rightleftarrows H_3CO * + \# \tag{1.17}$$
$$H_3CO * + H\# \rightleftarrows CH_4 * + O* \tag{1.18}$$
$$CH_4* \rightleftarrows CH_4 + * \tag{1.19}$$
$$O * + H* \rightleftarrows OH * + * \tag{1.20}$$
$$OH * + H* \rightleftarrows H_2O * + * \tag{1.21}$$

$$\theta_* + \theta_{H^*} + \theta_{CO_2^*} + \theta_{HCOO^*} + \theta_{CO^*} = 1 \tag{1.22}$$
$$\theta_\# + \theta_{H\#} \approx 1 \tag{1.23}$$

Assuming quasi-equilibrated adsorption, the hydrogen and CO_2 adsorption isotherms are given by Equations (1.24) to (1.26). Taking Reaction (1.15) as the rate-determining step, the reaction rate can be expressed as in Equation (1.27). Assuming quasi-equilibrated upstream steps, the overall rate expression becomes Equation (1.28).

$$\theta_{H^*} = \sqrt{K_{H^*} P_{H_2}}\, \theta_* \tag{1.24}$$
$$\theta_{H\#} = \sqrt{K_{H\#} P_{H_2}}\, \theta_\# \tag{1.25}$$
$$\theta_{CO_2^*} = K_{CO_2} P_{CO_2} \theta_* \tag{1.26}$$
$$r = k_7 \theta_{CO^*} \theta_{H\#} \tag{1.27}$$
$$r = k_7 K_{CO_2} \sqrt{K_{H\#}} P_{CO_2} P_{H_2}^{1/2}\, \theta_* \theta_\# \tag{1.28}$$

In the limit of weak adsorption, the surface coverages approach unity, yielding Equations (1.29) to (1.30). In the opposite limit of strong hydrogen adsorption on both site types, the site balances give (1.31) to (1.32). The apparent reaction orders under zero-conversion conditions are therefore bounded by Equation (1.33).

$$\theta_* \approx 1, \qquad \theta_\# \approx 1 \tag{1.29}$$
$$r \propto P_{CO_2} P_{H_2}^{1/2} \tag{1.30}$$
$$\theta_* \propto P_{H_2}^{-1/2}, \qquad \theta_\# \propto P_{H_2}^{-1/2} \tag{1.31}$$
$$r \propto P_{CO_2} P_{H_2}^{-1/2} \tag{1.32}$$

$$\boxed{\begin{aligned} 0 \leq n_{CO_2} &\leq 1 \\ -\frac{1}{2} \leq n_{H_2} &\leq +\frac{1}{2} \end{aligned}} \tag{1.33}$$

Not only kinetically, the reaction is limited by the metal-adsorbate strength. According to the Sabatier principle (1914), the maximum rate will be achieved by a catalyst whose combination with reactants is of

intermediate stability, to be effectively active while still transient. Meaning that the maximum rate will be obtained by a catalyst which does not bind the reactants too weak or too strongly, but just right. A volcano plot can then be plotted in which the optimum catalyst can be concluded as in Figure 1.5. By varying certain parameters such as particle size, a volcano plot may be obtained.

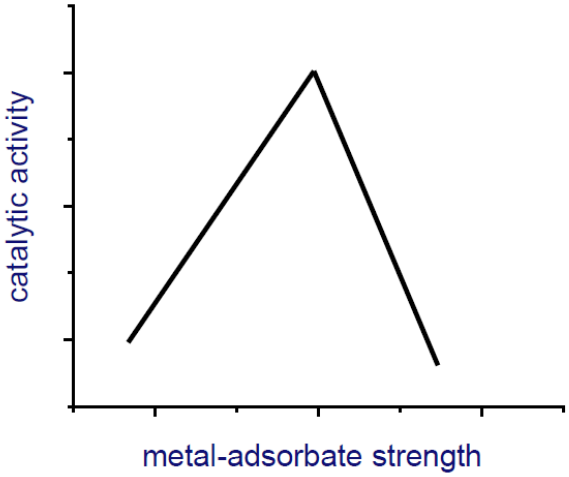

Figure 1.5: Sabatier volcano plot [1].

1.4 | Metal Support Interaction (MSI)

Metal-support interactions (MSI) play a critical role in determining the catalytic performance of supported metal catalysts for CO_2 methanation. The nature and strength of these interactions fundamentally influence catalyst properties including metal dispersion, electronic structure, the active sites, and reaction intermediate pathways. This affects which directly influences active site architecture [55]. Two important related process with MSI for Ni/CeO_2 catalysts are hydrogen spillover and oxygen vacancy formation. Hydrogen spillover, first described by Boudart in 1969, refers to the migration of H atoms from metal particles to the support surface [56]. This phenomenon is particularly pronounced on reducible oxide supports. For Ni/CeO_2 catalysts, hydrogen spillover is intimately connected to oxygen vacancy formation. Upon H_2 reduction, spillover H atoms reduce Ce^{4+} to Ce^{3+} at the Ni-CeO_2 interface, creating oxygen vacancies (O_v). These interfacial oxygen vacancies are crucial for CO_2 activation.

Recent systematic studies have revealed that not all oxygen vacancies contribute equally to catalytic activity [57]. The concentration of active Ni-O_v interfacial sites is determined by the availability and dispersion of metallic Ni, and only oxygen vacancies in close proximity to Ni particles are favorable for methane production. Three types of sites can be distinguished, which are: active interfacial sites consisting of exposed metallic Ni adjacent to oxygen vacancies; SMSI-blocked sites, where strong metal-support interaction causes CeO_x to encapsulate Ni particles; and non-interfacial oxygen vacancies [57]. Preparation variables such as calcination temperature and atmosphere can dramatically alter Ni crystallite size, Ni availability, and interfacial oxygen vacancy density.

1.5 | Morphology Sensitivity

Ceria has a fluorite structure with a face-centered cubic (fcc) lattice. In this structure, each cerium atom is coordinated by eight nearest-neighbor oxygen atoms. The most stable ceria surface is the (111) facet, which is the octahedral shape, followed by (110) and (100). The differing reducibility of the facets results in a varying amount of removable oxygen at the surface. The exposed facets therefore affect the catalytic performance of ceria-supported catalysts, as the reducibility of the support is an important factor. It has been shown that particles exposing a large fraction of mixed (100) and (110) surfaces (rods) exhibit a higher oxygen storage capacity (OSC) and activity than structures dominated by (111) surfaces

(octahedra) [58].

By referring to the mechanism derived previously, it appears that the same behaviour can be predicted for CO_2 methanation. For facet tuning of ceria based catalysts for CO_2 methanation, various researches have been done before. Sakpal et al. has done facet tuning using Ru/CeO_2 for CO_2 methanation [55]. Lin et al. has compared the activity of nanocubes and octahedral particle of Ni/CeO_2 for CO_2 methanation [59]. While Konsolakis and Lykaki has compared the performance of Ni/CeO_2 nanocubes, nanopolyhedra, and nanorods, all via hydrothermal method for CO_2 methanation [60]. There is not yet a comparison for isolating pure morphological effects due to particle size and surface area differences. Utilization of sauter diameter could be implemented to obtain a more accurate comparison between geometrical shapes.

1.6 | Particle Size Sensitivity

Nickel particle size variation on various supports including ceria, titania, and silica has been thoroughly explored. Varying Ni particle size from 2 to above 20 nm has shown that above 5 nm, the particle size of Ni no longer affects the catalyst performance with those below being less selective to methane as stated by both Simons et al. and Adhikari et al [3, 61]. It begs the question of particle size sensitivity of the support (ceria) instead of the metal.

Particle size tuning was done by Lin et al. on cubic (100) ceria for CO_2 methanation in which the MSI and related oxygen vacancy concentration were affected by particle size, causing lower activation energy [62]. The modulated ceria size was 30-50 nm and the activation energy is more than 100 kJ/mol for all catalysts. This begs the question on how the ceria particle size sensitivity affects the performance if the particle size is to be modulated to be under 30 nm.

1.7 | Scope

The importance of support in CO_2 methanation has been highlighted across various research. Ni-CeO_2 as a favorable catalyst has been explored thoroughly. However, there is still a lack of study on the effect of ceria particle size towards the performance. There is also a lack of a proper comparison of Ni-CeO_2 with different ceria morphologies, constricted to the same sauter diameter.

This report focuses on answering the following questions:

- How does the CeO_2 particle size affect the performance of the catalyst in CO_2 methanation?
- What may be the cause of CeO_2 particle size effect?
- Does the CeO_2 size effect change the mechanism of CO_2 methanation?

And also explores the following side questions:

- What is the effect on performance due to the CeO_2 morphology and calcination temperature in CO_2 methanation?
- What do the results mean on an industrial scale?

2 | Materials and Methods

2.1 | Chemicals Used

The metal precursors $Ni(NO_3)_2{\cdot}6H_2O$ (purity $\geq$ 95%), $Ce(ac)_3{\cdot}3H_2O$ (ac=acetate, 99.9% purity), and $Ce(NO_3)_3{\cdot}6H_2O$ (purity $\geq$ 95%) were purchased from Sigma-Aldrich. Polyvinylpyrrolidone (PVP, Mw = 40,000 and 360,000), citric acid, glacial acetic acid (99.7% purity), and 2-ethylhexanoic acid (99% purity), used as additional materials in various synthesis processes, were also obtained from Sigma-Aldrich. All chemicals were used as received without further purification. Demineralized water was used in all experiments.

2.2 | Catalyst Synthesis

2.2.1 | Tuning Particle Size

FSP synthesis was carried out to tune the CeO_2 particle size. using a Tethis NSP10 setup with method based on Yannis et al. [63]. For each synthesis, a solvent mixture consisting of 50 vol% 2-ethylhexanoic acid and 50 vol% glacial acetic acid was prepared. To obtain bare ceria support particles, cerium acetate was dissolved in the solvent mixture at a concentration of 0.15 M. Additional solvent mixture was prepared for washing and cleaning purposes.

The precursor solution was heated to 70 °C and stirred until a clear solution was obtained. After cooling to room temperature, the solution was used for FSP synthesis. The FSP syringe was filled with 40 mL of the cooled precursor solution and refilled several times during production. To sustain the flame, methane and oxygen flow rates of 1.5 L min^{-1} and 3.0 L min^{-1} were used, respectively. Oxygen was employed as the dispersion gas at a flow rate of 5 L min^{-1}, with an overpressure of 2.5 bar at the nozzle.

In doping the synthesized ceria particles with Ni, the method incipient wetness impregnation was used. A fixed loading of 10-wt% of Nickel was done. The particle size of the Nickel was controlled to be 3.7-6.6 nm using citric acid as a ligand at 1:1 ratio. The Ni precursor and citric acid was diluted together in water of which volume is adjusted to the pore volume of each ceria synthesized. The solution is then sonicated and mixed with the ceria support. The mixture is then dried in an oven overnight at 110 °C. The catalyst is then calcinated at 150 °C with airflow for 2 h and continued with 400 °C with airflow for 2 h, with a heating rate of 1 °C min^{-1}.

2.2.2 | Synthesis Parameter Tuning

In preparation for an accurate particle size tuning, the synthesis method was varied to understand the effect of morphology tuning of ceria. Flame spray pyrolysis (FSP), hydrothermal, and direct calcination methods are used, to create octahedral, cubic, and spherical particles respectively. The FSP method is explained further in the previous section. The hydrothermal method is based on Saw et al. utilizing PVP (360,000). Two catalysts were synthesized using ceria precursor concentration of 13.5 mM. The amount of polyvinylpyrrolidone (PVP, M_w = 360,000) was fixed at 7.5 g. The required amount of cerium precursor was first dissolved in 300 mL of deionized water under stirring. Subsequently, PVP was slowly added to the solution and stirred for several hours until complete dissolution was achieved. The resulting homogeneous solution was transferred into a teflon lined autoclave and aged at 140 °C for 12 and 24 h. After hydrothermal treatment, the products were recovered by centrifugation at 5,000 rpm for 20 min, repeated four times, and dried overnight at 110 °C. Finally, the sample was calcined at 700 °C for 2 h, with a heating rates of 10 °C min^{-1} with airflow [64].

For direct calcination, the 3-5 g nickel nitrate precursor is calcined directly at temperature of 400 °C for 2 h, using a heating rate of 2 °C min^{-1} with airflow. Three different types of ceria synthesis methods were done to obtain three different type of ceria morphology which in theory would show different performance and different particle size sensitivity. After the ceria synthesis is done, each one were impregnated by the IWI method as described in the previous section.

As the Ni/CeO_2 MSI is discussed to be sensitive to calcination temperature. The effect of calcination temperature is then explored in a series of particle size variation in the approximately same range of particle size tuning at base case temperature. The additional synthesis done at 350 °C with other parameters kept constant.

2.2.3 | Synthesis summary

In Table 2.1 is the summary for all synthesized Ni/CeO_2. Different synthesis method, particle shape, and size are shown in the naming convention, indicating FSP synthesized octahedral particles (O), hydrothermal synthesized cubic particle (C), and direct calcination synthesized spherical particles (S). The naming is written in the structure of Ni/CeO2-Particle Size-Shape. In the case of calcination temperature tuning, Ni/CeO2-Particle Size-Shape-Calcination Temperature is used.

Table 2.1: Overview of Ni/CeO_2 catalyst series and their respective synthesis parameter under investigation.

Particle Size Tuning	Calcination Temperature Tuning	Morphology Tuning
Ni/CeO2-9-O	Ni/CeO2-9-O-350	Ni/CeO2-9-S
Ni/CeO2-20-O	Ni/CeO2-17-O-350	Ni/CeO2-15-C
Ni/CeO2-29-O	Ni/CeO2-20-O-350	
Ni/CeO2-15-O	Ni/CeO2-30-O-350	
Ni/CeO2-23-O		

2.3 | Characterization

Nitrogen physisorption measurements were performed at 77 K using a Micromeritics TriStar II 3020 analyzer. Typically, 50–70 mg of catalyst was used for each measurement. Prior to analysis, the samples were pretreated under vacuum at 350 °C for 2 h, followed by a nitrogen gas flow to remove adsorbed water and residual impurities. The obtained adsorption data were subsequently processed to determine the specific surface area and pore volume.

H_2 temperature-programmed reduction (H_2-TPR) measurements were first carried out using Micromeritics Autochem II 2020. Typically, 50 mg of catalyst was used for each experiment and placed in a U-shaped quartz tube between plugs of glass wool to keep the sample in position. Prior to reduction, the sample was pretreated in a flow of He for 60 min at 150 °C. After pretreatment, the sample was cooled down to room temperature and the flow was switched to a mixture of 4 vol% H_2/N_2. Once a stable signal was obtained, the TPR is then performed by ramping the temperature from 100 °C to 700 °C at a heating rate of 10 °C min^{-1}.

Transmission Electron Microscopy (TEM) was used to observe the morphology of synthesized catalysts. The sample was prepared by dissolving one small spatula scoop of catalyst in 20 mL of ethanol. The sample is sonicated to ensure even distribution and is then deposited onto the Cu support grid and film. The TEM was done at the courtesy of Daniil Efanov.

Scanning Transmission Electron Microscopy - Energy Dispersive X-ray analysis (STEM-EDX) were carried out on a FEI-cubed Cs-corrected Titan instrument operating at an acceleration voltage of 300 kV using High-Angle Annular Dark-Field (HAADF) imaging technique. Ni/CeO_2 catalysts were reduced at 300 °C for 4 h under a flow of 20 vol% H_2 in He (50 ml/min), using a heating rate of 5 °C min^{-1}, followed by passivation at room temperature. The as-prepared and passivated samples were crushed and sonicated in analytical-grade absolute ethanol before deposition on Cu grids. The HAADF-STEM-EDX was done at the courtesy of Stefan Bouts.

X-ray diffraction (XRD) measurements were performed to evaluate the crystallinity of the samples. Diffraction patterns were collected using a Bruker D2 Phaser powder diffractometer equipped with Cu Kα radiation. The data were recorded over a 2θ range of 20–80°, using a step size of 0.015° and a counting time of 0.25 s per step. The obtained diffractograms were analyzed by Scherrer Equation using Origin

software to estimate the crystallite sizes. The crystallite size of CeO_2 was calculated from the (111) reflection using a Lorentz function, while the crystallite size of Ni was determined from the (200) reflection of NiO with Gauss function, both using Lamda = 0.154 nm and shape factor of 0.94.

CO chemisorption measurements were carried out using Micromeritics ASAP 2020 Plus to obtain metal particle dispersion and particle size. Catalyst sample of 80-110 mg was loaded into a U-shaped quartz tube reactor between two plugs of quartz wool. Prior to chemisorption measurements, the sample was reduced at 300 °C using a mixture of 5 vol% H_2/He for 4 h and then evacuated for 1 h. The sample was then cooled to -20 ° C, where then CO chemisorption was conducted [65]. In calculating dispersion and particle size, a factor of Ni:CO of 1.5:1 was used, this is to account for the presence of both bridged and linear adsorption of CO on Ni (Ni:CO of 2:1 and 1:1).

X-ray Spectroscopy (XPS) was used to study the surface chemical properties of the as-prepared and reduced (XPS-red) with a KAlpha XPS apparatus (Thermo Scientific) equipped with an aluminum anode (Al Kα = 1486.68 eV) monochromatized X-ray source. Fine samples were placed on double-sided carbon tape. The scanning time and frequency were adjusted to minimize the charging effect. The reduction of the samples for post-reduction XPS was done ex-situ. The reduced samples were loaded onto the sample holder in glovebox and is loaded onto the apparatus in a vacuum sealed holder. The U"' (Ce4+) component of the Ce 3d line with a characteristic position of 916.7 eV was used to correct the binding energies of Ni and Ce. Spectral lines were fitted with the CasaXPS software using varying functions and baseline fitting. The Ce 3d line was fitted according to a model described in the Gao et al. while the Ni 2p is fitted based on Biesinger et al. and Rodriguez et al. [66–68]. The XPS and XPS-red were done at the courtesy of Zhang ShuChi and Ding Yi.

In-situ FTIR is done using a combination of CO_2 and H_2 which are alternated and combined accordingly. IR spectra are recorded on a Bruker Vertex 70v FTIR spectrometer equipped with a MCT (Mercury Cadmium Telluride) detector. The experiments are performed in situ using a home-built environmental transmission IR cell. Self-supporting pellets are made by pressing approximately 20 mg of sample diluted by SiO_2 (1:1 ratio, silica confirmed to have no signal) in a disc. Each spectrum is collected by averaging 62 scans with a 2 cm–1 resolution in the 4000–1000 cm–1 range. For CO IR measurements, the sample was first reduced in a flow of 20 vol.% H2 in He at 300 °C (heating rate 5 °C/min) for 4 h. For in situ CO_2 methanation measurements, the spectra are recorded in a flow of CO_2 and H_2 balanced by He using a forward/backwards shift (H_2/CO_2+H_2/H_2/CO_2+H_2/CO_2/CO_2+H_2) at 200 °C and measurement interval of 2 min.

Inductively Coupled Plasma Optical Emission Spectroscopy (ICP-OES) is used to determine the chemical composition, and more importantly, to confirm the metal loading of the as-prepared catalysts using Spectro CIROS CCD Spectrometer. Prior to these measurements, 25 mg of the catalysts were dissolved in 5 mL of concentrated sulfuric acid followed by dilution in water.

2.4 | Catalytic Performance Test

Catalytic activity measurements were performed using a high-throughput setup equipped with a 10-tube flow reactor. For each reactor, 10 mg of catalyst (sieved to a particle size fraction of 250–500 μm) and were mixed with 290 mg of silicon carbide (SiC). The resulting mixture was loaded into a quartz tubular reactor and positioned between two plugs of quartz wool. To ensure an equal pressure drop across all reactors, a pressure test was conducted and additional quartz wool was added when necessary. Prior to reaction, the catalysts were pretreated *in situ* at 300 °C for 4 h under a flow of 20 vol% H_2 in He, using a heating rate of 5 °C min^{-1}. The total gas flow through each reactor was maintained at 50 mL min^{-1}. Reaction was carried out using a feed gas composition of 20 vol% H_2, 5 vol% CO_2, and 75 vol% He at a total flow rate of 50 mL min^{-1}, 1 bar, if not mentioned.

Catalytic performance was evaluated over a temperature range of 200–300 °C. While the activation energy analysis was evaluated over a temperature range of 185–200 °C. At each temperature, the dwell time was 120-180 min and the heating rate between steps was 10 °C min^{-1}. The H_2 and CO_2 reaction order was evaluated using different concentration variations at 200 °C. At each concentration, the dwell time was 120–180 min and the heating rate between steps was 10 °C min^{-1}. The reactor

effluent was analyzed online using a gas chromatograph (Interscience Compact GC) equipped with two thermal conductivity detectors (TCDs) and a flame ionization detector (FID). The FID was used for hydrocarbon analysis, while the TCDs were used to quantify permanent gases such as CO, CO_2, O_2, and H_2.

The data spectra from the performance and activity tests is then processed using calibration points of GC signals at 1%-vol for CO_2, CH_4, and CO. The resulting mole fractions are then analyzed using Equations (2.1) until (2.9). Mole fractions are indicated with the symbol of x, while F indicates the flow rate, while temperature and pressure conditions is at temperature standard IUPAC conditions ($T = 273.15$ K and $P = 1$ bar). Calculations were normalized using the ideal gas constant $R = 0.08314\ \mathrm{L \cdot bar \cdot mol^{-1} \cdot K^{-1}}$ and a standard molar volume $V_m = 22.711\ \mathrm{L \cdot mol^{-1}}$, corresponding to modern IUPAC reference conditions.

$$S_{\mathrm{CH_4}} = \frac{x_{\mathrm{CH_4,out}}}{x_{\mathrm{CO,out}} + x_{\mathrm{CH_4,out}}} \tag{2.1}$$

$$X_{\mathrm{CO_2}} = \frac{x_{\mathrm{CH_4,out}} + x_{\mathrm{CO,out}}}{x_{\mathrm{CH_4,out}} + x_{\mathrm{CO,out}} + x_{\mathrm{CO_2,out}}} \tag{2.2}$$

$$\text{At 1 bar:} \quad p_i = x_i \tag{2.3}$$

$$\mathrm{Activity}_{CH4} = \frac{F(\mathrm{CO_2})_{\mathrm{in}}}{R \times T} \times \frac{x_{\mathrm{CH_4,out}}}{x_{\mathrm{CH_4,out}} + x_{\mathrm{CO,out}} + x_{\mathrm{CO_2,out}}} \tag{2.4}$$

$$r_{\mathrm{CH_4}} = \frac{Activity}{g_{N_i}} \tag{2.5}$$

$$\text{Specific Activity}_{CH4} = r_{\mathrm{CH_4}} \times M_w \tag{2.6}$$

$$\mathrm{Activity}_{CO} = \frac{F(\mathrm{CO_2})_{\mathrm{in}}}{R \times T} \times \frac{x_{\mathrm{CO,out}}}{x_{\mathrm{CH_4,out}} + x_{\mathrm{CO,out}} + x_{\mathrm{CO_2,out}}} \tag{2.7}$$

$$r_{\mathrm{CO}} = \frac{Activity_{CO}}{g_{N_i}} \tag{2.8}$$

$$r_{\mathrm{CO_2}} = \frac{F(\mathrm{CO_2})_{\mathrm{in}}}{V_m} \times \frac{X_{\mathrm{CO_2}}}{g_{Ni}} \tag{2.9}$$

Turnover Frequency (TOF) is used to normalize activity per active site per unit time. In this work, we use TOF normalized by surface Ni as the active site with comparability to Ni structure sensitivity in Adhikari et al. and Simons et al. [61, 69]. The r_{x} is converted to moles-normalized by molar weight of Ni ($M_w = 58.69$ g/mol) and dispersion (symbolysed by D) as in Equation 2.10. The x in this formula are used for CH_4, CO_2, and CO.

$$TOF = r_{surface} = \frac{r_{\mathrm{x}\times M_w}}{D} \tag{2.10}$$

Kinetic measurements were carried out under low-conversion conditions (under 5%) such that reactant concentrations remained effectively constant over the temperature range studied. Under these conditions, the observed reaction rate may be expressed as Equation 2.11 where Arhennius can then be implemented. Substituting Eq. 2.12 into Eq. 2.11 gives Eq. 2.13. Then a plot of $\ln(r_{\mathrm{CH4}})$ versus $1/T$ yields a straight line with slope $-E_a/R$. Therefore activation energy can be obtained from the slope multiplied by R. Activation energy can also be calculated from $\mathrm{Activity}_{CH4}$ as well as mass is a constant variable.

$$r_{\mathrm{CH4}} = C^* \, k(T) \tag{2.11}$$

$$k(T) = A \exp\left(-\frac{E_a}{RT}\right) \tag{2.12}$$

$$\ln(r_{\mathrm{CH4}}) = \ln(C^* A) - \frac{E_a}{R}\frac{1}{T} \tag{2.13}$$

3 | Results and Discussion

3.1 | Tuning Particle Size

3.1.1 | Characterization

Properties related to crystallite and particle size of the catalyst are summarized as in Table 3.1. In Figure 3.1, the spectra for each variation can be seen where the NiO peak is very broad but could still be distinguished and fitted as in Table B.1. Contrast and morphology difference can still be visually distinguishable in TEM and STEM for Ni/CeO2-29-O and therefore the particle size distribution (PSD) could also be calculated as in Figures 3.2 and 3.3. While Ni/CeO2-20-O and Ni/CeO2-9-O both have been analyzed with TEM and STEM, but PSD was deemed infeasible from all results, depicted in Figure B.1, B.2, B.4, and B.5. At a constant ligand to metal ratio, the particle size of Ni was controlled at 3.7-6.6 nm with the minimum at Ni/CeO2-20-O. In Ni/SiO_2, at constant ligand:metal ratio and wt%, the resulting Ni particle size is limited and/or controlled by the structural property of the silica (e.g. pore volume) [3]. This is not the case in Ni/CeO_2 as the intermediate ceria size and pore volume produced the best dispersion and smallest Ni.

Table 3.1: Summary of CeO_2 and Ni characterization data for the Ni/CeO_2 particle size tuning series.

	CeO_2 Properties			Ni Properties				
Catalyst	D_{XRD} **(nm)**	D_{TEM} **(nm)**	D_{STEM} **(nm)**	D_{XRD} **(nm)**	D_{TEM} **(nm)**	D_{STEM} **(nm)**	D_{Chemi} **(nm)**	**Dispersion (%)**
Ni/CeO2-9-O	9.4	—	—	5.3	—	—	4	24
Ni/CeO2-15-O	15.7	—	—	5.3	—	—	3.7	26
Ni/CeO2-20-O	19.6	—	—	4.8	—	—	3.6	27
Ni/CeO2-23-O	22.5	—	—	6.6	—	—	4	24
Ni/CeO2-29-O	28.6	23.8 ± 8.4	36.2 ± 24.5	8.0	5.1 ± 2.2	11.4 ± 4.3	6.6	15

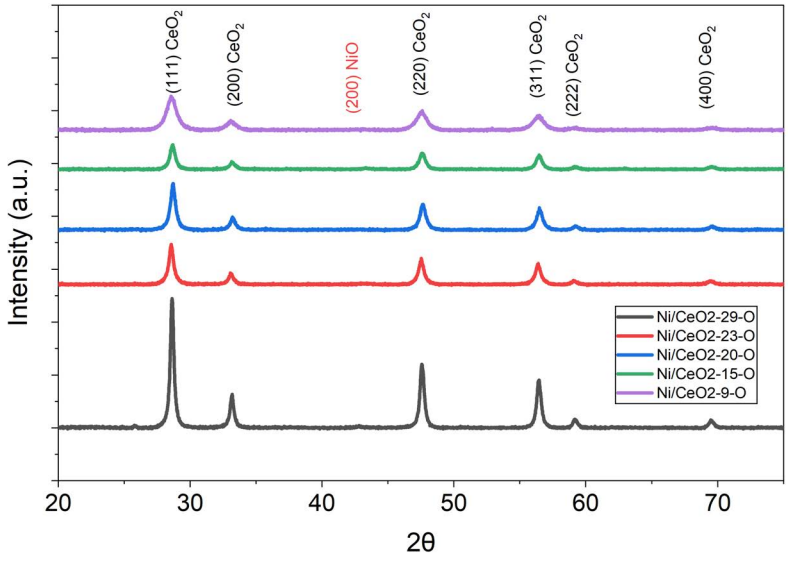

Figure 3.1: XRD of Ni/CeO_2-O particle size variation.

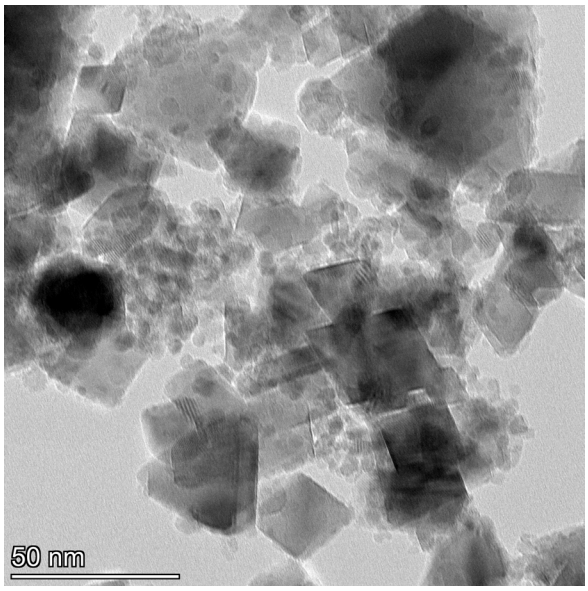

(a) TEM image 1

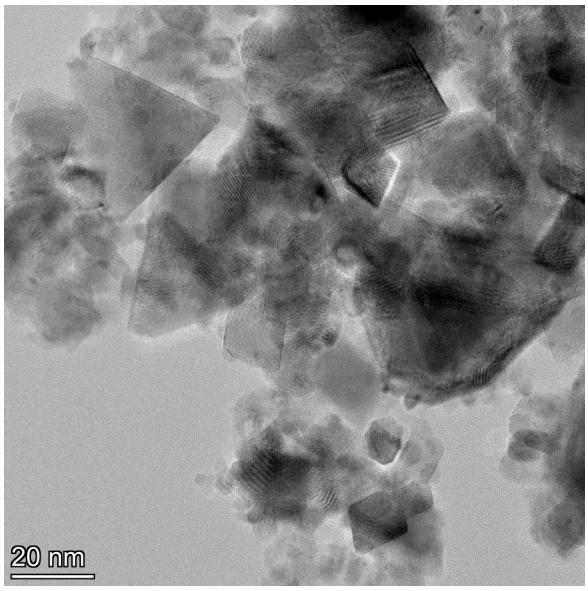

(b) TEM image 2

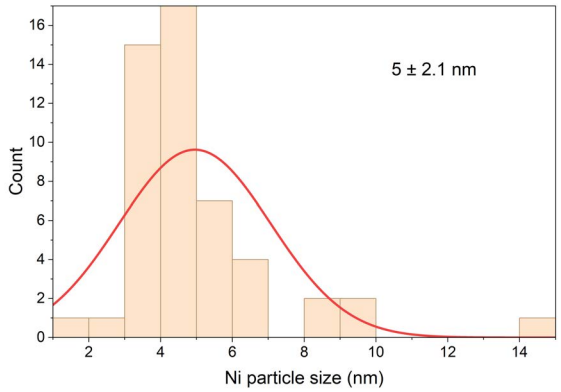

(c) Ni particle size distribution

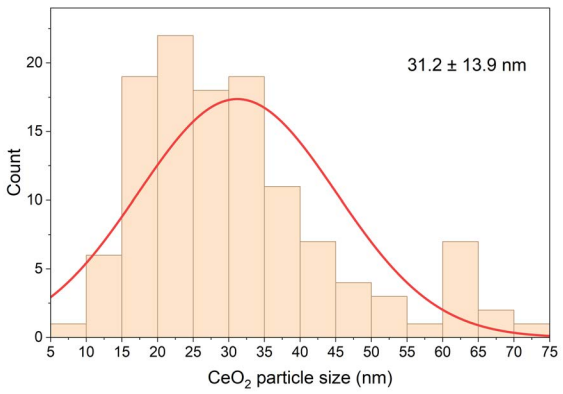

(d) CeO_2 particle size distribution

Figure 3.2: TEM images and particle size distributions of Ni/CeO2-29-O.

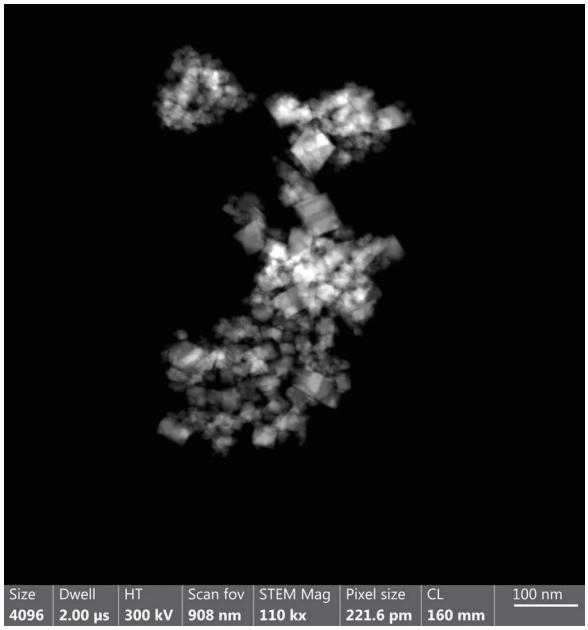

(a) STEM HAADF image

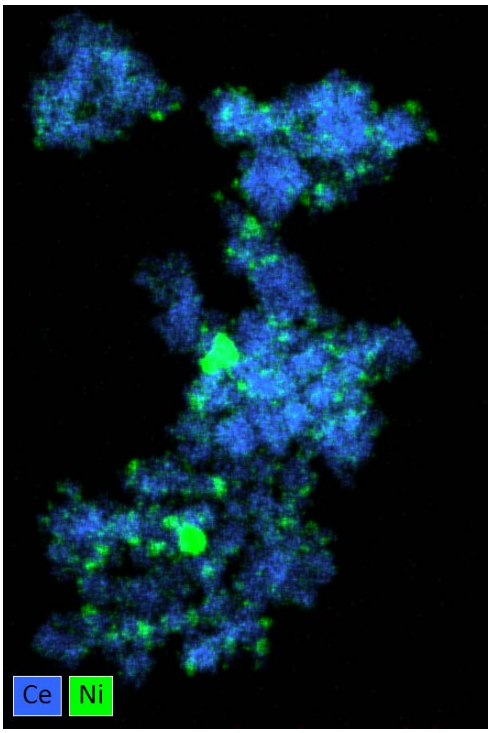

(b) EDX image

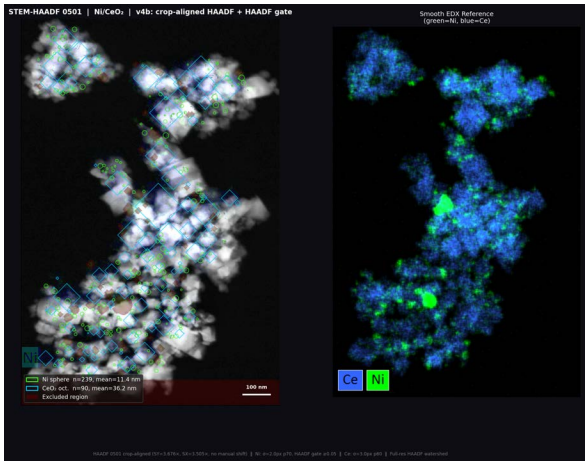

(c) PSD count overlay.

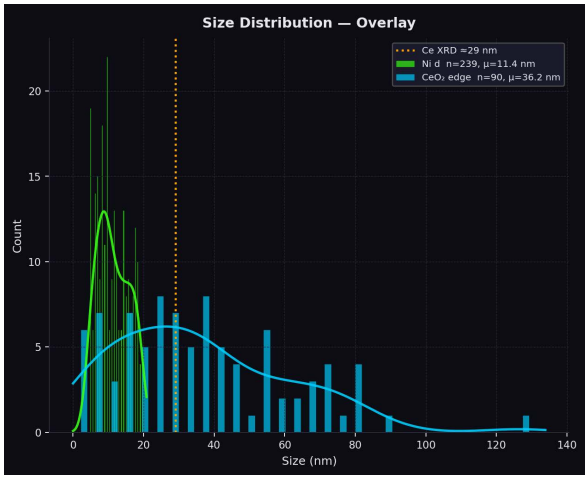

(d) Particle size distribution

Figure 3.3: STEM images and particle size distributions of Ni/CeO2-29-O.

It can be noted that the dispersion of Ni itself is has an optimum point at Ni/CeO2-20-O with 27% dispersion, depicted in Figure 3.4 and tabulated in Table B.5. The chemisorbed CO is calculated over the tested catalyst weight, but dispersion and Ni particle size were calculated using the actual Ni wt% analyzed through ICP-OES, tabulated in Table B.4. Individual CO chemisorption behaviour and repeat measurements are displayed in Figure B.6. We ascertained that CO chemisorption results were sufficiently accurate to determine surface based on linear regression of CO_2 activity to CO chemisorbed as in Figure B.7 which shows $R^2 = 0.9157$.

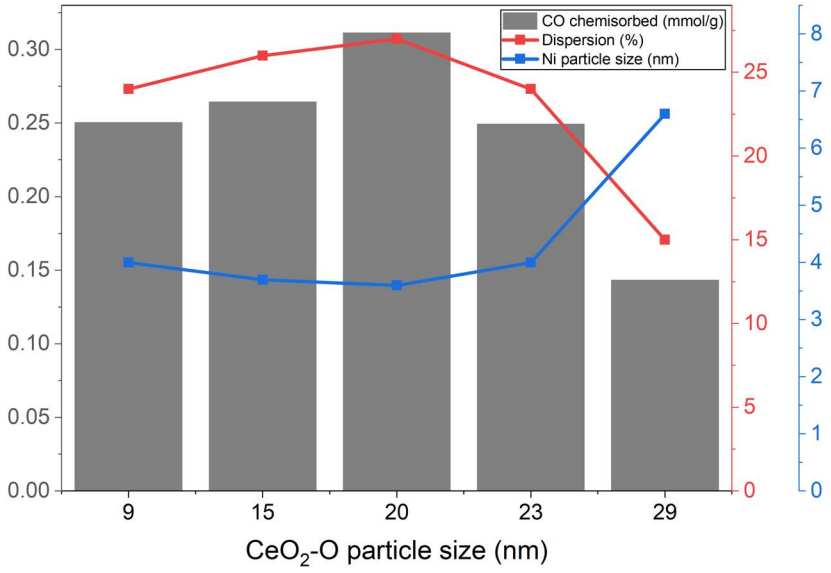

Figure 3.4: CO chemisorption results of Ni/CeO_2-O particle size variation at -20 °C after reduction at 300 °C for 4 h under a flow of 20 vol% H_2 in He.

Stoichiometric H_2 was calculated as the amount needed to theoretically reduce all NiO to Ni (using actual Ni weight by ICP-OES). Each catalysts has a consumption excess which was calculated as in Figure 3.5a. The over-consumption is correlated with hydrogen spillover from Ni to CeO_2 which leads to some surface reduction [2, 19]. The correlation of excess H_2 consumption to particle size is seen in Figure 3.5b. While a linear regression yields a moderate correlation ($R^2 \approx 0.48$), a downward trend in H_2 consumption with increasing particle size emerges, while excluding the 20 nm. However, the 20 nm CeO_2 support indicates a structural "sweet spot", combined optimized nickel dispersion, indicates an optimum in the Ni/CeO_2 interfacial parameter [57, 70]. The TPR spectra itself in Figure 3.6, shows the reduction peak centered approximately at 300 °C. Therefore, 300 °C was selected to ensure the completely reduction while minimizing the particle sintering during reduction.

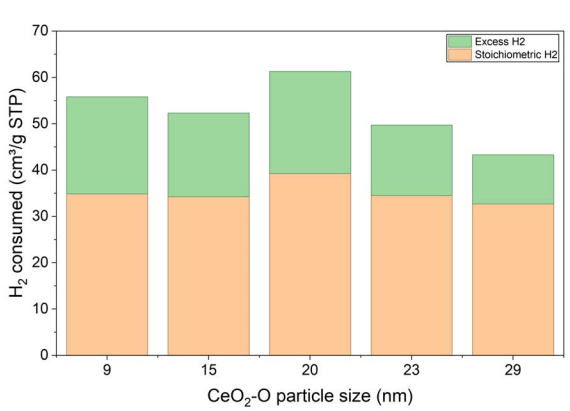

(a) H_2 consumption and excess.

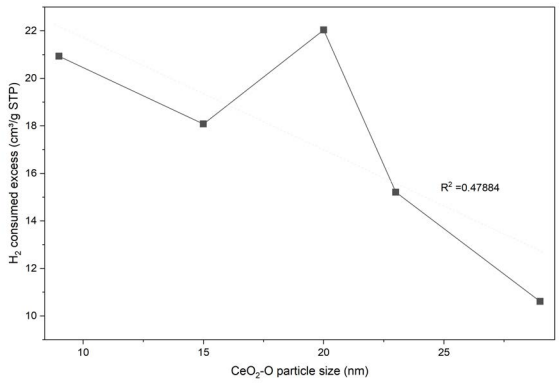

(b) Correlation of particle size and H_2 excess consumption.

Figure 3.5: H_2 consumption and excess of Ni/CeO_2-O particle size variation during TPR with assumption of 1:1 H_2 reducing NiO to Ni.

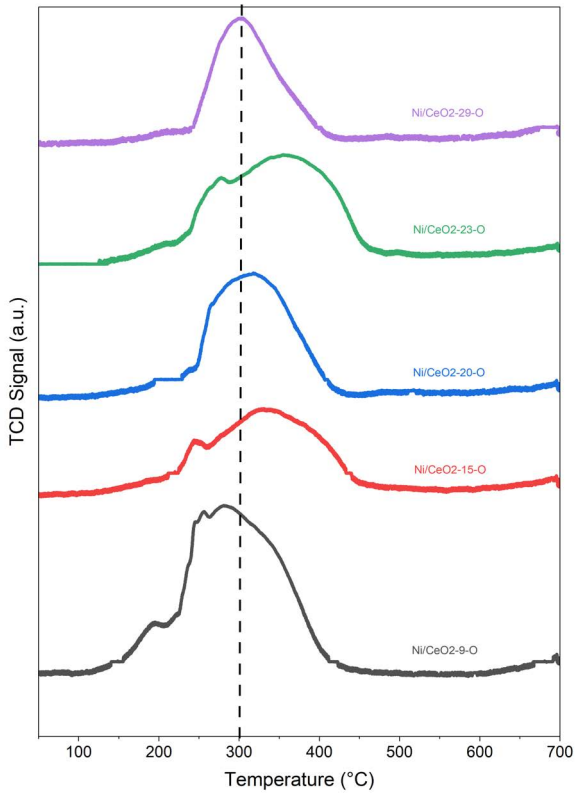

Figure 3.6: H_2-TPR results of Ni/CeO_2-O with different CeO_2 particle sizes.

The surface area, pore volume, and pore diameter are tabulated in Table 3.2. The change of pore volume and surface area indicates changes in textural properties after calcination. On low particle size supports, as in 9 and 15 nm, there is a huge pore volume decrease of 67.9% and 48.3%, as well as surface area decrease, indicating textural collapse and restructuring. Trapped high precursor concentration drives aggressive particle migration and coalescence (PMC), leading to larger Ni particles [71]. At higher ceria particle sizes, loss of surface area at higher particle sizes are able to be compensated with the Ni surface area [72].

Table 3.2: Texture properties of CeO_2 supports and Ni/CeO_2 catalysts.

CeO_2 supports

Catalyst	BET Surface Area (m^2/g)	Pore Volume (cm^3/g)	Pore Diameter (Å)
CeO2-9-O	150.83	0.563	149.342
CeO2-15-O	88.06	0.362	164.609
CeO2-20-O	71.00	0.275	154.707
CeO2-23-O	75.00	0.238	126.981
CeO2-29-O	44.11	0.165	149.549

Ni/CeO_2 catalysts

Catalyst	BET Surface Area (m^2/g)	Pore Volume (cm^3/g)	Pore Diameter (Å)
Ni/CeO2-9-O	109.77	0.181	65.801
Ni/CeO2-15-O	84.60	0.187	88.215
Ni/CeO2-20-O	83.95	0.186	88.558
Ni/CeO2-23-O	54.71	0.135	98.378
Ni/CeO2-29-O	50.88	0.182	142.766

By evaluating the theoretical geometric calculations against experimental data across the ceria particle size series, the surface coverage behaviour could be analyzed [63]. A model of a homogenously distributed

Ni over the ceria volume and an all-surface model (egg-shell) of Ni were tabulated for its surface coverage and atomic rato in Table 3.3. The ICP results were also processed as a homogenous model in Table 3.4 for more accurate comparison. From XPS (pre-reduced), accurate data of atomic ratio and surface coverage of Ni on ceria could be obtained as in Table 3.5. XPS effectively probes the surface at with depth of 7 nm, while the catalysts have particle size of 9 to 29 [73]. It can be observed that the surface coverage calculated by XPS has a higher correlation to homogenous assumption at lower particle size and decreasing correlation as it increases. Comparison to the ICP-based calculation provides a clearer relationship where the increase in ceria particle size leads to increased difference of surface coverage by surface and bulk measurement.

Comparing the XPS to all surface assumption, the real surface coverage is still lower than the maximum possible, with the ratio indicating the amount of Ni at the surface by the theoretical total if all Ni is on surface. This structural evolution appears to control the accessibility of the active phase, leading to a strong linear correlation ($R^2 = 0.937$) when compared to experimental CO chemisorption capacities. CO chemisorption selectively titrates only exposed, reduced metallic surface sites, which the high linearity indicates that the structural stability of nickel dispersed on outer shell is associated with the availability of active metal sites.

Table 3.3: Theoretical calculation of surface Ce and Ni atom densities for CeO_2 nanoparticles of nominal radius $R_{\text{nominal}} = 0.326$ nm and unit cell volume $V_{\text{cell}} = 0.158$ nm^3, assuming a surface Ce density $\rho_{\text{Ce, surf}} = 12.79$ atoms/nm^2 [31,32]. Calculations assume a homogeneous Ni distribution ($(\text{Ni/Ce})_{\text{homogen.}}$) and an all-surface Ni distribution ($(\text{Ni/Ce})_{\text{all surf.}}$).

d (nm)	A (nm^2)	V (nm^3)	C_{pp}	Ni_{pp}	$\text{Ni/nm}^2_{\text{hom}}$ [a]	$(Ni/Ce)_{\text{hom}}$ [a]	$\text{Ni/nm}^2_{\text{surf}}$ [b]	$N_{\text{Ce, surf}}$	$(Ni/Ce)_{\text{surf}}$ [b]
9	281	344	8700	2836	4.084	0.326	10.108	3589	0.790
15	779	1591	40278	13131	4.084	0.326	16.847	9969	1.317
20	1386	3771	95474	31125	4.084	0.326	22.462	17722	1.756
23	1833	5736	145205	47337	4.084	0.326	25.832	23438	2.020
29	2913	11497	291065	94887	4.084	0.326	32.570	37261	2.547

[a] Homogeneous Ni distribution throughout the particle volume.
[b] All-surface Ni distribution (all Ni atoms located on the particle surface).

Table 3.4: ICP-OES elemental analysis of Ni/CeO_2 catalysts: experimental Ni and Ce loading, surface Ni density, and comparison with the theoretical homogeneous distribution model.

d (nm)	wt% Ni (ICP)	Ni (ICP)	Ce (ICP)	$(\text{Ni/Ce})_{\text{ICP}}$	Ni/nm^2 (ICP)	ICP/hom[a]
9	9.1	0.156	0.528	0.295	3.691	0.904
15	9.0	0.153	0.529	0.289	3.616	0.885
20	10.3	0.175	0.521	0.336	4.209	1.031
23	9.0	0.154	0.529	0.291	3.645	0.892
29	8.6	0.146	0.531	0.275	3.441	0.843

[a] Ratio of experimental bulk Ni/Ce to theoretical homogeneous Ni/Ce; not necessarily 1:1 with the nominal wt%, but of approximately the same order of magnitude.

Table 3.5: XPS surface quantification of Ni/CeO_2 catalysts using relative sensitivity factors $\text{RSF}_{\text{Ni}} = 22.18$ and $\text{RSF}_{\text{Ce}} = 51.62$ [33], compared against the all-surface model, the homogeneous model, ICP, and CO chemisorption.

d (nm)	I_{Ni}	I_{Ce}	$(\text{Ni/Ce})_{\text{XPS}}$	Ni/nm^2 (XPS)	XPS/surf.	XPS/hom.	XPS/ICP	CO chemisorbed[a]
9	9999	60954	0.382	4.783	0.47	1.17	1.30	0.250
20	73309	192937	0.884	11.078	0.49	2.71	2.63	0.311
29	18500	50341	0.855	10.715	0.33	2.62	3.11	0.143

[a] Comparing CO chemisorption to XPS/all-surface ratio: $R^2 = 0.937$ [36].

The chemical evolution of the surface sites under reducing conditions can be observed in the behaviour of Ce 3d and Ni 2p spectra before and after hydrogen exposure in Table 3.6 and Figures B.9 and B.8.

The smallest particle suffer from nickel which is locked into an unreactive (hard to reduce) ionic state, leaving a dominant Ni^{2+}–CeO_2 phase (55.0%) and a negligible metallic Ni^0 yield (7.1%) post-reduction, despite the high support reducibility. The intermediate size shows the highest metallic concentration (Ni0 = 25.8%) and the highest reduction ratio (Ni^0/NiO = 0.90), while simultaneously having the best reduced state defect population (Ce^{3+}/Ce^{4+} = 0.506). Meanwhile, the largest fails to preserve its support defects ($\Delta Ce^{3+} = -5.2\%$, negative spillover-linked reducibility). This behaviour shows that the strong MSI could overly oxidize and lock the Ni in smaller particles of ceria, and larger particles of Ni may have a decreased reducibility in the ceria due to weak MSI and lower spillover. However, since the bare ceria support's own oxygen vacancy mobility is also known to vary with particle size independent of metal loading [74, 75], this trend may equally reflect a property of the ceria itself rather than Ni-CeO_2 bond strength specifically. Distinguishing between these two possibilities, would require comparing bare-support reducibility against the loaded catalyst directly and would also benefit from a direct spillover confirmation through H_2-TPR. The lower metallic Ni content may be due to partial oxidation during the ex-situ reduction and transfer of the samples, but the trends between different samples are still comparable.

Table 3.6: XPS summary of Ni/CeO_2 catalysts for all CeO_2 particle sizes, pre- and post-reduction (reduction at 300 °C for 4 h under a flow of 20 vol% H_2 in He).

Ce 3d Region

Sample	State	Ce^{3+} (%)	Ce^{4+} (%)	Ce^{3+}/Ce^{4+}	ΔCe^{3+} after reduction (%)
9-O (smallest CeO_2)					
9-O	Pre	9.0	91.0	0.099	—
9-O	Post	25.4	74.6	0.340	16.4
20-O (medium CeO_2)					
20-O	Pre	26.2	73.8	0.355	—
20-O	Post	33.6	66.4	0.506	7.4
29-O (largest CeO_2)					
29-O	Pre	34.1	65.9	0.518	—
29-O	Post	29.0	71.0	0.408	−5.2

Ni 2p Region

Sample	State	Ni^0 (%)	NiO bulk (%)	Ni^{2+}–CeO_2 (%)[a]	Ni^0/NiO
9-O (smallest CeO_2)					
9-O	Pre	3.9	44.8	51.3	0.09
9-O	Post	7.1	37.9	55.0	0.19
20-O (medium CeO_2)					
20-O	Pre	1.0	45.0	54.0	0.02
20-O	Post	25.8	28.8	45.4	0.90
29-O (largest CeO_2)					
29-O	Pre	4.5	40.4	55.1	0.11
29-O	Post	20.9	33.0	46.1	0.63

[a] Hydroxide phase is identified to be Ni^{2+}–CeO_2 in Ni/CeO_2 catalysts [68].

3.1.2 | Catalytic Performance

Consistent with the results of dispersion (CO chemisorption) and reduced defect state population (XPS) Ni/CeO2-20-O produces the best performance at 200-300 °C as in Figure 3.7, closely followed by Ni/CeO2-23-O. Reported activities are normalized using the ICP-OES-determined Ni weight fraction rather than the nominal loading, ensuring rates reflect the actual Ni content of each catalyst. All catalysts exhibits substantial low temperature activity with appreciable methane formation rate at 200 °C as seen in Figure 3.8a, this temperature was selected specifically to resolve the particle-size dependence of activity while keeping conversion low enough to avoid the CO-inhibition and equilibrium-approach effects that can obscure genuine structure–activity trends at higher conversion. The effect of particle size on performance could be clearly seen in Figure 3.8b. The selectivity itself seems to be optimized at ceria particle size of 15 nm while conversion is optimized at 20 nm, with both properties falling off sharply at the largest particle size (29 nm). Observed qualitatively, it can be inferred at the largest ceria particle size, there may be a different pathway preference. Conversion itself is noted to be heavily dependent on surface

oxygen vacancy on one part, as it determines the activation energy of C-O bond cleavage [15, 52, 76]. The XPS data on Ce^{3+}/Ce^{4+} is consistent with the conversion optimum. On the other part, Ni dispersion is proposed to govern the subsequent methanation step, affecting selectivity [3]. Because both properties are simultaneously reshaped by changing CeO_2 particle size, which alters oxygen vacancy density, dispersion, and pore structure together, this is interpreted as a manifestation of ceria-mediated metal–support interaction (MSI), the origin of which is interrogated directly via a calcination-temperature control series in Section 3.2.1 [57].

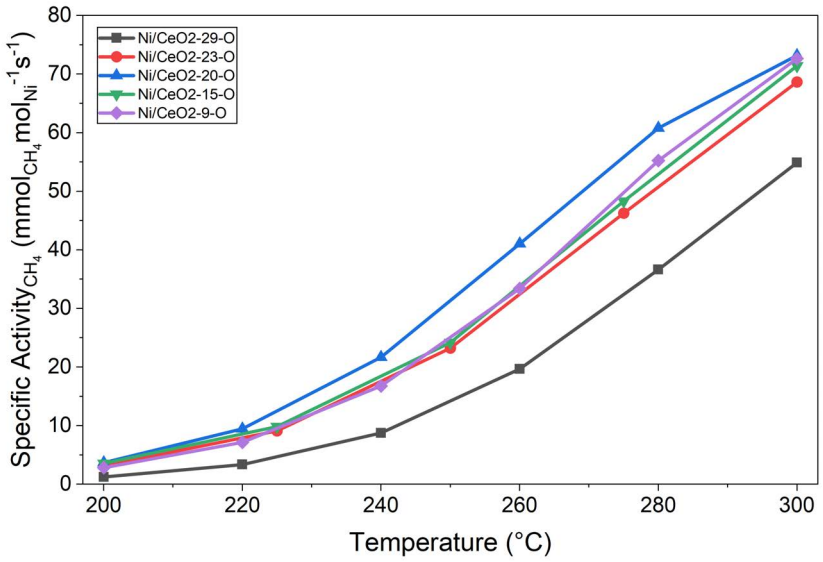

Figure 3.7: CH_4 specific activity of Ni/CeO_2 with different CeO_2 particle sizes.

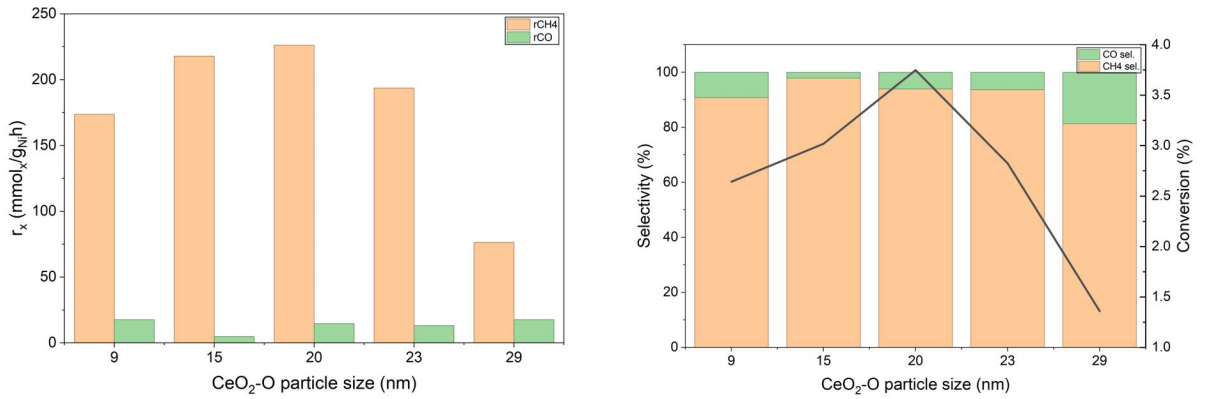

(a) Formation rate of CH_4 at 200 °C.

(b) CO_2 conversion and product selectivity at 200 °C.

Figure 3.8: Reaction performance of Ni/CeO_2 with different CeO_2 particle size at 200 °C.

To identify which catalyst property best predicts activity, mass-normalized CH_4 formation rate was regressed against various properties of Ni-CeO_2 (Figure 3.9): CO chemisorbed, surface Ni sites, H_2 consumed (TPR), BET surface area, and calculated Ni–CeO_2 interfacial site density B.6. CO chemisorbed and surface Ni sites are, by construction, linear transforms of the same chemisorption measurement and unsurprisingly return identical fits (R^2 = 0.916). Ni-CeO_2 interfacial sites, calculated from this same dispersion data, return a marginally higher R^2 of 0.945 consistent with, though not decisively distinct from, the chemisorption-derived metrics, given that all three descend from a single underlying measurement of Ni dispersion. The more informative comparisons are the two metrics that are not derived from surface Ni chemisorption: total H_2 consumption from TPR (R^2 = 0.517), which captures bulk in addition to surface reduction, and BET surface area (R^2 = -0.028), which reflects total textural area rather than accessible Ni. The near-total absence of correlation with BET area indicates that gross textural surface

area is not what governs activity, while the markedly weaker H_2-TPR correlation suggests that bulk reducibility is a poorer predictor than surface-specific Ni accessibility. Together, these two independent negative/weak controls support the conclusion that activity is shown to be affected specifically by accessible surface Ni, rather than by the catalyst's overall porosity or by Ni that remains reducible but subsurface.

To test whether the Ni–CeO_2 interface specifically, rather than surface Ni generally, is required for activity, a comparison sample of Ni/SiO_2 (Ni = 4 nm, comparable particle size, courtesy of M. Verstraten) was included in Figure 3.10. This sample, lacking a ceria interface, provides an approximate zero-interfacial-site data point. Including it actually increases the already strong correlation to $R^2 = 0.982$, and more importantly, the Ni/SiO_2 sample still exhibits nonzero methanation activity. This indicates that Ni retains baseline catalytic activity independent of any ceria interface, and that the Ni–CeO_2 interfacial site is better interpreted as an additive, rate-enhancing contribution on top of this intrinsic Ni activity, rather than as an absolute prerequisite for methanation, consistent with prior work identifying the metal–support interfacial region as an important but not exclusive contributor to CO_2 methanation activity on Ni/CeO_2 [70, 77, 78]. The reaction testing for Ni/SiO_2 was carried out at the same temperature (T = 200 °C) and same H_2/CO_2 ratio but with more catalyst and less dilution (50 mg catalyst and 100 mg SiC). It is still comparable as it is normalized by Ni weight (3.24%) of the catalyst but there may be an effect of local heating (hot spot) as there is more catalyst being used in an exothermic reaction, creating a higher apparent normalized activity at the same set temperature [79]. To provide a stronger support for the interfacial-site postulation, site analysis across different morphological variations is explored in Section 3.2.2.

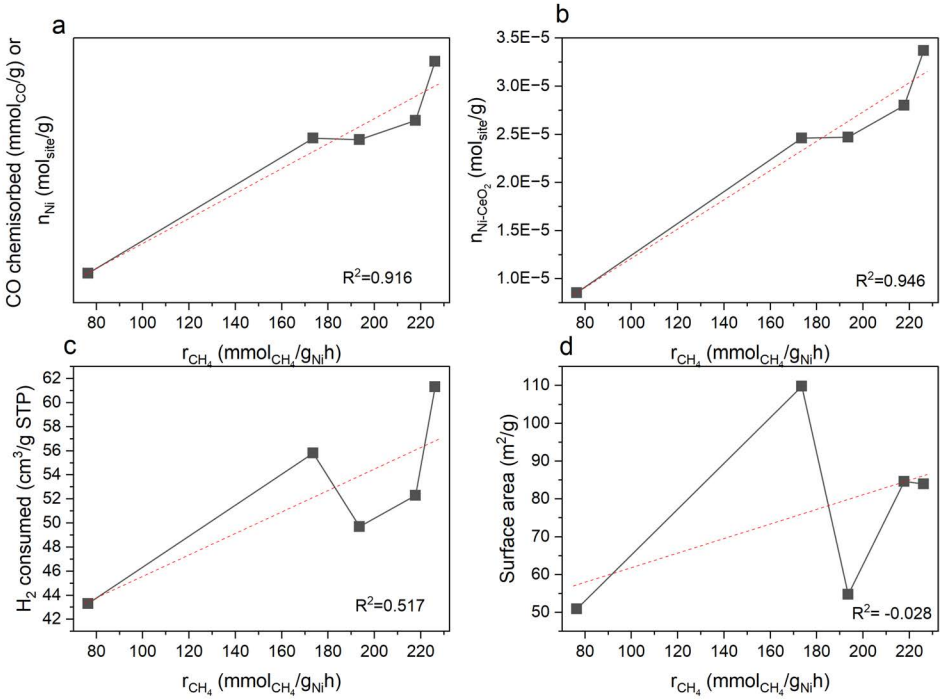

Figure 3.9: Active site postulation by linear regression of catalyst characteristics, (a) CO chemisorbed and Ni sites, (b) Ni-CeO_2 interfacial sites, (c) H_2 consumed, and (d) surface area.

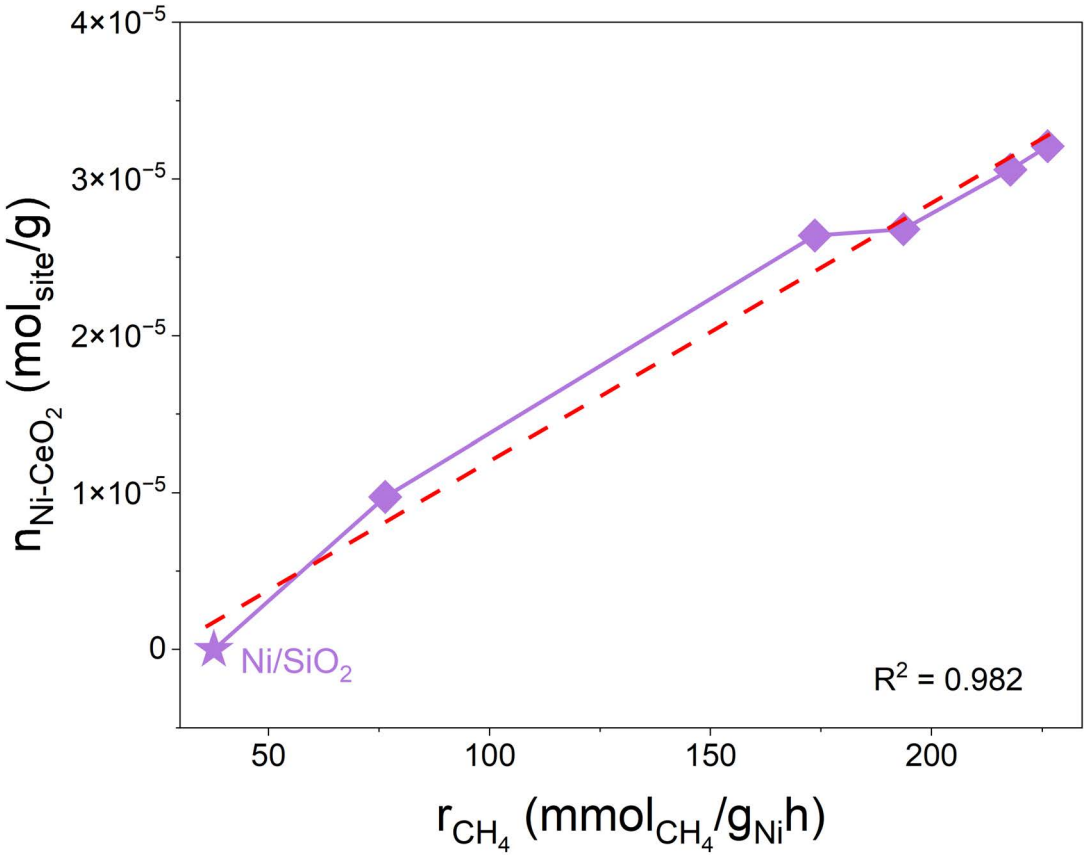

Figure 3.10: Active site postulation by linear regression of CeO_2 interfacial sites with inclusion of Ni/SiO_2.

Normalizing catalytic activity by catalyst mass and by surface Ni obtained from CO chemisorption yields two complementary views of the particle-size dependence of CO_2 methanation at 200 °C (Figures 3.11 and 3.12). The mass-normalized rates of both CO_2 consumption and CH_4 formation exhibit a clear, coincident optimum between 15 and 20 nm CeO_2, mirroring the non-monotonic Ni dispersion trend (Figure 3.4). This correspondence follows directly from the relationship $r_{CH_4} = \text{TOF} \times (M_w)^{-1} \times D$, where D is the fraction of surface-exposed Ni.

Turnover frequency for CO_2 conversion normalized by total surface Ni (Figure 3.12) shows a modest maximum at 20 nm (0.0153 s^{-1}), a ∼17% spread relative to the 9 nm value (0.0131 s^{-1}) across the 9–23 nm window, before declining to 0.0104 s^{-1} at 29 nm. This indicates that the structure sensitivity apparent when TOF is normalized by total surface Ni is a site-counting artifact, rather than reflecting a change in per-site reactivity across 9-23 nm it appears to reflect how the surface Ni fraction residing specifically at the Ni-CeO_2 interface (as opposed to total exposed Ni) varies with particle size, tracking the same synthesis-driven dispersion trend. CO formation follows a related pattern: it remains low and relatively flat across 9-23 nm under both normalizations, but shows the same qualitative break at 29 nm seen for CO_2 and CH_4 (rising from 0.004-0.019 s^{-1} across 9–23 nm to 0.050 s^{-1} at 29 nm under interfacial normalization), suggesting the 29 nm anomaly reflects a coherent shift in reaction character affecting all three products rather than a change confined to the methanation-selectivity step alone.

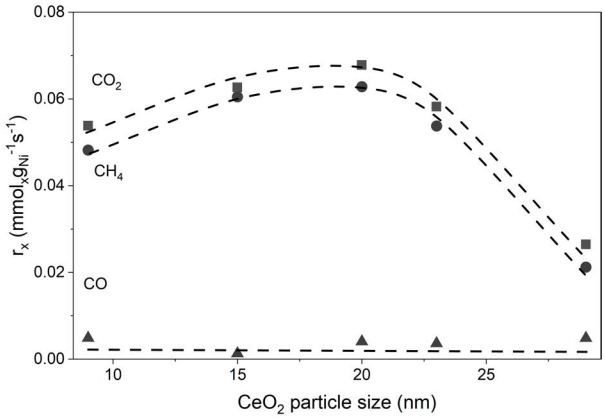

Figure 3.11: Normalized activity by Ni mass vs CeO_2 particle size.

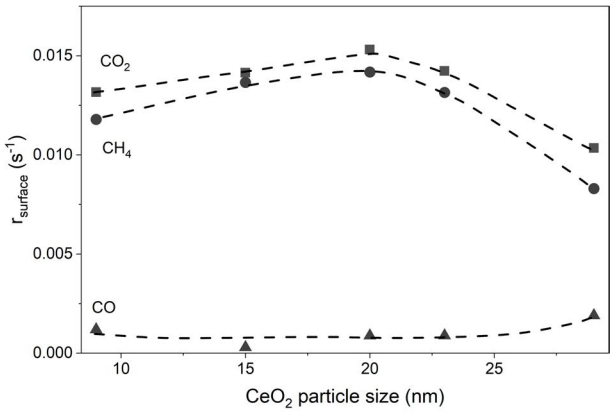

Figure 3.12: TOF normalized by surface Ni vs CeO_2 particle size.

The apparent activation energies of the catalysts calcined at 400 °C in the range of 185-200 °C itself have been observed to not vary markedly in respect to the particle size (9-29 nm of Ceria), resulting in 76-79 kJ/mol in Ni/CeO_2-O as in Figure 3.13. The small variation in the apparent activation energies is contributed to the effect of nickel-ceria interface, as a resulting effect of CeO_2 particle size [75]. The effect of different calcination temperature contributing to different apparent energy variations across similar CeO_2 particle size is explored in the next section (3.2.1)

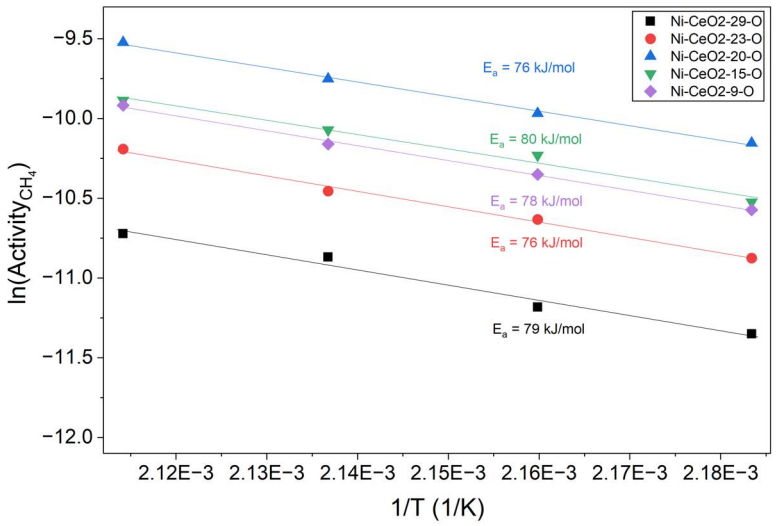

Figure 3.13: Particle size effect of Ni/CeO_2-O on kinetics and apparent activation energy from 185–200 °C under 20 vol% H_2, 5 vol% CO_2, and 75 vol% He at a total flow rate of 50 mL min^{-1}; pre-reduction at 300 °C for 4 h under a flow of 20 vol% H_2 in He (5 °C min^{-1}).

The formate intermediate was able to be identified in the switching of gas concentration in the FTIR for all catalysts in Figures Figures B.12 to B.16. Different CO adsorption mechanisms are observed as linear (2045 cm^{-1}) , bridged CO (1920 cm^{-1}) and hollow CO (1850 cm^{-1}) on Ni, consistent with previous assumptions for CO chemisorption [57]. The C=O stretching modes of bidentate carbonates (1750 cm^{-1}) and asymmetric stretching of O-C-O (1585 cm^{-1}) of the bidentate formate on CeO_2 can be observed [57,80]. The intensity of the peak were normalized between catalysts variation according to mass and signal response.

Under the CO_2+H_2→H_2 switch, in which CO_2 is removed from the feed while H_2 is retained, the formate (HCOO*) band decreased over the 0–4 min window, alongside a corresponding decrease in the adsorbed CO band observed in Figure B.17. Because no external carbon source is available to the catalyst under CO_2-free conditions, this decline reflects consumption of the pre-existing surface carbon pool rather than replenishment followed by turnover. This behavior, together with the responsiveness of the formate signal to H_2 availability observed in the CO_2+H_2→CO_2 and CO_2→CO_2+H_2 switches, supports the assignment of formate as a genuine, kinetically relevant surface intermediate rather than a spectator species. Formate concentration consistently tracks H_2 availability and is depleted under conditions where hydrogenation is favored and no further CO_2 activation can occur to sustain it [81,82]. We therefore consider the present data sufficient to support formate as one of the reactive surface intermediate under CO_2 methanation conditions on Ni/CeO_2. We do not, however, use this switch to draw conclusions regarding the rate or extent of CH_4 formation during this window, as quantitative gas-phase analysis (e.g., online MS or GC) was not available to independently verify the methanation output corresponding to this surface transient.

We also could not confirm directly the existence of the subsequent CO_2 → HCOO* → CO* → CH_4 pathway which is proposed and validated for reducible supported catalysts in CO_2 methanation [52,54]. This is due to the fact we could not isolate the contribution of CO_2 → CO* in the reaction. A finer grid for a more controlled reaction is needed using SSITKA and isotope switching.

3.2 | Synthesis Parameter Tuning

3.2.1 | Calcination Temperature Tuning

3.2.1.1 | Characterization

This calcination temperature series provides a second, independent test of the MSI–reducibility relationship proposed in Section 3.1 for the particle-size series, here keeping CeO_2 size approximately fixed while varying calcination temperature. The resulting crystalline properties of the catalysts calcined at 350 °C

were obtained as in Table 3.7 and Figure 3.14. It is noted that the Ni particle size for Ni/CeO2-9-O-350 and Ni/CeO2-17-O-350 was not able to be fitted as the peak was far too small and blended with the background noise as written in Table B.2. The aforementioned pore collapse and subsequent coalescence could be absent at this lower temperature, although this idea needs to be proven through textural properties study post calcination, the extremely small particle size indicates the lack of large Ni particles as its consequence. This may indicate the absence of Ni particle size minimum at Ni/CeO2-20-O-350, a different pattern than partcle size tuning at calcination temperature of 400 °C.

Table 3.7: XRD particle size of CeO_2 and Ni for Ni/CeO_2 catalysts calcined at $T_{calc} = 350$ °C.

Catalyst	Particle Size CeO_2 (nm)	Particle Size Ni (nm)
Ni/CeO2-9-O-350	9.3	—
Ni/CeO2-17-O-350	16.6	—
Ni/CeO2-20-O-350	20.4	5.4
Ni/CeO2-30-O-350	29.9	10.5

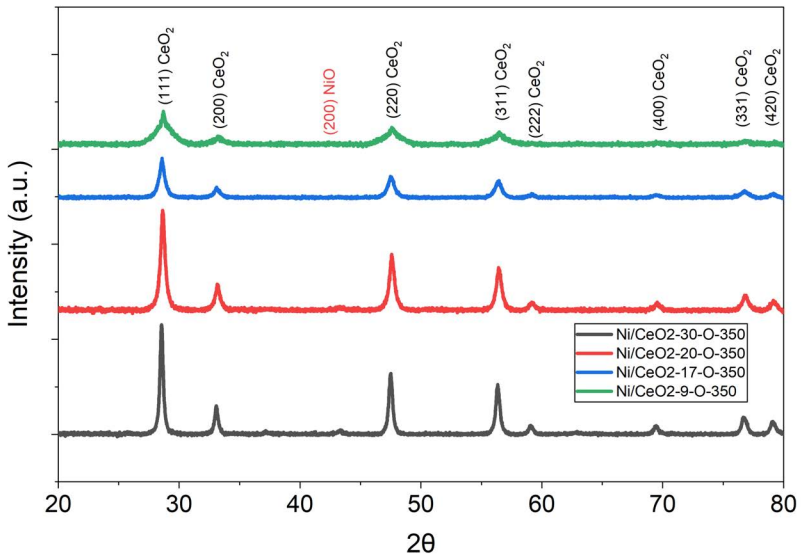

Figure 3.14: XRD of Ni/CeO_2-O particle size variation at calcination temperature of 350 °C.

The calcination temperature heavily affects the reduction degree of Ni at 20 nm particle size of CeO_2 shown in Table 3.8 and B.10. In addition to lower metallic Ni0 fraction post-reduction (15.3% vs. 25.8%), observing Table 3.7, the lower calcination temperature (350 °C) also corresponds to a larger Ni crystallite size (5.4 nm vs. the 4.8 nm value at 400 °C calcination). One interpretation is that weaker Ni-CeO_2 interaction at lower calcination temperature permits greater Ni at larger support sizes, and the resulting lower metallic fraction reflects either a genuinely higher reduction temperature for the larger particles or simply less complete reduction under the fixed 300 °C/4h treatment used here [83]. It is noted that the direction of this size-reducibility relationship is not consistent across the literature, Ru and Rh size series report the opposite trend (larger metal particles reducing more easily) [75, 84], while Ni-loading series on fixed supports report the same direction observed here (larger Ni, higher reduction temperature) [83]. This metal-dependence, rather than a universal MSI rule, is the most likely explanation for the difference.

Assuming bare CeO_2's own reduction capability does not vary between 350 and 400 °C, untested here, and the same open question flagged for particle size in Section 3.1, the observed Ce^{3+}/Ce^{4+} difference is consistent with a calcination-temperature-dependent, Ni-mediated spillover effect, though a contribution from the bare support's own temperature-dependent reducibility cannot be excluded. However, this link should be treated as a hypothesis rather than an established mechanism: Hao et al. report a Ni particle-size series where reduction-peak temperature shifts substantially (546→574 K) while an independently measured spillover-linked excess-H_2 signal remains essentially flat, indicating that a shift in reduction

temperature does not necessarily track a proportional shift in spillover [83]. Confirming the proposed link here would benefit from a spillover-specific measurement (H_2-TPR, concurring with particle size tuning) rather than inferring it solely from the reduction-peak shift.

Table 3.8: Effect of calcination temperature on Ni/CeO2-20-O: XPS comparison (post-reduction).

Ce 3d Region

Calcination T (°C)	Ce^{3+} (%)	Ce^{4+} (%)	Ce^{3+}/Ce^{4+}
350	28.3	71.7	0.395
400	33.6	66.4	0.506

Ni 2p Region

Calcination T (°C)	Ni^0 (%)	NiO bulk (%)	Ni^{2+}–CeO_2 (%)	Ni^0/NiO
350	15.3	64.6	28.2	0.24
400	25.8	27.1	42.7	0.95

3.2.1.2 | Catalytic Performance

In a different calcination temperature, the trend of methane formation activity in the range of 350-400 °C stays the same with ceria at 20 nm as the optimum as seen in Figure 3.15. However, when looking at CO_2 consumption in Figure 3.16a, Ni/CeO2-9-350 is actually the most active, even showing an almost linear relationship of activity against particle size. Observing Figure 3.16b, The selectivity towards CO has substantially increased at 9 nm with the decrease of calcination temperature. The 20 nm ceria support maintains its optimum point, as moderate metal-support interaction appears to optimize intermediate binding energies to maximize methane turnover, while avoiding agglomeration which occurs at 30 nm supports (large Ni particles) and ultra dispersion of Ni (high CO selectivity) at lower size supports, which is discussed more in detail in Section 4.2. The global suppression of the CO_2 consumption rate (r_{CO_2}) for the entire 350 °C calcination series relative to the 400 °C counterparts indicates a lower intrinsic quality and density of active metal-support interfacial sites. This highlights the importance of MSI not only as a support particle size sensitive property, but also as a temperature tunable property [85].

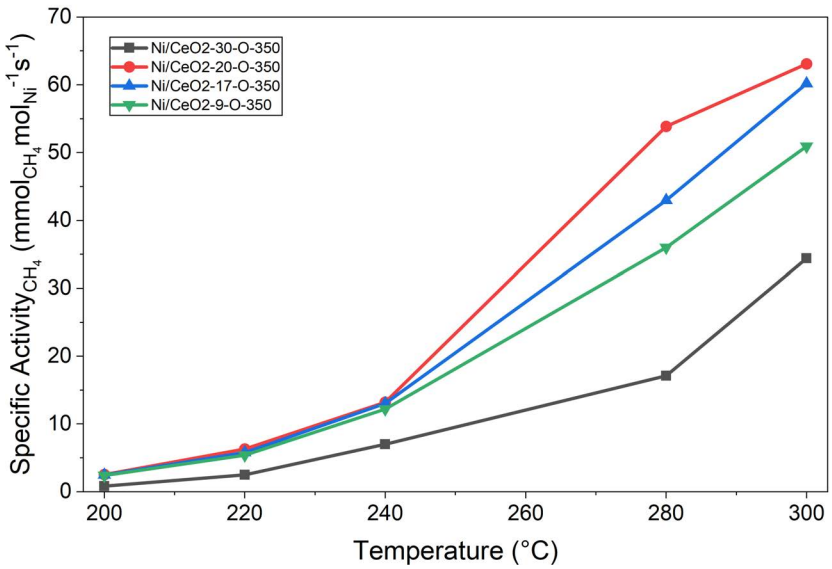

Figure 3.15: CeO_2 particle size effect of Ni/CeO_2-O on CH_4 specific activity at calcination temperature of 350 °C.

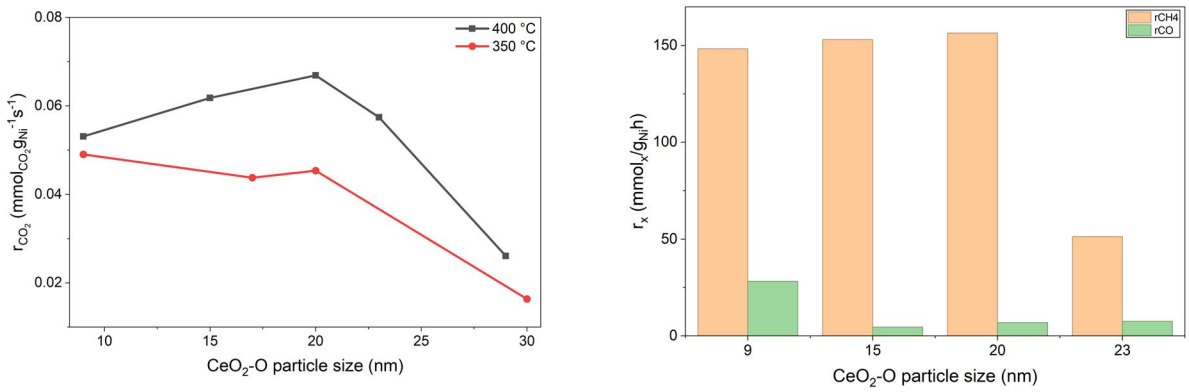

(a) Consumption rate of CO_2 at 200 °C. **(b)** Formation rate of CH_4 at 200 °C.

Figure 3.16: Particle size effect of Ni/CeO_2-O-350 on catalytic performance at 200 °C.

Observing the activation energy, it rises from 83 kJ/mol at 9 nm, to 93 kJ/mol at both 17 nm and 20 nm, and increasing to 111 kJ/mol at 30 nm (Figure 3.17. The inverse relationship between activation energy and CO_2 consumption is a classic Arrhenius relationship of lower apparent barrier and higher overall conversion rate. However, this does not apply to methane formation, again indicating that the initial CO_2 activation step (reflected in total rCO_2) is not limited by CeO_2 particle size, but the efficiency of $^*CO$ hydrogenation to CH_4 is. The 30 nm sample is the exception to this otherwise clean separation, it is the weakest performer overall and carries the highest Ea of the series. This suggests that at this particle size, unlike within the 9–20 nm window, a different mechanism and relationship could be observed. Further experimental standing through CO chemisorption and XPS may be required.

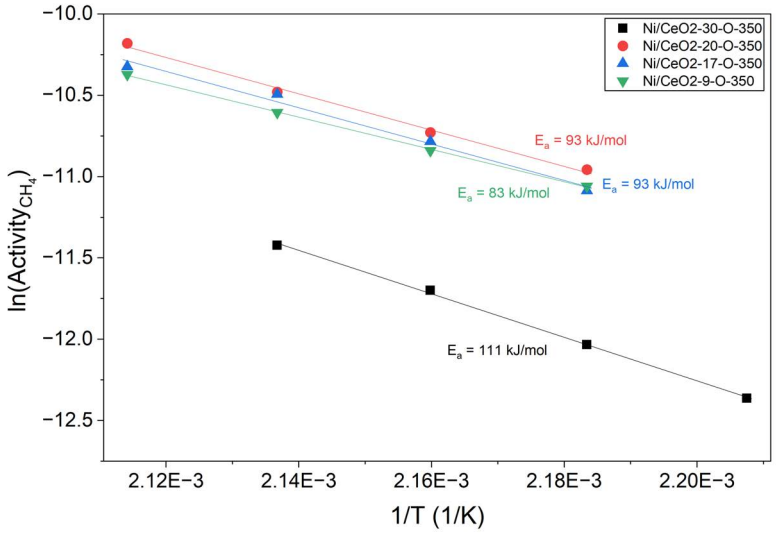

Figure 3.17: Particle size effect of Ni/CeO_2-O-350 on kinetics and apparent activation energy from 180–200 °C under 20 vol% H_2, 5 vol% CO_2, and 75 vol% He at a total flow rate of 50 mL min^{-1}; pre-reduction at 300 °C for 4 h under a flow of 20 vol% H_2 in He (5 °C min^{-1}).

3.2.2 | Morphology tuning

The primary objective of this subchapter is to isolate the role of support surface-to-volume ratio, specifically comparing flame-spray-pyrolysis (FSP) derived octahedral ({111} domains), hydrothermally aged cubic ({100} planes), and directly calcined spherical nanoparticles, at fixed incipient wetness impregnation (IWI) parameters and comparable surface-to-volume metrics. XRD measures the coherent scattering domain length *perpendicular* to the diffracting plane, in this case the (111) plane of CeO_2. This quantity, D_{XRD}, is therefore *not* directly equivalent to the diameter of a sphere, the edge length of a cube, or the

edge length of an octahedron [35, 86]. Sample labels (9-O, 15-C, 9-S) reflect the nominal $D_{XRD}(111)$ size targeted during synthesis; because this quantity is not directly comparable across particle shapes (Eq. 3.1), Table 3.9 converts each to the shape-appropriate Sauter mean diameter d_{32}, confirming the three samples are size-matched (8.7–9 nm) on this surface-area-weighted basis. Turnover frequencies below are normalized independently, using surface Ni determined by CO chemisorption [34].

$$D_{\mathrm{XRD}} \neq D_{\mathrm{sph}} \neq a_{\mathrm{cub}} \neq a_{\mathrm{oct}} \tag{3.1}$$

Table 3.9: Geometric conversion of the XRD (111) coherent domain size D_{XRD} to the Sauter mean diameter for three idealised particle morphologies, illustrated for $D_{\mathrm{XRD}}(111) \approx 9$–15 nm [34, 35].

Parameter	**Octahedron**	**Cube**	**Sphere**
$D_{\mathrm{XRD}}(111)$ (nm)	9	15	9
Conversion factor	$a\left(\sqrt{2/3}\right)$	$a\left(\sqrt{3}\right)$	D
Edge / diameter (nm)	$a = 12.25$	$a = 8.66$	$d = 9$
Volume	$\left(\sqrt{2}/3\right) a^3$	a^3	$(\pi/6)\, d^3$
Surface area	$3.464\, a^2$	$6a^2$	πd^2
Sauter diameter (nm)	**9**	**8.66**	**9**

3.2.2.1 | Characterization

Properties related to crystallite and particle size of the catalyst are summarized as in Table 3.10. In Figure 3.18, the spectra for each variation can be seen with peak fittings as in Table B.3. The large discrepancy in chemisorption and XRD data of Ni for cubic ($D_{XRD} \gg D_{Chemi}$) and spherical ($D_{XRD} < D_{Chemi}$) morphologies indicate a different crystallinity behaviour of Ni on each morphology which caused the overall particle size to not be reliable. Therefore for particle size (irrespective of crystallinity) determination of Ni/CeO_2 at different morphologies, chemisorption would be most reliable.

Table 3.10: Summary of CeO_2 and Ni characterization data for the Ni/CeO_2 morphology tuning series (nominal Ni wt% used).

	CeO_2 Properties		**Ni Properties**		
Catalyst	D_{SA} **(nm)**	D_{XRD} **(nm)**	D_{XRD} **(nm)**	D_{Chemi} **(nm)**	**Dispersion (%)**
Ni/CeO2-9-O	9.0	9.4	5.3	4.4	22
Ni/CeO2-15-C	8.7	15.3	29.5	7.1	14
Ni/CeO2-9-S	9.0	8.7	—	5.4	18

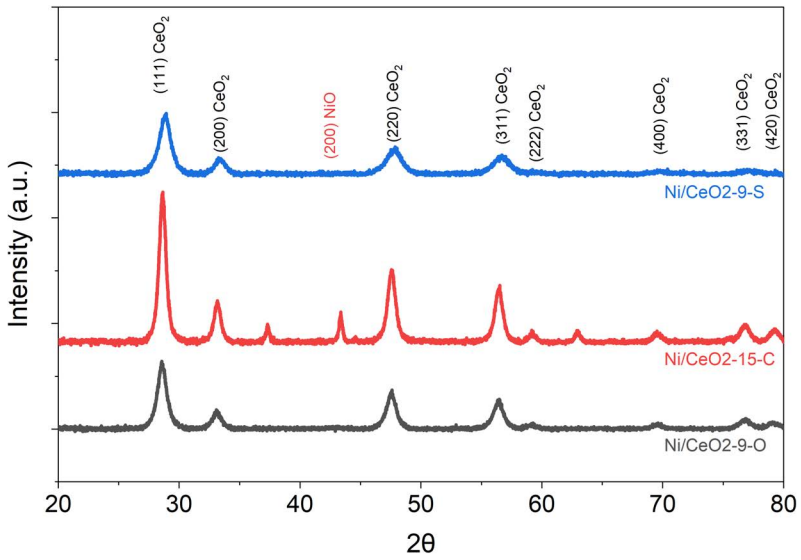

Figure 3.18: XRD of Ni/CeO_2-O morphology variation.

It can be noted that the dispersion of Ni itself is not equal across different morphologies at the same volume-to-surface-area ratio as in Figure 3.19 and tabulated in Table B.7. The chemisorbed CO is calculated over nominal Ni weight (10%) with individual CO chemisorption behaviour and measurements are displayed in Figure B.6. The distinct variations in dispersion are corroborated by the unique H_2 temperature-programmed reduction (H_2-TPR) profile observed for each morphology as in Figure 3.20, this behavior is indication of facet-controlled reduction process. Theoretically, bare CeO_2 surface energies show a stability trend of octahedral > spherical (mixed facet) > cubes and corresponding reducibility should follow the reverse trend [87]. However, the impregnation of transition metals is known to result in a reversed reduction behaviour [55].

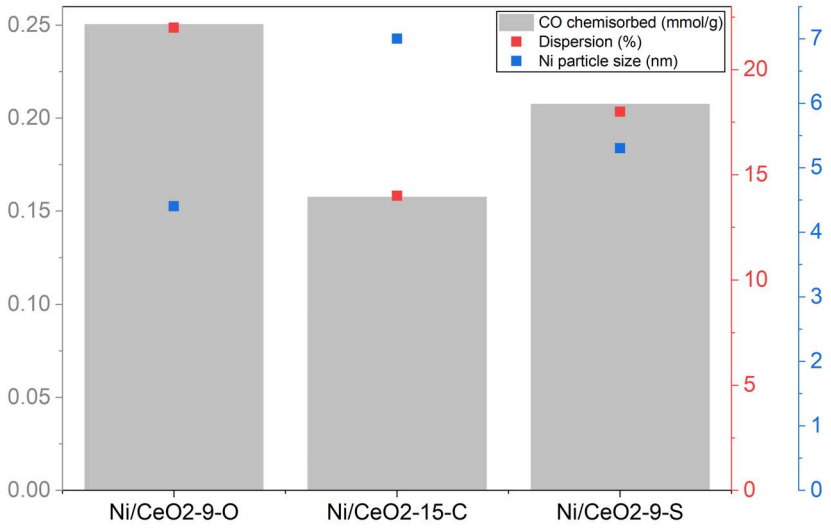

Figure 3.19: CO chemisorption results of Ni/CeO_2 morphology variation.

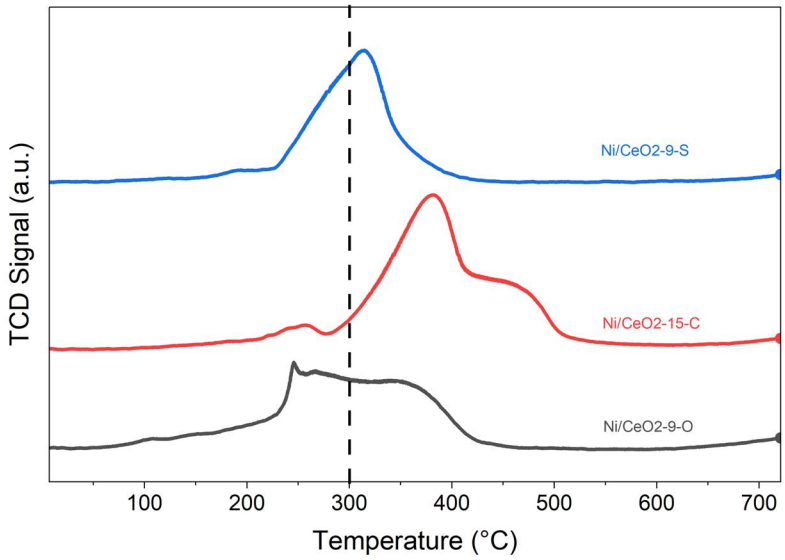

Figure 3.20: H_2-TPR of Ni/CeO_2 morphology variation, pretreated at 300 .

Bare ceria support textural properties of catalysts with different morphologies of ceria is summarized in Table 3.11. The bare pore volume and surface area seems to track with the dispersion. This allows for an understanding that pore properties, translates to Ni anchoring during impregnation and therefore interfacial site population, rather than morphology (octahedral, cubic, spherical) acting as an independent driver on its own, more so that variation in morphology causing the variation in pore volume [88]. However, more data post calcination is needed since morphology and synthesis-route-dependent texture vary together across this catalyst series The XPS properties of each catalyst as-prepared are tabulated in Figure 3.12. Ni/CeO2-9-S exhibits the highest initial reduced Ce concentration and largest highly bound and oxidized Ni-CeO_2 concentration. It would be interesting to explore the properties after reduction and how it changes.

Table 3.11: Texture properties of CeO_2 supports of morphology variation.

CeO_2 supports			
Catalyst	**BET Surface Area (m^2/g)**	**Pore Volume (cm^3/g)**	**Pore Diameter (Å)**
CeO_2-9-O	150.83	0.563	149.342
CeO_2-15-C	62.24	0.248	159.232
CeO_2-9-S	87.94	0.186	84.479

Table 3.12: XPS summary of Ni/CeO_2 catalysts for samples 9-O, 15-C, and 9-S (unreduced/as-prepared state).

Ce 3d Region

Sample	**Ce^{3+} (%)**	**Ce^{4+} (%)**	**Ce^{3+}/Ce^{4+}**
9-O	9.0	91.0	0.099
15-C	9.5	90.5	0.105
9-S	14.2	85.8	0.166

Ni 2p Region

Sample	**Ni^0 (%)**	**NiO bulk (%)**	**Ni^{2+}–CeO_2 (%)**	**Ni^0/NiO**
9-O	3.9	44.8	51.3	0.09
15-C	3.7	55.4	40.9	0.07
9-S	0.5	37.1	62.5	0.01

3.2.2.2 | Catalytic Performance

Catalytic performance of the three morphologies is shown in Figure 3.21. It can be observed that Ni/CeO2-9-O has the highest activity and methane formation rate, followed by Ni/CeO2-9-S and Ni/CeO2-15-C. The apparent activation energies are compiled as in 3.22. The apparent activation energies for the octahedral and spherical catalysts are nearly identical (78 and 77 kJ/mol, respectively), whereas the cubic catalyst shows a substantially higher barrier (94 kJ/mol). This is consistent with the cubic sample's anomalous behavior in the XRD/chemisorption particle-size discrepancy and its position as the performance, this suggests the cube-morphology catalyst may be operating under a genuinely different kinetic regime rather than simply a less-active version of the same mechanism. Within the dual-pathway framework established in Section 4.1, a higher apparent activation energy on the cubic sample would be consistent with more single-pathway-limited kinetics, paralleling the elevated activation energy Lou et al. report at particle-size extremes relative to their optimal intermediate-size catalyst [89].

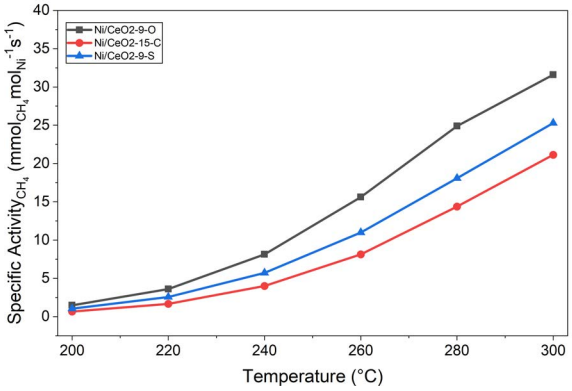

(a) Particle size effect of Ni/CeO_2-O on performance at different particle morphologies (nominal Ni wt% used).

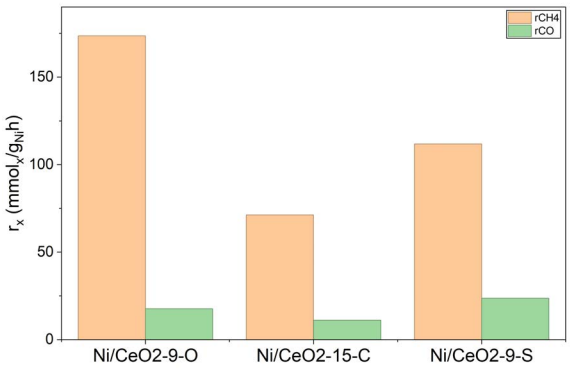

(b) Catalysts activity at 200 °C (nominal Ni wt% used).

Figure 3.21: Reaction performance of Ni/CeO_2 with different CeO_2 morphology.

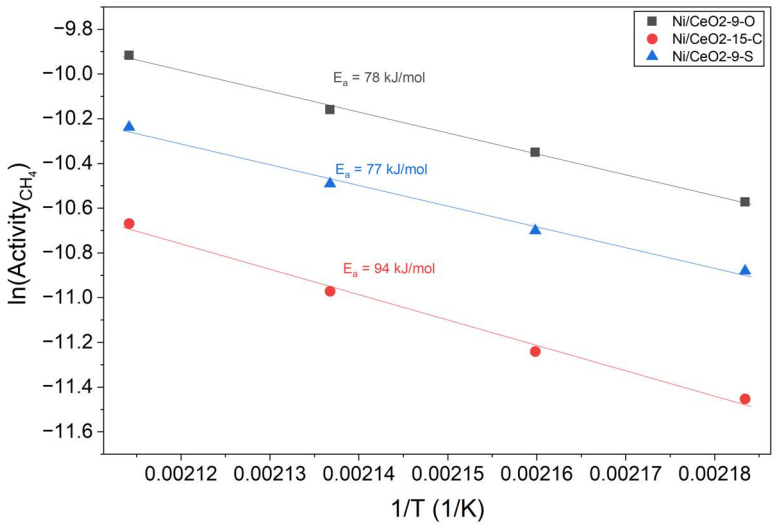

Figure 3.22: Morphology effect of Ni/CeO_2 on kinetics and apparent activation energy from 185–200 °C under 20 vol% H_2, 5 vol% CO_2, and 75 vol% He at a total flow rate of 50 mL min^{-1}; pre-reduction at 300 °C for 4 h under a flow of 20 vol% H_2 in He (5 °C min^{-1}).

The high correlation with interfacial area is followed by CO chemisorbed and Nickel amount as in Figure 3.23, the same relationship but with an even higher correlation ($R^2 = 0.982$ and $R^2 = 0.947$ respectively).

What is unique is that it also has a high correlation with its bare support area. This high correlation with the bare support surface area ($R^2 = 0.972$) provides a mechanistic link as summarized previously in Table 3.11, the geometric morphology directly dictates the initial textural properties of the ceria. A higher baseline support surface area (e.g. in the octahedral CeO2-9-O) inherently optimizes the structural landscape for Ni anchoring and dispersion during impregnation. Consequently, this maximizes the density of highly active interfacial zones. This strong, multi-variable convergence supports the conclusion that while morphology modulates the underlying textural architecture, the prominent apparent driver of the CO_2 methanation rate is the resulting population of interfacial sites, providing support for the active site postulation established in Section 3.1.

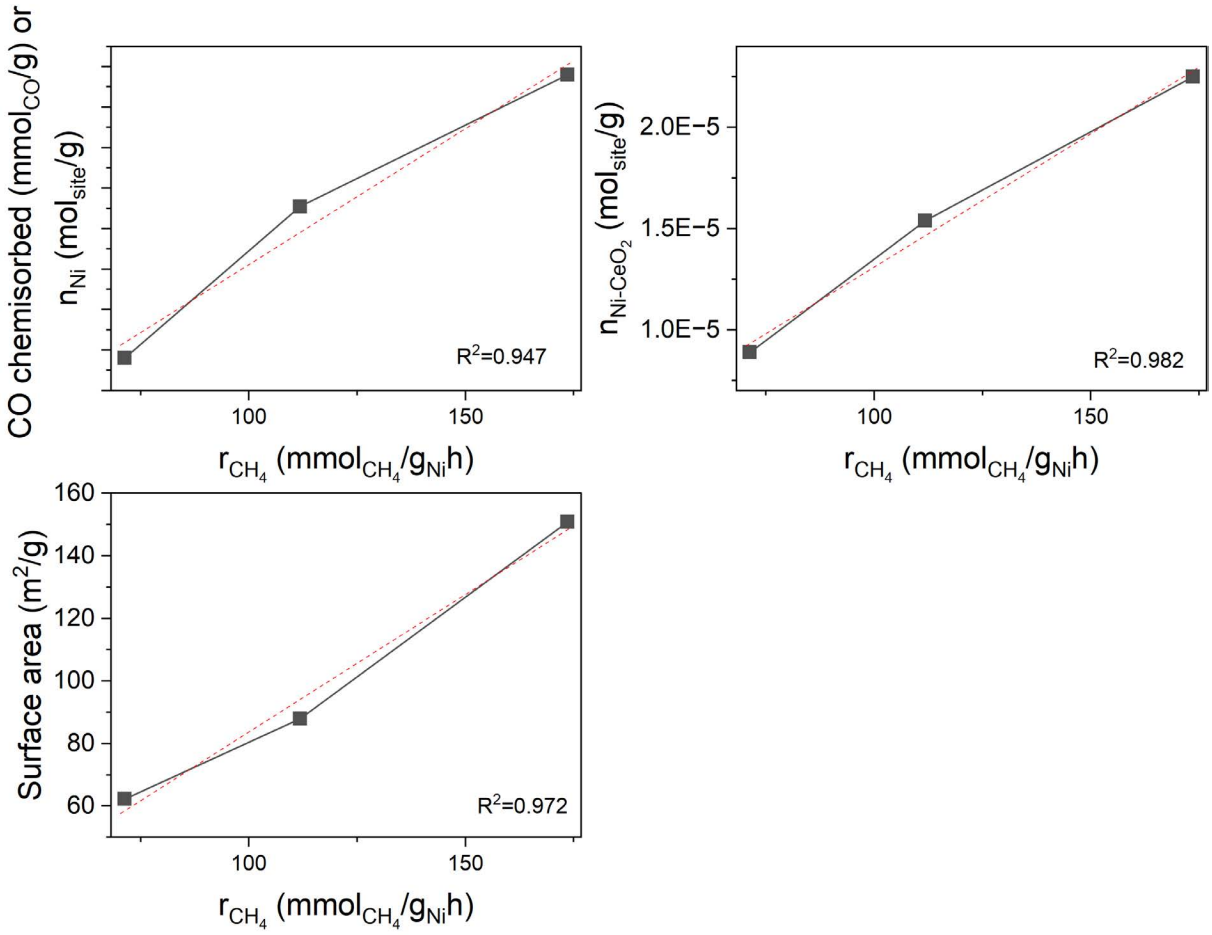

Figure 3.23: Active site determination by linear regression of catalyst characteristics, (a) CO chemisorbed and Ni sites, (b) Ni-CeO_2 interfacial sites, and (c) Bare support surface area (nominal Ni wt% used).

To complement mass-normalized activity (Figure 3.25) the surface-Ni-normalized TOF (Figure 3.24) was also calculated, both using nominal Ni wt% loading. Both metrics show the same qualitative pattern: Ni/CeO2-9-O highest, Ni/CeO2-15-C lowest, and Ni/CeO2-9-S intermediate. Because nominal loading was used, these mass-normalized values should be treated as approximate, any deviation between nominal and actual Ni content would shift these numbers without necessarily changing their relative ranking across the three morphologies. This indicates that while the effect of CeO_2 particle size may induce a slight oxygen vacancy change due to slight exposed facet variance, in a complete morphology change where the facet completely changes, the effect is amplified. This is explored more in Section 4.2.

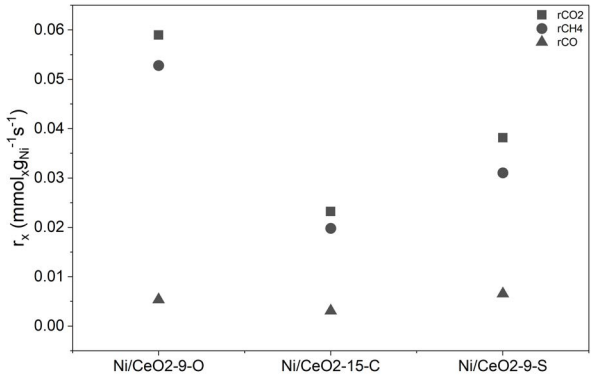

Figure 3.24: Normalized activity by Ni mass vs CeO_2 morphology variation.

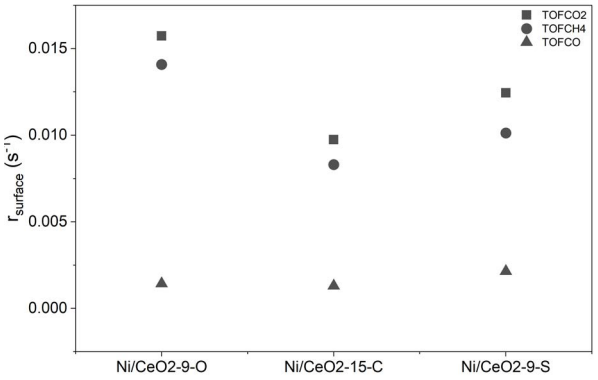

Figure 3.25: TOF normalized by surface Ni vs CeO_2 morphology variation.

4 | Mechanistic Insights and Metal-Support Interactions

4.1 | Catalytic Mechanism and Nature of the Active Site

Across the CeO_2 particle-size series (9–29 nm), the effect of support size on catalytic performance is best understood as indirect and synthesis-mediated rather than intrinsic to the ceria crystallites themselves. Mass-normalized CO_2 and CH_4 formation rates both show a clear optimum near 15–20 nm, but this tracks Ni dispersion (also peaking in the same window) rather than reflecting a change in per-site chemistry. The calcination-temperature control experiment (350 vs. 400 °C, CeO_2 size held fixed) provides supporting data, the non-monotonic Ni-size trend specific to 400 °C collapses into a monotonic one at 350 °C, showing the "optimum" is a thermally-activated synthesis artifact (pore-mouth collapse on fine-pored, high-surface-area supports, competing with insufficient nucleation sites on coarse, low-surface-area ones) rather than a property that would persist if the ceria crystallites' intrinsic redox/electronic character were what mattered. This is consistent with ceria being disproportionately prone to redox/vacancy-mediated surface mobility at mild temperatures compared to more thermally robust oxide supports — sintering-related deactivation in CuO–CeO_2/SiO_2 systems, for instance, is reported to require calcination temperatures of 600 °C and above, with the effect specifically attributed to ceria particle migration rather than the silica component [90] , while γ-Al_2O_3's major structural/pore degradation is generally not seen until 800–1100 °C.

Turnover frequency for CO_2 conversion normalized by total surface Ni is not perfectly constant across this series, showing a modest maximum at 20 nm before declining at 29 nm. The regression of interfacial site density against mass-normalized CH_4 formation rate (Figure 3.9 and 3.23) provides the most direct evidence that Ni-CeO_2 interfacial sites, rather than total surface Ni, are the primary kinetically relevant population in this system. The relationship is strongly linear ($R^2 = 0.982$) across the full particle-size series, and extrapolates through a near-zero, non-negative intercept represented by the Ni/SiO_2 control sample, which possesses no Ni–CeO_2 interface and correspondingly shows the lowest CH_4 formation rate in the dataset while still retaining measurable baseline activity. This is consistent with Ni itself carrying some intrinsic methanation activity independent of any oxide interface, with the ceria interface acting as an additive rate enhancement whose magnitude scales directly with interfacial site count. Therefore, the true structure-insensitive kinetic unit in this system appears to be the Ni-CeO_2 interfacial site specifically, which is the sub-population of surface Ni actually in contact with the support.

Taken together, this characterization dataset splits into properties that are essentially insensitive to $CeO2_2$ particle size and properties that are clearly sensitive to it. The apparent activation energy across 9–23 nm, and the strong correlation between interfacial site density and methane formation rate, both fall into the size-insensitive category, consistent with a dominant (interfacial) active site whose fundamental character does not change substantially across this window. Ni dispersion, particle size itself, reducibility (Ni0/NiO ratio), pore structure, and the interfacial fraction of surface Ni all fall into the size-sensitive category, and are governed principally by how much Ni disperses, and how it partitions between interfacial and terrace environments, during synthesis. What this work refines, however, is which population the "insensitive" label actually describes: it is the interfacial Ni sub-population specifically that behaves consistently, not surface Ni as a whole — a distinction only visible once interfacial site density is regressed separately from total surface Ni. CeO_2 particle size therefore matters primarily through how it constrains Ni nucleation, dispersion, and interfacial contact during the citrate-assisted impregnation and calcination protocol used here.

Figure 4.1 presents this proposed mechanism at the level of individual surface species, distinguishing connections confirmed directly by FTIR evidence (solid arrows) from those proposed but not yet independently verified (dashed arrows), most notably the direct $CO_2 \rightarrow {}^*CO$ route bypassing HCOO*, and the possibility that CeO_2-remote formate can, over longer timescales, still feed back into the productive cycle. This work could not directly isolate CO dissociation as a discrete step, though Wang et al. and Struijs et al. established this two-step pathway in related systems [29, 52]. The pathways in comparison are depicted in Figure 4.2.

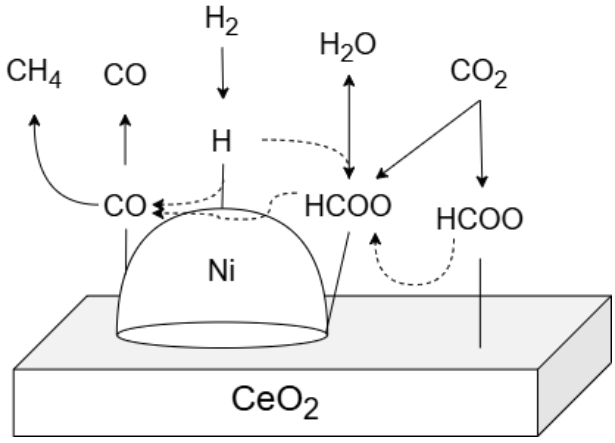

Figure 4.1: CH_4 mechanism on Ni/CeO_2 adapted from [29].

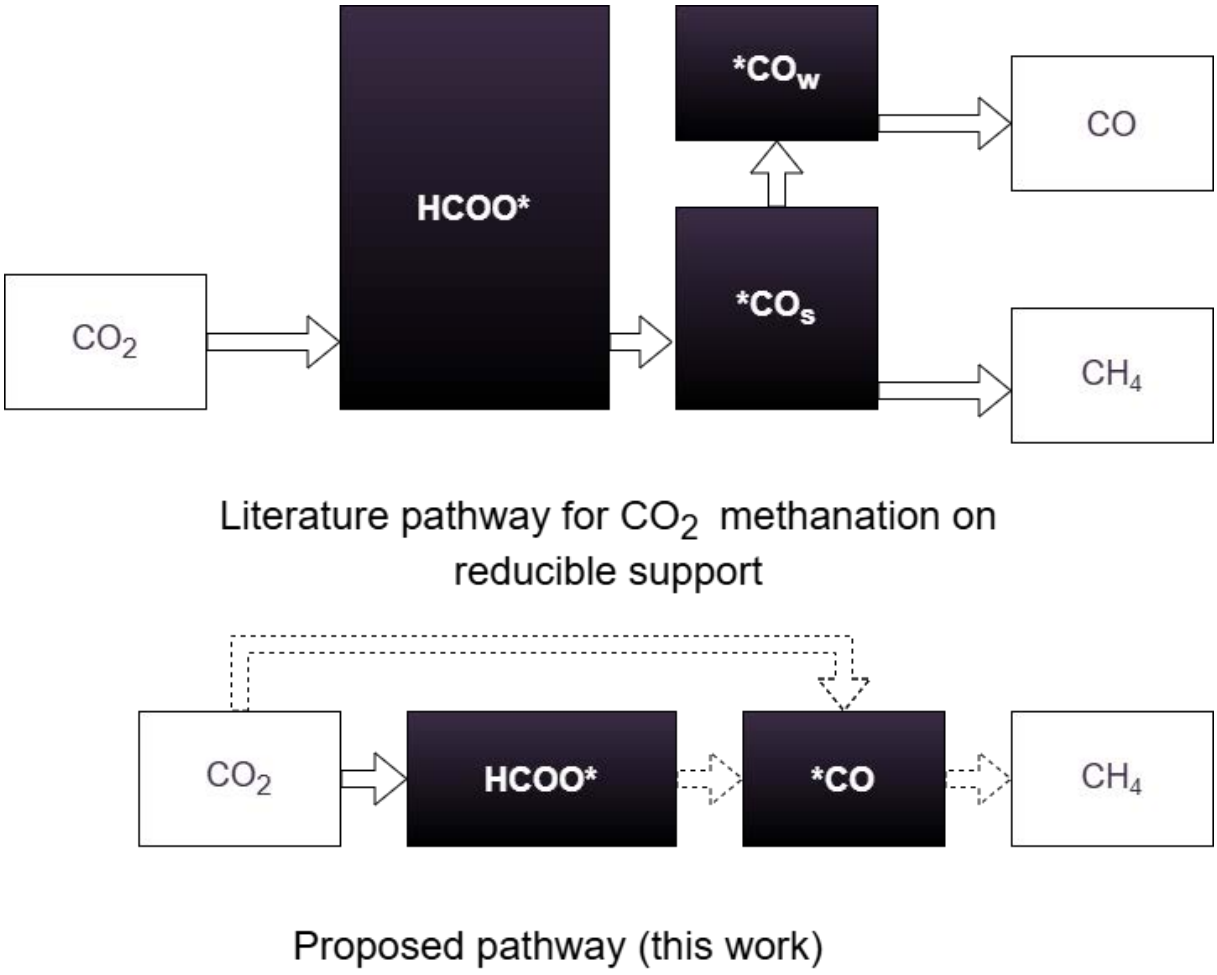

Figure 4.2: Literature pathway and proposed pathway.

4.2 | Electronic Tuning and Interfacial Thermodynamics: Literature Review

Within the d-band model of surface reactivity, the electronic structure of a transition metal surface, specifically the position of its d-band centroid relative to the Fermi level, governs adsorbate binding strength and, by extension, activation barriers for bond-making and bond-breaking steps [91, 92]. For a supported nanoparticle in direct contact with a reducible oxide, however, this picture must be extended

beyond simple coordination-driven band narrowing. At a Ni-CeO_2 interface, Ni atoms in direct bonding contact with the support can donate electron density into the empty Ce 4f band, oxidizing surface Ni and reducing adjacent Ce^{4+} to Ce^{3+}. Mao et al. directly quantified this process by single-crystal adsorption calorimetry and DFT for Ni on CeO_2(111), finding that the charge transferred per Ni atom is largest for the smallest clusters and decreases sharply as cluster size increases, that this charge is localized specifically to the Ni and Ce atoms in the atomic layers closest to the interface, and that Ce 3d XPS directly tracks the resulting increase in Ce^{3+}/Ce^{4+} ratio with Ni coverage [93].

This size-dependent charge-transfer trend is the same qualitative shape as ΔCe^{3+} measured across the present particle-size series (+16.4%, +7.4%, and −5.2% at 9, 20, and 29 nm; Table 3.6), and offers an atomic-level account of it. The transferred charge is localized to interfacial atoms rather than distributed across the whole particle: the total electron donation observed by bulk XPS scales with the fraction of total Ni residing at the Ni-CeO_2 interface, which is itself set by the same particle-size-dependent dispersion trend already established via the textural pathway (Section 4.1). Under this framing, the redox pathway is not an independent size effect competing with the textural one, but a direct electronic consequence of it: smaller CeO_2 particles, by promoting higher Ni dispersion, mechanically expose a larger fraction of total Ni to the interface, and it is this larger interfacial fraction, not a change in the intrinsic electronic character of a single Ni atom, that has been shown to manifest in a larger bulk-averaged ΔCe^{3+} signal and a correspondingly lower Ni^0 yield upon reduction (7.1% at 9 nm).

This interfacial-localization picture also offers a concrete atomic-level account of the apparent activation energy paradox between the 350 and 400 °C calcination series (Sections 3.1 and 3.2.1). Because charge transfer is confined to Ni atoms in direct interfacial bonds, its contribution to the observed kinetics should scale with the fraction of total Ni that remains in this oxidized, interfacially-bonded state, directly reflected in the Ni^0/NiO ratio, which rises from 0.24 to 0.95 between 350 and 400 °C at fixed 20 nm CeO_2 (Table 3.8). At 350 °C, incomplete reduction leaves a substantial, and strongly size-dependent, fraction of Ni in the charge-transferred interfacial state, consistent with the activation energy variation observed across particle size at this calcination temperature (83-111 kJ/mol). At 400 °C, more complete reduction dilutes this interfacial population relative to bulk-like metallic Ni across all particle sizes tested, consistent with the near-uniform Ea observed there (76-80 kJ/mol). This is specific to the redox pathway, i.e. it accounts for why the electronic signature of the interface converges with calcination temperature, but does not explain the textural (dispersion) optimum at 20 nm, which remains attributable to the synthesis-driven pore-collapse mechanism.

Particle-size-dependent d-electron redistribution is not always support-mediated: XANES studies of supported Au show smaller clusters retain more d-electron density through a purely intraparticle effect, with no measurable dependence on support composition [94]. The clear support-dependence of ΔCe^{3+} and Ni^0/NiO in the present work indicates the Ni/CeO_2 system is governed by the interfacial, support-mediated mechanism rather than this alternative, support-independent pathway. A DFT study comparing Ni as a surface adsorbate against Ni as a lattice substituent on CeO_2(110)/(100) shows these to be electronically distinct cases: a Ni adsorbate, the relevant geometry here raises the energy required to form an additional oxygen vacancy relative to bare ceria [95]. This indicates the ΔCe^{3+} signal reported throughout this thesis is better attributed to direct electronic charge transfer through existing interfacial bonds (as in [93]) rather than to Ni catalyzing the formation of new lattice vacancies, and the term spillover is used loosely in this sense rather than implying literal oxygen removal.

Figure 4.3 visualizes an attempt to close the loop between the redox and textural frameworks. Each arrow feeding into Fermi-level alignment corresponds to one of the three variables explored in this work: the particle size sets the interfacial fraction, calcination temperature sets what fraction of that interface remains in the charge-transferred state, and morphology sets the facet-dependent magnitude of transfer per interfacial atom. The diagram's two outcome boxes map accordingly the textural and redox pathways, with each of the three tuning studies contributing as an apparent effect.

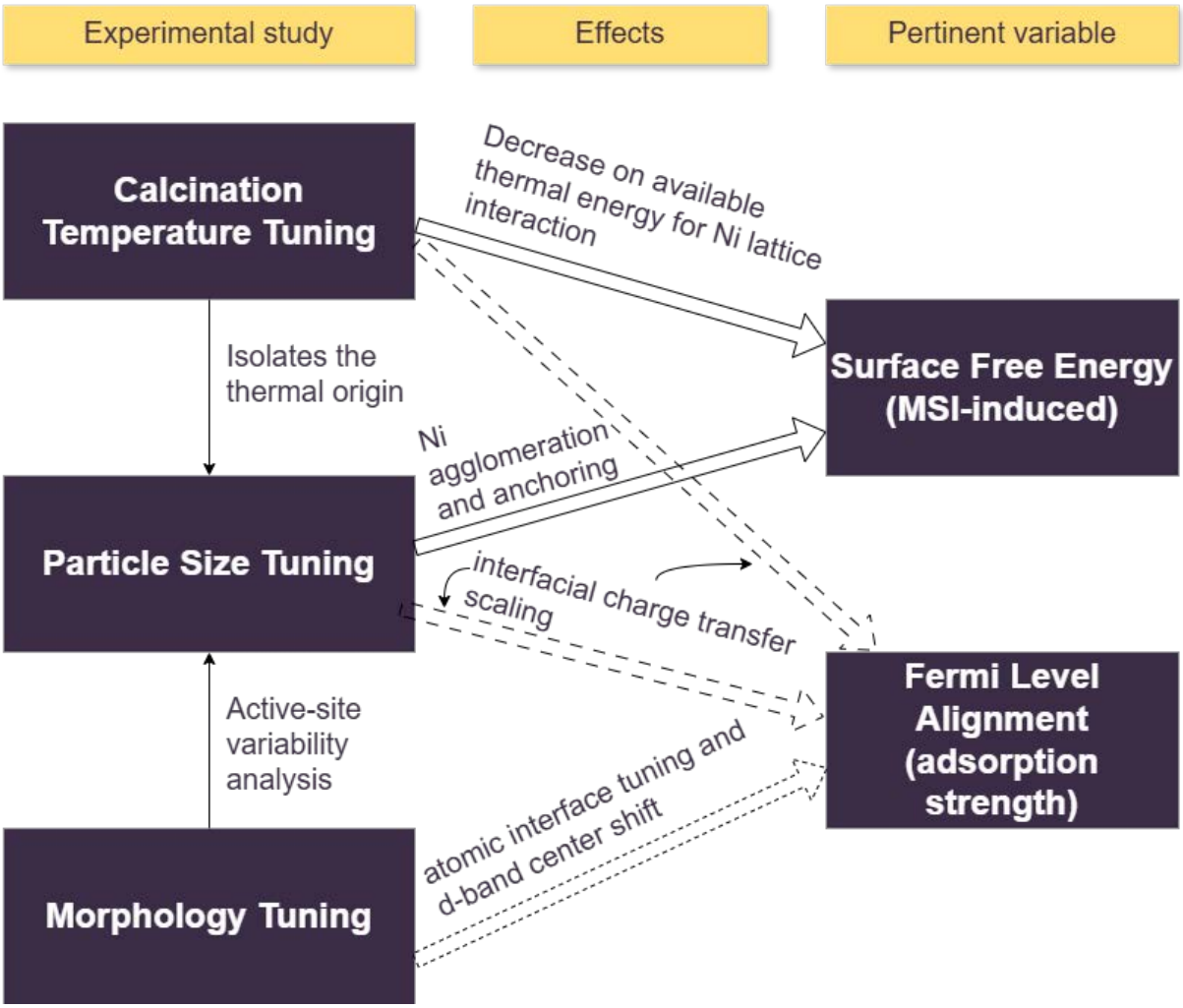

Figure 4.3: Overall surface chemistry apparent variables analysis and summary on catalyst synthesis.

5 | Performance and Use-case Analysis

How is this research relevant from an industrial point of view? This research analyzes the possibility of catalyst optimization through ceria particle size tuning. It also explores how different synthesis method and temperature would impact its performance and physical-chemical characteristics. In Figure 5.1, the results of this work has been added and can be seen in comparison to other published works. Results from this work are highlighted in bright colors and cross-hatched patterns. Using the performance of Ni/CeO2-20-O (bright green cross-hatched triangle) as a benchmark due to its best performance among the size tuned catalysts, it is competitive with other catalysts in terms of reaction rate of CO_2.

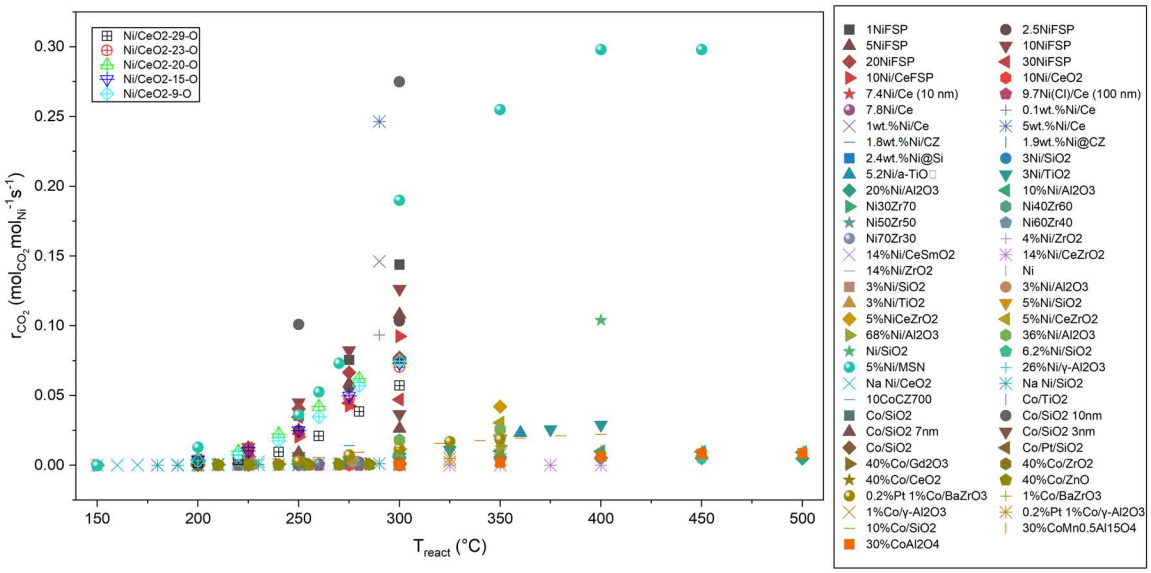

Figure 5.1: CO_2 methanation Ni and Co based metal-support variation summary compared with this work.

If we focus on low-temperature methanation, specifically 200 °C (Figure 5.2, the catalyst's competitiveness shines even further. It is understood from the work of Evtushkova et al., using a lower loading of Ni could obtain a better performance, and the tested 20 and 30 mol% loading also produced similar results to Ni/CeO2-20-O with 10-wt% (equivalent to 24.57-mol%) [2]. However, the main focus of this work is to understand the ceria particle size effect, and higher loading is deemed to be better for XRD visibility. Future works may further optimize the loading to provide an even better performing catalyst.

For a use-case of a high-turndown, electrically heated honeycomb reactor for surplus green H_2 and captured CO_2 needs a catalyst that stays kinetically active across a swinging temperature window, tolerates the thermal excursions inherent to a strongly exothermic reaction, and makes efficient use of its Ni loading. Ni/CeO_2-20-O has supporting data on all three fronts, and each compares favorably with published benchmarks for this catalyst class. Ni/CeO_2-20-O shows an apparent activation energy of 76 kJ/mol over 185-200 °C. A kinetic study of an 8.5% Ni/CeO_2 catalyst reported 103.9 kJ/mol and placed the broader Ni/CeO_2 literature range near 53.5–113 kJ/mol, with Ni/Al_2O_3-type catalysts around 75–118 kJ/mol [96]. A kaolin-supported Ni–Ce study reported 55.1–116.8 kJ/mol depending on synthesis route, citing comparable Ni/CeO_2 values of 94.9–106.0 kJ/mol [97], while a DFT/kinetic Monte Carlo study attributed unusually low apparent activation energies (roughly 41–54 kJ/mol) to a high density of interfacial oxygen vacancies [98]. 76 kJ/mol falls centrally in this spread, toward its lower half. That is operationally meaningful: a lower activation energy means the rate is less sensitive to temperature, so during turndown-driven cooling this catalyst should retain a larger fraction of its activity than higher-activation-energy Ni/CeO_2 or Ni/Al_2O_3 formulations.

Ni dispersion of 27% is high for an impregnated Ni/CeO_2 system, and is consistent with the known

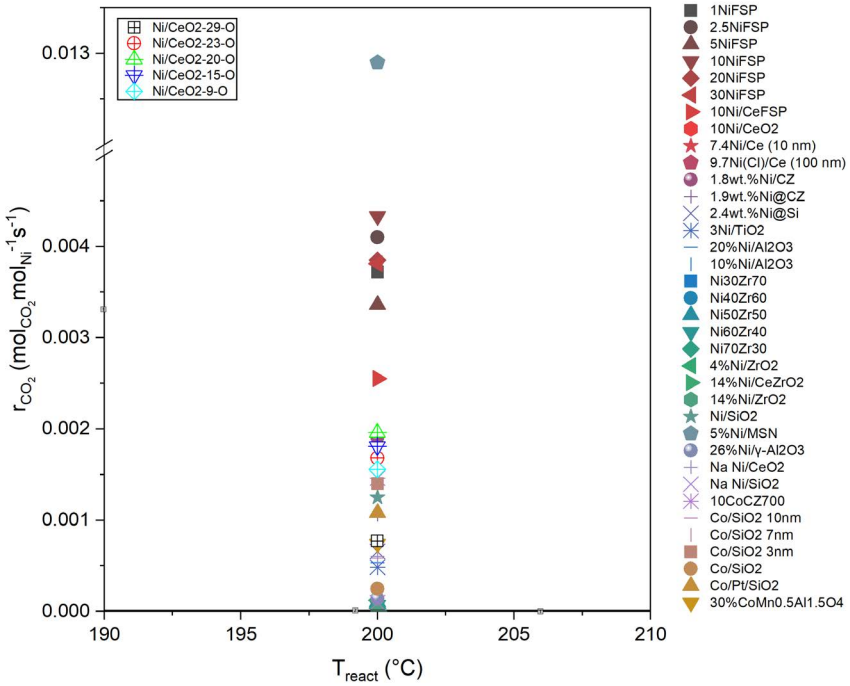

Figure 5.2: CO_2 methanation metal-support variation summary compared with this work.

mechanism behind this support's performance. Higher dispersion also means more of the Ni inventory is active surface rather than buried bulk metal, which improves cost-per-active-site when scaling washcoat loading. Honeycomb methanation is an established architecture for converting electrolytic H_2 and CO_2 into SNG with good heat management and load flexibility, already scaled from lab to MW-scale in the Store&Go project [99–101]. Reported pilots maintain a ~250 °C floor and must meet grid-injection specifications such as ≥96 vol% CH_4 [102]. The combination of lower temperature sensitivity and high site utilization maps directly onto what these reactors need.

Nickel methanation catalysts are known to deactivate via sintering and carbon deposition under prolonged exothermic operation [103]. The credible next step is to do a long stability test of 500-1000 h and adding thermal cycling, following protocols like the seven-cycle heating-cooling tests used to validate structured Ni/ceria catalysts [104]. If this catalyst were to be used for this specific use case, other tests are also required, such as wash-coat adhesion and thermal-expansion matching to the honeycomb substrate, a validated GHSV scaling law from lab conditions to reactor-volume-normalized space velocity, turndown-envelope mapping of CH_4 purity against the required specifications, and sensitivity to feed impurities (O_2, water, sulfur) from real electrolytic H_2 and captured CO_2 streams [105]. Overall, the results support advancing Ni/CeO2-20-O to extended stability and washcoat-integration testing for honeycomb methanation, broader applicability would need reactor-specific validation.

6 | Conclusion

The characterization data assembled across this thesis separates two structural pathways by which CeO_2 particle size governs CO_2 methanation performance. The first, redox-mediated pathway is reflected specifically in the spillover-linked change in support reduction state, ΔCe^{3+}, which decreases monotonically with CeO_2 particle size (+16.4%, +7.4%, and −5.2% at 9, 20, and 29 nm respectively, Table 3.6) and tracks mass-normalized CO_2 consumption rate closely at 350 °C calcination (highest at 9 nm, plateauing at 17–20 nm, collapsing at 30 nm; Section 3.2.1). This pathway governs the initial CO_2 activation step specifically, not overall product formation: the same 9 nm sample that leads in r_{CO2} is not the leading catalyst for CH_4 formation.

The second, textural pathway operates on Ni dispersion rather than support redox character. Bare-support pore diameter, and its fractional retention after Ni loading and calcination, decline sharply with decreasing CeO_2 particle size (44% pore-diameter retention at 9 nm vs. 96% at 29 nm, Table 3.2), driving a non-monotonic dispersion trend that peaks at 15–20 nm. This pathway governs methanation completion specifically, mass-normalized CH_4 formation rate correlates strongly with calculated Ni-CeO_2 interfacial site density ($R^2 = 0.982$, extrapolating through the Ni/SiO_2 reference with no interfacial sites, Section 4.1), and this correlation, not a redox metric, accounts for the CH_4-specific optimum at 20 nm. Under this framing, the redox pathway is largely a downstream electronic consequence of the textural one, via the interfacial-fraction link established in Section 4.2, rather than an independent size effect.

Across the 9–23 nm range, the reaction mechanism itself appears unchanged: FTIR identifies the same formate intermediate and CO adsorption modes on every catalyst (Section 3.1), so the redox/textural picture above reflects a shift in which step is rate-limiting rather than a change in the pathway itself. The one hint of a genuine mechanistic departure is at the largest particle size (29–30 nm), where CO selectivity rises sharply and kinetics break from this pattern (Sections 3.1 and 3.2.1), suggests, but not independently confirmed as, a different pathway outside this window.

Raising calcination temperature from 350 to 400 °C at fixed 20 nm particle size substantially improves both Ni reducibility (Ni^0/NiO: 0.24 → 0.95) and support reduction state (Ce^{3+}/Ce^{4+}: 0.395 → 0.506 as in Table 3.11). The same temperature increase also converts the Ni-size vs. support-size relationship from monotonic (at 350 °C) to non-monotonic and 20 nm-optimized (at 400 °C), coinciding with apparent activation energy shifting from a size affected activation energy (83–111 kJ/mol at 350 °C) to near-flat across particle size at 400 °C. Bare-support texture (BET area, pore volume) varies substantially across octahedral, cubic, and spherical CeO_2 even at matched Sauter mean diameter (Table 3.10). Ni/CeO_2-9-S shows an elevated Ce^{3+} fraction and Ni^{2+}–CeO_2 interaction relative to the octahedral and cubic samples (Table 3.12), even though all three vary in facet and texture simultaneously.

The optimum catalyst identified in this work, Ni/CeO_2 supported on 20 nm ceria, was found to be competitive with literature systems particularly at lower temperatures, achieving 3.93 $mmol_{CO_2}$ mol_{Ni}^{-1} h^{-1} at 200 °C and a GHSV of 300,000 ml g_{cat}^{-1} h^{-1} ($CO_2/H_2/He = 1/4/15$), 1 bar.

7 | Outlook

This thesis is able to act as a valid proof of concept, showing trends supported by existing literature and underlying surface chemistry theory. Potential synthesis and experimental errors were not quantified via error bars in this work, trend consistency was instead cross-checked qualitatively across multiple characterization techniques. To further solidify data credibility and reproducibility, re-synthesis and repeat testing is essential to be done.

In order to strongly conclude on the postulations raised, more characterizations could be done. Completing gaps in available data including XPS and CO chemisorption are vital in further grounding the arguments. In-situ measurement techniques such as isotopic switching, DRIFTS-SSITKA and quasi in-situ XPS or NAP-XPS could be done to better validate the proposed reaction mechanisms.

Overall the identified optimum ceria particle size and its industrial potential due to its performance at low temperature is interesting to further develop on, especially for the utilization of electrically heated systems for Sabatier reaction. It is interesting to analyze the system operating under different concentrations of H_2 and CO_2 which could be tailored to future application potential, i.e. biogas upgrading or ammonia production.

8 | Acknowledgements

Throughout this entire journey of the EMJM HySET Master's programme, starting with my first year in Italy and ending it with this Master's Thesis research experience at IMC in the Netherlands, I am profoundly grateful for all of my experiences. Beginning from my first year with HySET, I am thankful for all the new knowledge I received and the warmth of all the friends I have met in Italy, especially in Torino, of which I hope we will be keeping in touch. Moving to the Netherlands, I have found myself at home, working with straightforward, laid-back, yet focused people of IMC. I had so many beautiful experiences which helped me develop as a person and I hope that I can work with you all again in the future.

I would like to give special thanks to my graduation supervisor, Nikolay. I have always appreciated your candid advice and feel very thankful for your supervision and putting up with my numerous ideas. Equally, I would like to give special thanks to my thesis supervisor, Shuchi, who has always given me countless support and feedback, both mentally and in research. You have never hesitated to give me any learning opportunity of which I am interested in. I am also grateful to Samir whom despite the distance, remains supportive in my efforts and had given abundant constructive feedback. Also grateful to Ivo as a member of my graduation committee, hopefully my chemical and atomic level derivations and understanding were up to par.

At IMC, my many questions and curiosity was always accepted, and for that I am endlessly thankful to everyone there. Especially to Stefan who I pestered, fixed up a lot of my mess, and is basically a big brother supervisor to me. To Alessia, who is like my big sister who've brought warmth and taught me a lot of things. To Ariq, my energetic cousin, who helped me a lot, especially when FSP is not cooperating. To my aunt and uncles, Qingqing, Yin, and Frong, who helped me with a lot of analysis which my thesis would not have finished with otherwise. To Danya, who I bothered with TEM among other things. To Miep, Roberto, and Shogen who mentally supported me during long days in the lab. To Brahim, Tiny, and Thijs, who I have bombarded with numerous characterization requests. To everyone I have not mentioned, even including previous IMC members whose thesis I have learned from, I apologize for not mentioning your names specifically, but know that I deeply appreciate all your help and interactions that we have during my time here. Goed verhaal, lekker kort he?

My very good friend, Lana, I am very grateful to have met you, who has continuously provided me with support and love during these past two years, especially during my thesis, and hopefully many more in the future. I am also grateful to all of my HySET friends who always entertain my craziness and requests during teamworks, Nur, Vero, Aseem, Ayalneh, Rebecca, Salma, Hammad, and Abdulmumin. To my EMJM Italy friends, Fay, Alif, Vi, Nadia, Salma, I will never forget all our travels and unforgettable experiences. To my picnic friends, Miguel, Pasha, Bella, Abdan, Kak Indry, Kak Devira, Bang Naufal, and others. To Simone, Angelo, Kira, Dani, and Denise who I had fun memories with. To Alice who went all the way to Eindhoven to visit me. To the 4thfloorgang, which I feel grateful for all of the memories, Myrthe, Sara, Josh, Adam, Jochem, Joe, Danilo, and Max (in height order). To all my friends, peers, and seniors in Indonesia and all over Europe, I am eternally grateful for the endless support for me before, during and after this stage of my life.

On the closing note of this acknowledgement, I would like to thank my family for the unending support my whole life (literally). To my parents who went through a lot of surprises together with me, and my brother who is a warrior. To my cousins, uncles, aunts, and grandparents, who always hold me up.

Amo, che mi ride e piange con me. Davvero i momenti più belli della mia vita.

The graduation project (30 ECTS) was established in accordance with the rules of the TU/e Code of Scientific Conduct.

Bibliography

[1] E. J. Hensen. Basic concepts – fundamentals of catalysis (1/2). Lecture slides, 6CPT20 Catalysis: Science & Technology, 2025.

[2] A. Evtushkova. *Flame-synthesized ceria- and titania-supported Co and Ni catalysts for CO_2 hydrogenation.* PhD thesis (Research TU/e / Graduation TU/e), chemical engineering and chemistry, Eindhoven University of Technology, Eindhoven, The Netherlands, 2025. Phd Thesis 1 (Research TU/e / Graduation TU/e).

[3] Jérôme F. M. Simons, Ton J. de Heer, Rim C. J. van de Poll, Valery Muravev, Nikolay Kosinov, and Emiel J. M. Hensen. Structure sensitivity of co2 hydrogenation on ni revisited. *Journal of the American Chemical Society*, 145(37):20289–20301, 2023. PMID: 37677099.

[4] W. L. Vrijburg, J. W. A. van Helden, A. Parastaev, E. Groeneveld, E. A. Pidko, and E. J. M. Hensen. Ceria–zirconia encapsulated Ni nanoparticles for CO_2 methanation. *Catalysis Science & Technology*, 9(18):5001–5010, 2019.

[5] G. D. Weatherbee and C. H. Bartholomew. Hydrogenation of CO_2 on group VIII metals: II. kinetics and mechanism of CO_2 hydrogenation on nickel. *Journal of Catalysis*, 77(2):460–472, 1982.

[6] G. D. Weatherbee and C. H. Bartholomew. Hydrogenation of CO_2 on group VIII metals: I. specific activity of Ni/SiO_2. *Journal of Catalysis*, 68(1):67–76, 1981.

[7] J. Li, Y. Lin, X. Pan, D. Miao, D. Ding, Y. Cui, J. Dong, and X. Bao. Enhanced CO_2 methanation activity of Ni/Anatase catalyst by tuning strong metal–support interactions. *ACS Catalysis*, 9(7):6342–6348, 2019.

[8] W. L. Vrijburg, E. Moioli, W. Chen, M. Zhang, B. J. P. Terlingen, B. Zijlstra, I. A. W. Filot, A. Zuttel, E. A. Pidko, and E. J. M. Hensen. Efficient base-metal $NiMn/TiO_2$ catalyst for CO_2 methanation. *ACS Catalysis*, 9(9):7823–7839, 2019.

[9] S. Rahmani, M. Rezaei, and F. Meshkani. Preparation of highly active nickel catalysts supported on mesoporous nanocrystalline γ-Al_2O_3 for CO_2 methanation. *Journal of Industrial and Engineering Chemistry*, 20(4):1346–1352, 2014.

[10] M. Yamasaki, H. Habazaki, K. Asami, K. Izumiya, and K. Hashimoto. Effect of tetragonal ZrO_2 on the catalytic activity of Ni/ZrO_2 catalyst prepared from amorphous Ni–Zr alloys. *Catalysis Communications*, 7(1):24–28, 2006.

[11] N. Perkas, G. Amirian, Z. Zhong, J. Teo, Y. Gofer, and A. Gedanken. Methanation of carbon dioxide on Ni catalysts on mesoporous ZrO_2 doped with rare earth oxides. *Catalysis Letters*, 130(3):455–462, 2009.

[12] C. K. Vance and C. H. Bartholomew. Hydrogenation of carbon dioxide on group VIII metals: III, effects of support on activity/selectivity and adsorption properties of nickel. *Applied Catalysis*, 7(2):169–177, 1983.

[13] P. A. U. Aldana, F. Ocampo, K. Kobl, B. Louis, F. Thibault-Starzyk, M. Daturi, P. Bazin, S. Thomas, and A. C. Roger. Catalytic CO_2 valorization into CH_4 on Ni-based ceria-zirconia. reaction mechanism by operando IR spectroscopy. *Catalysis Today*, 215:201–207, 2013.

[14] D. Beierlein, D. Häussermann, M. Pfeifer, T. Schwarz, K. Schütte, Y. Traa, and E. Klemm. Is the CO_2 methanation on highly loaded $Ni\text{-}Al_2O_3$ catalysts really structure-sensitive? *Applied Catalysis B: Environmental*, 247:200–219, 2019.

[15] C. Vogt, E. Groeneveld, G. Kamsma, M. Nachtegaal, L. Lu, C. J. Kiely, P. H. Berben, F. Meirer, and B. M. Weckhuysen. Unravelling structure sensitivity in CO_2 hydrogenation over nickel. *Nature Catalysis*, 1(2):127–134, 2018.

[16] M. A. A. Aziz, A. A. Jalil, S. Triwahyono, R. R. Mukti, Y. H. Taufiq-Yap, and M. R. Sazegar. Highly active Ni-promoted mesostructured silica nanoparticles for CO_2 methanation. *Applied Catalysis B: Environmental*, 147:359–368, 2014.

[17] T. Van Herwijnen, H. Van Doesburg, and W. A. De Jong. Kinetics of the methanation of CO and CO_2 on a nickel catalyst. *Journal of Catalysis*, 28(3):391–402, 1973.

[18] T. A. Le, T. W. Kim, S. H. Lee, and E. D. Park. Effects of Na content in Na/Ni/SiO_2 and Na/Ni/CeO_2 catalysts for CO and CO_2 methanation. *Catalysis Today*, 303:159–167, 2018.

[19] A. Parastaev, V. Muravev, E. Huertas Osta, A. J. F. van Hoof, T. F. Kimpel, N. Kosinov, and E. J. M. Hensen. Boosting CO_2 hydrogenation via size-dependent metal–support interactions in cobalt/ceria-based catalysts. *Nature Catalysis*, 3(6):526–533, 2020.

[20] G. Melaet, W. T. Ralston, C.-S. Li, S. Alayoglu, K. An, N. Musselwhite, B. Kalkan, and G. A. Somorjai. Evidence of highly active cobalt oxide catalyst for the Fischer–Tropsch synthesis and CO_2 hydrogenation. *Journal of the American Chemical Society*, 136(6):2260–2263, 2014.

[21] V. Iablokov, S. K. Beaumont, S. Alayoglu, V. V. Pushkarev, C. Specht, J. Gao, A. P. Alivisatos, N. Kruse, and G. A. Somorjai. Size-controlled model Co nanoparticle catalysts for CO_2 hydrogenation: Synthesis, characterization, and catalytic reactions. *Nano Letters*, 12(6):3091–3096, 2012.

[22] S. K. Beaumont, S. Alayoglu, C. Specht, W. D. Michalak, V. V. Pushkarev, J. Guo, N. Kruse, and G. A. Somorjai. Combining in situ NEXAFS spectroscopy and CO_2 methanation kinetics to study Pt and Co nanoparticle catalysts reveals key insights into the role of platinum in promoted cobalt catalysis. *Journal of the American Chemical Society*, 136(28):9898–9901, 2014.

[23] W. Li, H. Liu, H. Jiang, J. Guo, M. Wang, M. Guo, Z. Song, J. Zhao, and X. Ma. ZrO_2 support imparts superior activity and stability of Co catalysts for CO_2 methanation. *Applied Catalysis B: Environmental*, 220:397–408, 2018.

[24] J. Díez-Ramírez, P. Sánchez, J. L. Valverde, and F. Dorado. Effect of support nature on the cobalt-catalyzed CO_2 hydrogenation. *Journal of CO_2 Utilization*, 21:562–571, 2017.

[25] H. H. Shin, L. Lu, Z. Yang, C. J. Kiely, and S. McIntosh. Cobalt catalysts decorated with platinum atoms supported on barium zirconate provide enhanced activity and selectivity for CO_2 methanation. *ACS Catalysis*, 6(5):2811–2818, 2016.

[26] G. Zhou, H. Liu, Y. Xing, S. Xu, H. Xie, and K. Xiong. CO_2 hydrogenation to methane over mesoporous Co/SiO_2 catalysts: Effect of structure. *Journal of CO_2 Utilization*, 26:221–229, 2018.

[27] T. Franken, J. Terreni, A. Borgschulte, and A. Heel. Solid solutions in reductive environment – A case study on improved CO_2 hydrogenation to methane on cobalt based catalysts derived from ternary mixed metal oxides by modified reducibility. *Journal of Catalysis*, 382:385–394, 2020.

[28] Yingzhe Shi, Wei Su, Yi Xing, Yongkang Cui, Ximiao Liu, Wentao Guo, and Zichang Che. Research progress and future prospects of chemical utilization of co2. *Chemical Engineering Journal*, 510:161579, 2025.

[29] Job J. C. Struijs, Valery Muravev, Marcel A. Verheijen, Emiel J. M. Hensen, and Nikolay Kosinov. Ceria-supported cobalt catalyst for low-temperature methanation at low partial pressures of co2. *Angewandte Chemie International Edition*, 62(5):e202214864, 2023.

[30] Nur Diyan Mohd Ridzuan, Maizatul Shahrun, Mohd Anawar, and Israf Ud-Din. Ni-based catalyst for carbon dioxide methanation: A review on performance and progress. *Catalysts*, 12:469, 04 2022.

[31] Ralph W. G. Wyckoff. *Crystal Structures*, volume 1. Interscience Publishers, New York, 2 edition, 1963.

[32] P. W. Tasker. The stability of ionic crystal surfaces. *Journal of Physics C: Solid State Physics*, 12(22):4977–4984, 1979.

[33] J. H. Scofield. Hartree-Slater subshell photoionization cross-sections at 1254 and 1487 eV. *Journal of Electron Spectroscopy and Related Phenomena*, 8(2):129–137, 1976.

[34] Calvin H. Bartholomew and Robert J. Farrauto. *Fundamentals of Industrial Catalytic Processes*. Wiley-AIChE, 2 edition, 2006.

[35] J. I. Langford and A. J. C. Wilson. Scherrer after sixty years: A survey and some new results in the determination of crystallite size. *Journal of Applied Crystallography*, 11(2):102–113, 1978.

[36] R. Van Hardeveld and F. Hartog. The statistics of surface atoms and surface sites on metal crystals. *Surface Science*, 15(2):189–230, 1969.

[37] John R. Rumble, editor. *CRC Handbook of Chemistry and Physics*. CRC Press, Boca Raton, FL, 102 edition, 2021.

[38] IPCC. Climate change 2022: Mitigation of climate change. Technical report, Intergovernmental Panel on Climate Change, 2022.

[39] P. Forster et al. The earth's energy budget, climate feedbacks, and climate sensitivity. *IPCC AR6 Working Group I*, 2021.

[40] R. Lindsey and L. Dahlman. Climate change: Global temperature. *NOAA Climate.gov*, 2021.

[41] J. Blunden and D. S. Arndt. State of the climate in 2014. *Bulletin of the American Meteorological Society*, 96(7):S1–S267, 2015.

[42] A. Kumar et al. Catalytic conversion of carbon dioxide into fuels and chemicals. *Renewable and Sustainable Energy Reviews*, 135:110190, 2021.

[43] National Center for Biotechnology Information. Carbon dioxide compound summary, 2023. PubChem.

[44] S. Patial et al. Co_2 activation and conversion: Challenges and opportunities. *Chemical Engineering Journal*, 405:126641, 2021.

[45] H. Selin and N. Eckley. Carbon capture and storage: Technology and policy. *Annual Review of Environment and Resources*, 44:479–505, 2019.

[46] A. Rodrigues et al. Carbon capture and utilization: A review. *Journal of CO_2 Utilization*, 9:1–13, 2015.

[47] P. Gabrielli et al. The role of co_2 utilization in climate mitigation. *Energy & Environmental Science*, 13:361–386, 2020.

[48] M. Aresta. *Carbon Dioxide as Chemical Feedstock*. Wiley-VCH, 2010.

[49] Andrew Litheko, Bilainu Oboirien, and Bilal Patel. Life cycle assessment of power-to-gas (ptg) technology – evaluation of system configurations of renewable hydrogen and methane production. *Sustainable Energy Technologies and Assessments*, 60:103527, 2023.

[50] STORE&GO Consortium. Innovative large-scale energy storage technologies and power-to-gas concepts after optimization. Technical report, European Union Horizon 2020, 2018. Deliverable D8.3.

[51] M.A. Vannice. The catalytic synthesis of hydrocarbons from h2co mixtures over the group viii metals: I. the specific activities and product distributions of supported metals. *Journal of Catalysis*, 37(3):449–461, 1975.

[52] Wei Wang, Haofei Shi, and Janos Szanyi. Controlling selectivities in co_2 reduction through mechanistic understanding. *Nature Communications*, 8(1):513, 2017.

[53] Fan Wang, Shibo He, Hao Chen, Bo Wang, Lirong Zheng, Meilin Wei, David G. Evans, and Xue Duan. Active site dependent reaction mechanism over ru/ceo_2 catalyst toward co_2 methanation. *Journal of the American Chemical Society*, 138(19):6298–6305, 2016.

[54] Job J. C. Struijs. Low co_2 partial pressure hydrogenation: can reducible oxides bring us there? Master's thesis, Eindhoven University of Technology, Eindhoven, The Netherlands, 2021.

[55] Tushar Sakpal and Leon Lefferts. Structure-dependent activity of ceo2 supported ru catalysts for co2 methanation. *Journal of Catalysis*, 367:171–180, 2018.

[56] Ton J. de Heer. Investigating the structure sensitivity of the co_2 hydrogenation on ni catalysts. Master's thesis, Eindhoven University of Technology, Eindhoven, The Netherlands, 2023.

[57] Sining Chen, Luke Higgins, Ilenia Giarnieri, Patricia Benito, and Andrew M. Beale. A detailed characterization study of ni/ceo2 catalysts identifies ni availability as the primary factor affecting co2 methanation performance. *Journal of Catalysis*, 439:115778, 2024.

[58] Feng Jiang, Shanshan Wang, Bing Liu, Jie Liu, Li Wang, Yang Xiao, Yuebing Xu, and Xiaohao Liu. Insights into the influence of ceo2 crystal facet on co2 hydrogenation to methanol over pd/ceo2 catalysts. *ACS Catalysis*, 10(19):11493–11509, 2020.

[59] Shuangxi Lin, Rui Tang, Xudong Liu, Longchen Gong, and Zhenhua Li. Modulating co2 methanation activity on ni/ceo2 catalysts by tuning ceria facet-induced metal-support interaction. *International Journal of Hydrogen Energy*, 51:462–475, 2024.

[60] Michalis Konsolakis and Maria Lykaki. Facet-dependent reactivity of ceria nanoparticles exemplified by ceo2-based transition metal catalysts: A critical review. *Catalysts*, 11(4), 2021.

[61] Dipesh Adhikari, Colby A. Whitcomb, Weijie Zhang, Sen Zhang, and Robert J. Davis. Revisiting the influence of ni particle size on the hydrogenation of co2 to ch4 over ni/ceo2. *Journal of Catalysis*, 438:115708, 2024.

[62] Shuangxi Lin, Zhenhua Li, and Maoshuai Li. Tailoring metal-support interactions via tuning ceo2 particle size for enhancing co2 methanation activity over ni/ceo2 catalysts. *Fuel*, 333:126369, 2023.

[63] Yannis C.A. van den Bosch. Ceria particle size effect in pd/ceo_2. Master's thesis, Eindhoven University of Technology, September 2021. Supervisors: Emiel J.M. Hensen, Nikolay A. Kosinov & Valerii Muravev.

[64] Eng Toon Saw, Usman Oemar, Ming Li Ang, Hidajat Kus, and Sibudjing Kawi. High-temperature water gas shift reaction on $ni–cu/ceo_2$ catalysts: effect of ceria nanocrystal size on carboxylate formation. *Catalysis Science & Technology*, 6:5336–5349, 2016.

[65] Valery Muravev, Giulia Spezzati, Ya-Qiong Su, Alexander Parastaev, Fu-Kuo Chiang, Alessandro Longo, Carlos Escudero, Nikolay Kosinov, and Emiel J. M. Hensen. Interface dynamics of pd–ceo2 single-atom catalysts during co oxidation. *Nature Catalysis*, 4(6):469–478, Jun 2021.

[66] Yu Gao, Valery Muravev, Yonghui Fan, Hao Zhang, Jorden Wagemakers, Alexander Parastaev, Nikolay Kosinov, and Emiel J. M. Hensen. Strong stabilization of co nanoparticles by ceo2-x clusters in inverse ceox/co catalysts for enhanced co2 methanation. *Advanced Materials*, 38(2):e10593, 2026.

[67] Mark C. Biesinger, Brad P. Payne, Leo W. M. Lau, Andrea Gerson, and Roger St. C. Smart. X-ray photoelectron spectroscopic chemical state quantification of mixed nickel metal, oxide and hydroxide systems. *Surface and Interface Analysis*, 41(4):324–332, 2009.

[68] Sergio López-Rodríguez, Arantxa Davó-Quiñonero, Esther Bailón-García, Dolores Lozano-Castelló, Ignacio J. Villar-Garcia, Virginia Perez Dieste, Jon Ander Onrubia Calvo, Juan Ramón González Velasco, and Agustín Bueno-López. Monitoring by in situ nap-xps of active sites for co2 methanation on a ni/ceo2 catalyst. *Journal of CO2 Utilization*, 60:101980, 2022.

[69] J. F. M. Simons, A. Parastaev, V. Muravev, M. A. Verheijen, N. Kosinov, and E. J. M. Hensen. Structure sensitivity of CO_2 hydrogenation on Ni revisited. *Journal of the American Chemical Society*, 145:20289–20301, 2023.

[70] Shohei Tada, Hironori Nagase, Naoya Fujiwara, and Ryuji Kikuchi. What are the best active sites for co 2 methanation over ni/ceo 2 ? *Energy Fuels*, 35, 03 2021.

[71] Thomas W. Hansen, Andrew T. DeLaRiva, Sivakumar R. Challa, and Abhaya K. Datye. Sintering of catalytic nanoparticles: Particle migration or ostwald ripening? *Accounts of Chemical Research*, 46(8):1720–1730, 2013. PMID: 23634641.

[72] Abd El-Aziz A Said, Mohamed M M Abd El-Wahab, and Mohamed Abd El-Aal. Catalytic dehydration of methanol to dimethyl ether over nanosized WO3/Al2O3 system under inert and oxidative atmosphere. *Monatsh. Chem.*, 147(9):1507–1516, September 2016.

[73] Sebastian Siol, Jennifer Mann, John Newman, Takuya Miyayama, Katsumi Watanabe, Patrik Schmutz, Claudia Cancellieri, and Lars P.H. Jeurgens. Concepts for chemical state analysis at constant probing depth by lab-based xps/haxpes combining soft and hard x-ray sources. *Surface and Interface Analysis*, 52(12):802–810, 2020.

[74] Xiangwen Liu, Kebin Zhou, Lei Wang, Baoyi Wang, and Yadong Li. Oxygen vacancy clusters promoting reducibility and activity of ceria nanorods. *Journal of the American Chemical Society*, 131(9):3140–3141, 2009. PMID: 19215075.

[75] Kexin Ma, Weiqi Liao, Wen Shi, Fangkai Xu, Yan Zhou, Cen Tang, Jiqing Lu, Wenjie Shen, and Zhenhua Zhang. Ceria-supported pd catalysts with different size regimes ranging from single atoms to nanoparticles for the oxidation of co. *Journal of Catalysis*, 407:104–114, 2022.

[76] Wan Yang, Kaizhu Chang, Meng Yang, Xueshuang Yan, Shiju Yang, Yongjun Liu, Guowei Wang, Futing Xia, Huimin Wang, and Qiulin Zhang. Facilitating co2 methanation over oxygen vacancy-rich ni/ceo2: Insights into the synergistic effect between oxygen vacancy and metal-support interaction. *Chemical Engineering Journal*, 499:156493, 2024.

[77] Ning Rui, Xiaoshan Zhang, Feng Zhang, Zongyuan Liu, Xinxiang Cao, Zhenhua Xie, Rui Zou, Sanjaya D. Senanayake, Yanhui Yang, José A. Rodriguez, and Chang-Jun Liu. Highly active ni/ceo2 catalyst for co2 methanation: Preparation and characterization. *Applied Catalysis B: Environmental*, 282:119581, 2021.

[78] Pablo G. Lustemberg, Zhongtian Mao, Agustín Salcedo, Beatriz Irigoyen, M. Verónica Ganduglia-Pirovano, and Charles T. Campbell. Nature of the active sites on ni/ceo2 catalysts for methane conversions. *ACS Catalysis*, 11(16):10604–10613, 2021.

[79] Baitao Li, Kenji Maruyama, Mohammad Nurunnabi, Kimio Kunimori, and Keiichi Tomishige. Effect of ni loading on catalyst bed temperature in oxidative steam reforming of methane over α-al2o3-supported ni catalysts. *Industrial & Engineering Chemistry Research*, 44(3):485–494, 2005.

[80] Yingrui Zhao, Plaifa Hongmanorom, Feilong Yang, Sandra Casale, Capucine Sassoye, Ales Styskalik, and Damien P. Debecker. Carbon nitride boosts the co2 methanation activity of ni/ceo2. *Journal of Environmental Chemical Engineering*, 13(6):119153, 2025.

[81] A. Cárdenas-Arenas, A. Quindimil, A. Davó-Quiñonero, E. Bailón-García, D. Lozano-Castelló, U. De-La-Torre, B. Pereda-Ayo, J. A. González-Marcos, J. R. González-Velasco, and A. Bueno-López. Isotopic and in situ DRIFTS study of the CO2 methanation mechanism using Ni/CeO2 and Ni/Al2O3 catalysts. *Applied Catalysis B: Environmental*, 265:118538, 2020.

[82] In situ investigation of the CO2 methanation on carbon/ceria-supported Ni catalysts using modulation-excitation DRIFTS. *Applied Catalysis B: Environmental*, 2022. ScienceDirect record S0926337322003174; verify full author list at source.

[83] Ziwen Hao, Jindong Shen, Shuangxi Lin, Xiaoyu Han, Xiao Chang, Jie Liu, Maoshuai Li, and Xinbin Ma. Decoupling the effect of ni particle size and surface oxygen deficiencies in CO2 methanation over ceria supported ni. *Appl. Catal. B*, 286(119922):119922, June 2021.

[84] Yu Guo, Sheng Mei, Kun Yuan, De-Jiu Wang, Hai-Chao Liu, Chun-Hua Yan, and Ya-Wen Zhang. Low-temperature co2 methanation over ceo2-supported ru single atoms, nanoclusters, and nanoparticles competitively tuned by strong metal–support interactions and h-spillover effect. *ACS Catalysis*, 8(7):6203–6215, 2018.

[85] Yao Zhang, Huaizhong Xiang, Boji Wang, Zhipeng Qie, Keran Jiao, Xuzhao Liu, Xiaolei Fan, and Shanshan Xu. A comparative study of the effect of metal–support interaction on catalytic co2 methanation over ni/cexzr1xo2 catalysts under thermal and plasma conditions. *Catal. Sci. Technol.*, 16:560–571, 2026.

[86] A. L. Patterson. The Scherrer formula for X-Ray particle size determination. *Physical Review*, 56(10):978–982, 1939.

[87] Anastasiia S. Kholtobina, Axel Forslund, Andrei V. Ruban, Börje Johansson, and Natalia V. Skorodumova. Temperature dependence of (111) and (110) ceria surface energy. *Phys. Rev. B*, 107:035407, Jan 2023.

[88] Agapi Orfanoudaki, Maria Lykaki, Angelos K Bonis, Shailza Saini, George Dury, Greg A Mutch, Evangelos I Papaioannou, Kalliopi Kousi, and Michalis Konsolakis. Facet-dependent metal–support interactions in cobalt–ceria binary oxides: linking ceria morphology (rods *vs.* cubes) to redox behaviour and CO oxidation. *Catal. Sci. Technol.*, 16(8):2716–2728, 2026.

[89] Hao Lou, Inam Ullah, Yunhong Luo, Syed Musab Ahmed, Zeeshan Abbasi, Hui Zhang, Jie Ren, Wenlong Wu, and Zhandong Wang. Unveiling the origin of structure sensitivity for CO $_2$ methanation over Ni/CeO $_2$ catalysts. *ACS Catal.*, 16(6):6020–6031, March 2026.

[90] Gonzalo Aguila, Rafael Calle, Sichem Guerrero, Patricio Baeza, and Paulo Araya. Improvement of thermal stability of highly active species on SiO2 supported copper-ceria catalysts. *RSC Adv.*, 11(53):33271–33275, October 2021.

[91] B. Hammer and J. K. Nørskov. Theoretical surface science and catalysis–calculations and concepts. *Advances in Catalysis*, 45:71–129, 2000.

[92] J. K. Nørskov, F. Abild-Pedersen, F. Studt, and T. Bligaard. Density functional theory in surface chemistry and catalysis. *Proceedings of the National Academy of Sciences*, 108(3):937–943, 2011.

[93] Zhongtian Mao, Pablo G. Lustemberg, John R. Rumptz, M. Verónica Ganduglia-Pirovano, and Charles T. Campbell. Ni nanoparticles on ceo2(111): Energetics, electron transfer, and structure by ni adsorption calorimetry, spectroscopies, and density functional theory. *ACS Catalysis*, 10(9):5101–5114, 2020.

[94] J. A. van Bokhoven, A. M. J. van der Eerden, and G. Sankar. d electron density and reactivity of the d band as a function of particle size in supported gold catalysts. *Journal of Physical Chemistry C*, 111:9245–9249, 2007.

[95] W. Q. Li, S. Goverapet Srinivasan, D. R. Salahub, and T. Heine. Ni on the ceo2(110) and (100) surfaces: adsorption vs. substitution effects on the electronic and geometric structures and oxygen vacancies. *Physical Chemistry Chemical Physics*, 18(16):11139–11149, 2016.

[96] Jon A Onrubia-Calvo, Adrián Quindimil, Arantxa Davó-Quiñonero, Alejandro Bermejo-López, Esther Bailón-García, Beñat Pereda-Ayo, Dolores Lozano-Castelló, José A González-Marcos, Agustín Bueno-López, and Juan R González-Velasco. Kinetics, model discrimination, and parameters estimation of CO_2 methanation on highly active Ni/CeO_2 catalyst. *Ind. Eng. Chem. Res.*, 61(29):10419–10435, July 2022.

[97] Kritchakorn Aimdate, Atthapon Srifa, Wanida Koo-Amornpattana, Chularat Sakdaronnarong, Wantana Klysubun, Sirapassorn Kiatphuengporn, Suttichai Assabumrungrat, Suwimol Wongsakulphasatch, Watchareeya Kaveevivitchai, Masao Sudoh, Ryo Watanabe, Choji Fukuhara, and Sakhon Ratchahat. Natural kaolin-based ni catalysts for CO2 methanation: On the effect of ce enhancement and microwave-assisted hydrothermal synthesis. *ACS Omega*, 6(21):13779–13794, June 2021.

[98] Pablo Lozano-Reis, Pablo Gamallo, Ramón Sayós, and Francesc Illas. Comprehensive density functional and kinetic monte carlo study of CO2 hydrogenation on a well-defined Ni/CeO2 model catalyst: Role of Eley-Rideal reactions. *ACS Catal.*, 14(4):2284–2299, February 2024.

[99] Mathias Held, Dominik Schollenberger, Simon Sauerschell, Siegfried Bajohr, and Thomas Kolb. Power-to-gas: CO 2 methanation concepts for SNG production at the Engler-Bunte-Institut. *Chem. Ing. Tech.*, 92(5):595–602, May 2020.

[100] Dominik Schollenberger, Siegfried Bajohr, Manuel Gruber, Rainer Reimert, and Thomas Kolb. Scale-up of innovative honeycomb reactors for power-to-gas applications - the project store&go. *Chem. Ing. Tech.*, 90(5):696–702, May 2018.

[101] Karlsruhe Institute of Technology, Energy Lab. Power-to-gas – the methanation plants, 2024.

[102] Philipp Biegger, Florian Kirchbacher, Ana Roza Medved, Martin Miltner, Markus Lehner, and Michael Harasek. Development of honeycomb methanation catalyst and its application in power to gas systems. *Energies*, 11(7):1679, June 2018.

[103] Peter Strucks, Luisa Failing, and Stefan Kaluza. A short review on ni-catalyzed methanation of CO 2 : Reaction mechanism, catalyst deactivation, dynamic operation. *Chem. Ing. Tech.*, 93(10):1526–1536, October 2021.

[104] Xin Tang, Chuqiao Song, Haibo Li, Wenyu Liu, Xinyu Hu, Qiaoli Chen, Hanfeng Lu, Siyu Yao, Xiao-Nian Li, and Lili Lin. Thermally stable ni foam-supported inverse CeAlOx/Ni ensemble as an active structured catalyst for CO2 hydrogenation to methane. *Nat. Commun.*, 15(1):3115, April 2024.

[105] Jie Ren, Han Lei, Chalachew Mebrahtu, Feng Zeng, Xusheng Zheng, Gang Pei, Wenhua Zhang, and Zhandong Wang. Ni-based hydrotalcite-derived catalysts for enhanced CO2 methanation: Thermal tuning of the metal-support interaction. *Appl. Catal. B*, 340(123245):123245, January 2024.

[106] E. Marconi, S. Tuti, and I. Luisetto. Structure-sensitivity of CO_2 methanation over nanostructured Ni supported on CeO_2 nanorods. *Catalysts*, 9:375, 2019.

A | State of the Art

Table A.1: Catalytic performance in CO_2 of Co and Ni based catalysts: State of the Art.

Catalyst	H_2:CO_2 (–)	P_{tot} (bar)	x_{CO_2} (%)	T_{react} (°C)	Activity ($mol_{CO_2}\ mol^{-1}_{metal}\ s^{-1}$)	Ref.
Ni/CeO_2-9-O	4	1	5	200	3.12×10^{-3}	This work
				220	7.57×10^{-3}	
				240	1.74×10^{-2}	
				260	3.43×10^{-2}	
				280	5.63×10^{-2}	
				300	7.35×10^{-2}	
Ni/CeO_2-15-O	4	1	5	200	3.63×10^{-3}	This work
				225	1.01×10^{-2}	
				250	2.47×10^{-2}	
				275	4.9×10^{-2}	
				300	7.22×10^{-2}	
Ni/CeO_2-20-O	4	1	5	200	3.93×10^{-3}	This work
				220	9.77×10^{-3}	
				240	2.21×10^{-2}	
				260	4.16×10^{-2}	
				280	6.13×10^{-2}	
				300	7.37×10^{-2}	
Ni/CeO_2-23-O	4	1	5	200	3.37×10^{-3}	This work
				225	9.4×10^{-3}	
				250	2.37×10^{-2}	
				275	4.69×10^{-2}	
				300	6.95×10^{-2}	
Ni/CeO_2-29-O	4	1	5	200	1.53×10^{-3}	This work
				220	3.85×10^{-3}	
				240	9.5×10^{-3}	
				260	2.07×10^{-2}	
				280	3.81×10^{-2}	
				300	5.64×10^{-2}	
1NiFSP	4	1	15	200	3.72×10^{-3}	[2]
				225	1.042×10^{-2}	
				250	3.562×10^{-2}	
				275	7.55×10^{-2}	
				300	1.438×10^{-1}	
2.5NiFSP	4	1	15	200	4.1×10^{-3}	[2]
				225	9.45×10^{-3}	
				250	2.48×10^{-2}	
				275	5.61×10^{-2}	
				300	1.034×10^{-1}	
5NiFSP	4	1	15	200	3.36×10^{-3}	[2]
				225	9.18×10^{-3}	
				250	2.48×10^{-2}	
				275	5.848×10^{-2}	
				300	1.08×10^{-1}	
10NiFSP	4	1	15	200	4.33×10^{-3}	[2]
				225	1.302×10^{-2}	

Continued on next page

Table A.1 – *continued*

Catalyst	H_2:CO_2 (–)	P_{tot} (bar)	x_{CO_2} (%)	T_{react} (°C)	Activity ($mol_{CO_2}\ mol_{metal}^{-1}\ s^{-1}$)	Ref.
				250	4.5×10^{-2}	
				275	8.238×10^{-2}	
				300	1.263×10^{-1}	
20NiFSP	4	1	15	200	3.85×10^{-3}	[2]
				225	1.278×10^{-2}	
				250	4.042×10^{-2}	
				275	6.646×10^{-2}	
				300	7.7×10^{-2}	
30NiFSP	4	1	15	200	3.81×10^{-3}	[2]
				225	1.233×10^{-2}	
				250	3.453×10^{-2}	
				275	4.454×10^{-2}	
				300	4.71×10^{-2}	
10Ni/CeFSP	4	1	15	200	2.55×10^{-3}	[2]
				225	6.126×10^{-3}	
				250	2.038×10^{-2}	
				275	4.271×10^{-2}	
				300	9.246×10^{-2}	
10Ni/CeO_2	4	1	15	200	3×10^{-6}	[2]
				225	9×10^{-6}	
				250	3×10^{-5}	
				275	5.8×10^{-5}	
				300	1.04×10^{-4}	
7.4Ni/Ce (10 nm)	4	1	6.5	200	3×10^{-5}	[3]
				220	8.3×10^{-5}	
				260	2.08×10^{-4}	
				280	2.11×10^{-4}	
				300	2.11×10^{-4}	
9.7Ni(Cl)/Ce (100 nm)	4	1	6.5	200	0	[3]
				220	0	
				260	2×10^{-6}	
				280	4×10^{-6}	
				300	6×10^{-6}	
7.8Ni/Ce	4	1	—	260	9.38×10^{-4}	[3]
				280	2.204×10^{-3}	
				300	2.826×10^{-3}	
0.1wt.%Ni/Ce	4	1	13.3	290	9.333×10^{-2}	[106]
1wt.%Ni/Ce	4	1	13.3	290	1.461×10^{-1}	[106]
5wt.%Ni/Ce	4	1	13.3	290	2.464×10^{-1}	[106]
1.8wt.%Ni/CZ	4	1	3	200	1.907×10^{-3}	[4]
				225	3.362×10^{-3}	
				250	6.914×10^{-3}	
				275	1.413×10^{-2}	
				300	2.377×10^{-2}	
1.9wt.%Ni@CZ	4	1	3	200	1.062×10^{-3}	[4]
				225	1.49×10^{-3}	
				250	2.868×10^{-3}	
				275	6.902×10^{-3}	
				300	1.253×10^{-2}	

Continued on next page

Table A.1 – *continued*

Catalyst	H_2:CO_2 (–)	P_{tot} (bar)	x_{CO_2} (%)	T_{react} (°C)	Activity ($mol_{CO_2}\ mol_{metal}^{-1}\ s^{-1}$)	Ref.
2.4wt.%Ni@Si	4	1	3	200	6.55×10^{-4}	[4]
				225	6.71×10^{-4}	
				250	7.1×10^{-4}	
				275	2.44×10^{-3}	
				300	5.126×10^{-3}	
$3Ni/SiO_2$	4	1	2.76	252	4.62×10^{-4}	[5]
				252	5.1×10^{-4}	
				252	5.58×10^{-4}	
				252	6.08×10^{-4}	
				252	6.57×10^{-4}	
				252	6.9×10^{-4}	
				252	7.04×10^{-4}	
				252	7.4×10^{-4}	
				227	4.74×10^{-4}	
				252	1.06×10^{-3}	
				277	2.79×10^{-3}	
$5.2Ni/a\text{-}TiO_2$	4	1	19	360	2.32×10^{-2}	[7]
$3Ni/TiO_2$	4	1	5	200	4.83×10^{-4}	[8]
				225	9.66×10^{-4}	
				250	1.81×10^{-3}	
				275	3.38×10^{-3}	
				300	6.04×10^{-3}	
				325	1.1×10^{-2}	
				350	1.86×10^{-2}	
				375	2.57×10^{-2}	
				400	2.9×10^{-2}	
$20\%Ni/Al_2O_3$	3.5	1	22.2	200	5.33×10^{-4}	[9]
				250	3.08×10^{-3}	
				300	5.42×10^{-3}	
				350	5.66×10^{-3}	
				400	5.28×10^{-3}	
				450	5.08×10^{-3}	
				500	4.82×10^{-3}	
$10\%Ni/Al_2O_3$	3.5	1	22.2	200	2.32×10^{-4}	[9]
				250	9.27×10^{-4}	
				300	6.4×10^{-3}	
				350	1.02×10^{-2}	
				400	10^{-2}	
				450	9.64×10^{-3}	
				500	9.36×10^{-3}	
Ni30Zr70	4	1	20	150	4.85×10^{-6}	[10]
				200	4.5×10^{-5}	
Ni40Zr60	4	1	20	150	2×10^{-5}	[10]
				200	7.06×10^{-5}	
Ni50Zr50	4	1	20	150	1.62×10^{-5}	[10]
				200	1.02×10^{-4}	
Ni60Zr40	4	1	20	150	8.03×10^{-6}	[10]
				200	7.18×10^{-5}	
Ni70Zr30	4	1	20	150	8.14×10^{-6}	[10]

Continued on next page

Table A.1 – *continued*

Catalyst	H_2:CO_2 (–)	P_{tot} (bar)	x_{CO_2} (%)	T_{react} (°C)	Activity ($mol_{CO_2}\ mol_{metal}^{-1}\ s^{-1}$)	Ref.
				200	3.46×10^{-5}	
$4\%Ni/ZrO_2$	4	1	20	150	2.64×10^{-5}	[10]
				200	1.23×10^{-4}	
$14\%Ni/CeZrO_2$	4	1	20	200	1.02×10^{-6}	[11]
				250	8.36×10^{-6}	
				300	1.47×10^{-5}	
				325	1.5×10^{-5}	
				350	1.71×10^{-5}	
				375	1.77×10^{-5}	
				400	1.75×10^{-5}	
$14\%Ni/CeSmO_2$	4	1	20	150	5.82×10^{-8}	[11]
				200	1.16×10^{-6}	
				250	8.68×10^{-6}	
				300	1.47×10^{-5}	
				325	1.55×10^{-5}	
				350	1.61×10^{-5}	
				375	1.63×10^{-5}	
				400	1.7×10^{-5}	
$14\%Ni/ZrO_2$	4	1	20	200	7.61×10^{-7}	[11]
				250	9.21×10^{-6}	
				300	1.47×10^{-5}	
				325	1.74×10^{-5}	
				350	1.92×10^{-5}	
				375	2.01×10^{-5}	
				400	1.99×10^{-5}	
Ni	4	1	3	227	1.64×10^{-6}	[12]
				252	5.03×10^{-6}	
				277	1.31×10^{-5}	
$3\%Ni/SiO_2$	4	1	3	227	5.59×10^{-4}	[12]
				252	1.4×10^{-3}	
				277	3.15×10^{-3}	
$3\%Ni/Al_2O_3$	4	1	3	227	5.91×10^{-4}	[12]
				252	1.29×10^{-3}	
				277	2.54×10^{-3}	
$3\%Ni/TiO_2$	4	1	3	227	5.73×10^{-4}	[12]
				252	1.44×10^{-3}	
				277	3.58×10^{-3}	
$5\%Ni/SiO_2$	4	1	16.4	350	1.94×10^{-2}	[13]
$5\%NiCeZrO_4$	4	1	16.4	350	4.2×10^{-2}	[13]
$5\%Ni/CeZrO_4$	4	1	16.4	350	3.06×10^{-2}	[13]
$68\%Ni/Al_2O_3$	4	1	19	250	3.05×10^{-3}	[14]
				300	1.17×10^{-2}	
				350	1.38×10^{-2}	
$36\%Ni/Al_2O_3$	4	1	19	250	4.11×10^{-3}	[14]
				300	1.82×10^{-2}	
				350	2.57×10^{-2}	
Ni/SiO_2	4	5	10	200	1.25×10^{-3}	[15]
				300	8.73×10^{-3}	

Continued on next page

Table A.1 – *continued*

Catalyst	H_2:CO_2 (–)	P_{tot} (bar)	x_{CO_2} (%)	T_{react} (°C)	Activity ($mol_{CO_2}\ mol_{metal}^{-1}\ s^{-1}$)	Ref.
				400	1.04×10^{-1}	
				400	1.5×10^{-2}	
6.2%Ni/SiO_2	4	1	16.7	450	5.29×10^{-3}	[6]
5%Ni/MSN	4	1	20	150	0	[16]
				200	1.29×10^{-2}	
				250	3.61×10^{-2}	
				260	5.25×10^{-2}	
				270	7.31×10^{-2}	
				300	1.9×10^{-1}	
				350	2.55×10^{-1}	
				400	2.98×10^{-1}	
				450	2.98×10^{-1}	
26%Ni/γ-Al_2O_3	—	1	—	200	1.04×10^{-4}	[17]
				200	1.16×10^{-4}	
				200	1.23×10^{-4}	
				200	1.19×10^{-4}	
				200	1.24×10^{-4}	
				200	1.37×10^{-4}	
				200	1.4×10^{-4}	
				230	4.51×10^{-4}	
				230	5.17×10^{-4}	
				230	5.59×10^{-4}	
				230	6.35×10^{-4}	
				230	6.86×10^{-4}	
				230	5.99×10^{-4}	
Na Ni/SiO_2	1	1	1	180	2.78×10^{-5}	[18]
				190	5.56×10^{-5}	
				200	9.45×10^{-5}	
				210	1.56×10^{-4}	
				220	2.45×10^{-4}	
				230	3.89×10^{-4}	
				240	5.73×10^{-4}	
				250	7.73×10^{-4}	
				260	9.34×10^{-4}	
				270	1.02×10^{-3}	
				280	1.13×10^{-3}	
				290	1.2×10^{-3}	
				300	1.27×10^{-3}	
Na Ni/CeO_2	1	1	1	160	7×10^{-5}	[18]
				170	1.4×10^{-4}	
				180	2.24×10^{-4}	
				190	4.06×10^{-4}	
				200	6.02×10^{-4}	
				210	1.04×10^{-3}	
				220	1.68×10^{-3}	
				230	2.49×10^{-3}	
				250	3.18×10^{-3}	
				300	3.36×10^{-3}	
10CoCZ700	4	1	5	200	1.46×10^{-3}	[19]
				225	3.35×10^{-3}	
				250	6.22×10^{-3}	

Continued on next page

Table A.1 – *continued*

Catalyst	H_2:CO_2 (–)	P_{tot} (bar)	x_{CO_2} (%)	T_{react} (°C)	Activity ($mol_{CO_2}\ mol_{metal}^{-1}\ s^{-1}$)	Ref.
				275	9.19×10^{-3}	
				300	1.13×10^{-2}	
				325	1.28×10^{-2}	
				350	1.37×10^{-2}	
Co/TiO_2	4	5	25	250	3.22×10^{-3}	[20]
Co/SiO_2	4	5	25	250	1.37×10^{-3}	[20]
Co/SiO_2 10nm	4	6	22.2	200	5.86×10^{-4}	[21]
				250	1.01×10^{-1}	
				300	2.75×10^{-1}	
Co/SiO_2 7nm	4	6	22.2	200	1.54×10^{-3}	[21]
				250	8.99×10^{-3}	
				300	2.63×10^{-2}	
Co/SiO_2 3nm	4	6	22.2	200	1.4×10^{-3}	[21]
				250	6.48×10^{-3}	
				300	3.66×10^{-2}	
Co/SiO_2	4	1	25	200	8.46×10^{-5}	[22]
				200	2.49×10^{-4}	
$Co/Pt/SiO_2$	4	1	25	200	4.53×10^{-4}	[22]
				200	1.08×10^{-3}	
$10\%Co/ZrO_2$	4	30	20	400	1.2×10^{-2}	[23]
$10\%Co/Al_2O_3$	4	30	20	400	1.62×10^{-2}	[23]
$40\%Co/Gd_2O_3$	4	1	10	210	4.91×10^{-4}	[24]
				225	6.31×10^{-4}	
				240	7.58×10^{-4}	
				255	8.45×10^{-4}	
				270	9×10^{-4}	
				285	9.12×10^{-4}	
				300	9.2×10^{-4}	
$40\%Co/ZrO_2$	4	1	10	210	3.42×10^{-4}	[24]
				225	4.76×10^{-4}	
				240	5.38×10^{-4}	
				255	5.4×10^{-4}	
				270	5.55×10^{-4}	
				285	5.99×10^{-4}	
				300	7.02×10^{-4}	
$40\%Co/CeO_2$	4	1	10	210	3.06×10^{-4}	[24]
				225	4.55×10^{-4}	
				240	7.04×10^{-4}	
				255	9.01×10^{-4}	
				270	1.06×10^{-3}	
				285	1.14×10^{-3}	
				300	1.19×10^{-3}	
40%Co/ZnO	4	1	10	210	6.15×10^{-5}	[24]
				225	1.14×10^{-4}	
				240	1.78×10^{-4}	
				255	2.47×10^{-4}	
				270	3.42×10^{-4}	
				285	5.75×10^{-4}	

Continued on next page

Table A.1 – *continued*

Catalyst	H_2:CO_2 (–)	P_{tot} (bar)	x_{CO_2} (%)	T_{react} (°C)	Activity ($mol_{CO_2}\ mol_{metal}^{-1}\ s^{-1}$)	Ref.
				300	7.37×10^{-4}	
1%Co/γ-Al_2O_3	4	1	3	300	9.07×10^{-4}	[25]
				325	2.4×10^{-3}	
				350	4.05×10^{-3}	
0.2%Pt 1%Co/γ-Al_2O_3	4	1	3	300	2.02×10^{-3}	[25]
				325	4.97×10^{-3}	
				350	7.9×10^{-3}	
1%Co/$BaZrO_3$	4	1	3	275	2.52×10^{-3}	[25]
				300	6.01×10^{-3}	
				325	1.05×10^{-2}	
				350	1.37×10^{-2}	
0.2%Pt 1%Co/$BaZrO_3$	4	1	3	250	3.06×10^{-3}	[25]
				275	7.33×10^{-3}	
				300	1.18×10^{-2}	
				325	1.69×10^{-2}	
				350	1.85×10^{-2}	
10%Co/SiO_2	4	1	10	240	3.11×10^{-3}	[26]
				260	5.6×10^{-3}	
				280	9.35×10^{-3}	
				300	1.27×10^{-2}	
				320	1.57×10^{-2}	
				340	1.78×10^{-2}	
				360	1.94×10^{-2}	
				380	2.11×10^{-2}	
				400	2.21×10^{-2}	
30%$CoMn_{05}Al_{15}O_4$	4	1	20	200	7.44×10^{-4}	[27]
				250	4.56×10^{-3}	
				300	9.73×10^{-3}	
				350	1.05×10^{-2}	
				400	1.07×10^{-2}	
				450	1.06×10^{-2}	
				500	1.03×10^{-2}	
30%$CoAl_2O_4$	4	1	20	300	2.54×10^{-4}	[27]
				350	1.78×10^{-3}	
				400	6.22×10^{-3}	
				450	8.28×10^{-3}	
				500	8.51×10^{-3}	

B | Characterizations

B.1 | TEM

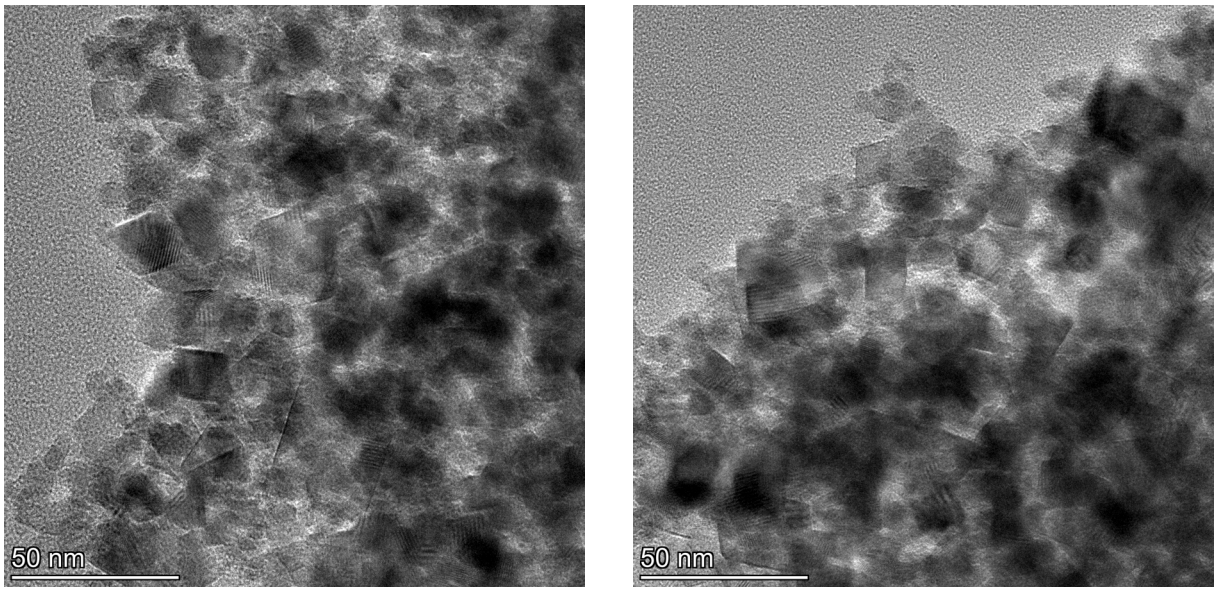

(a) TEM image 1 **(b)** TEM image 2

Figure B.1: TEM images of Ni/CeO_2-20-O.

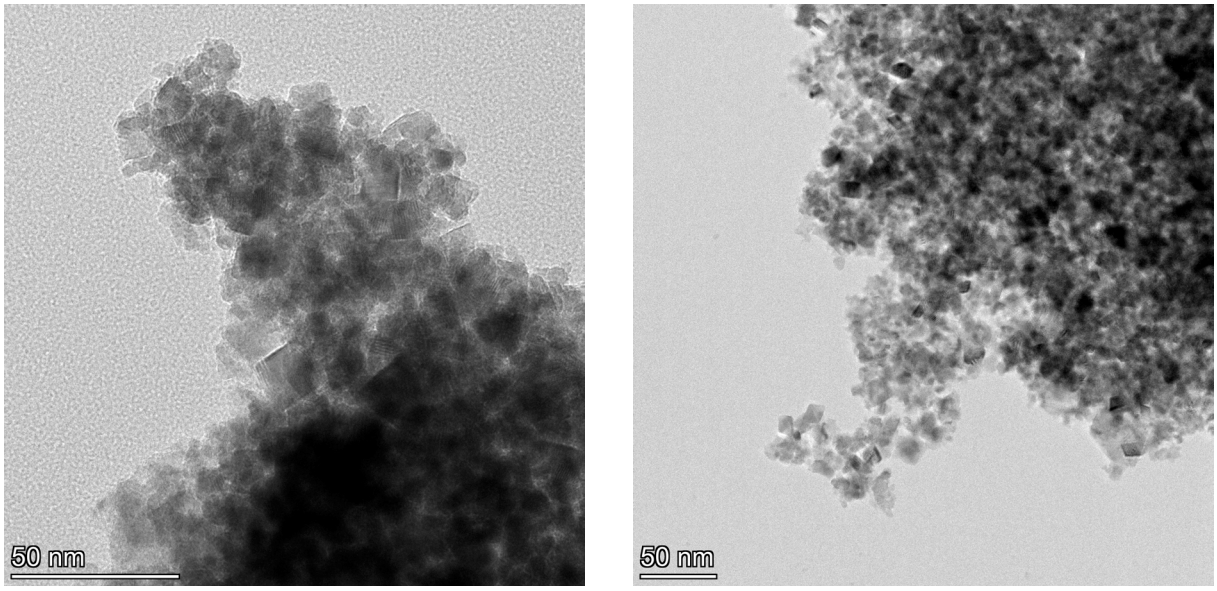

(a) TEM image 1 **(b)** TEM image 2

Figure B.2: TEM images of Ni/CeO_2-9-O.

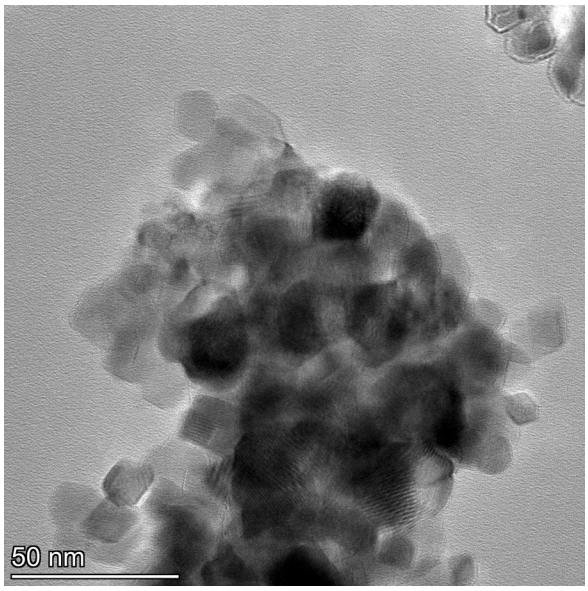

(a) TEM image 1

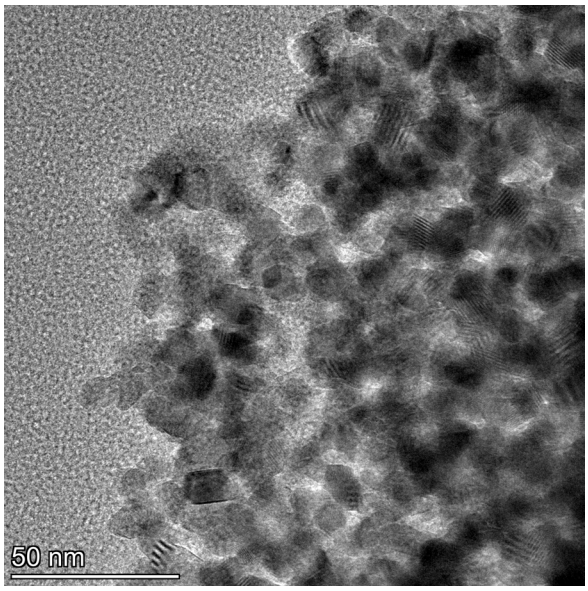

(b) TEM image 2

Figure B.3: TEM images of Ni/CeO_2-15-C.

B.2 | STEM

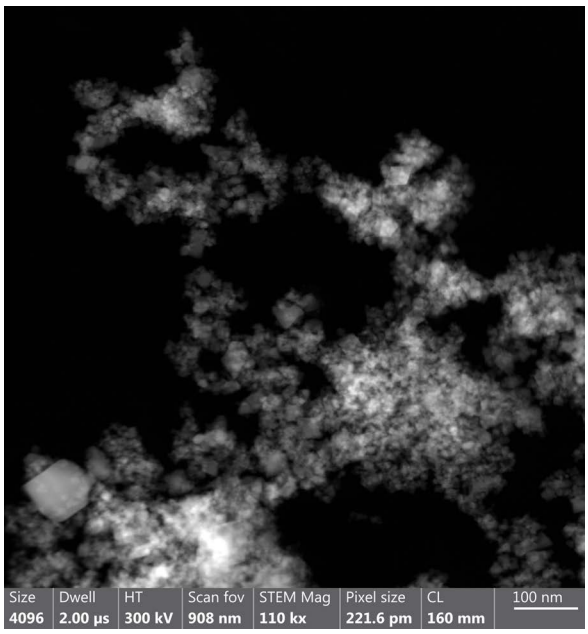

(a) STEM HAADF image

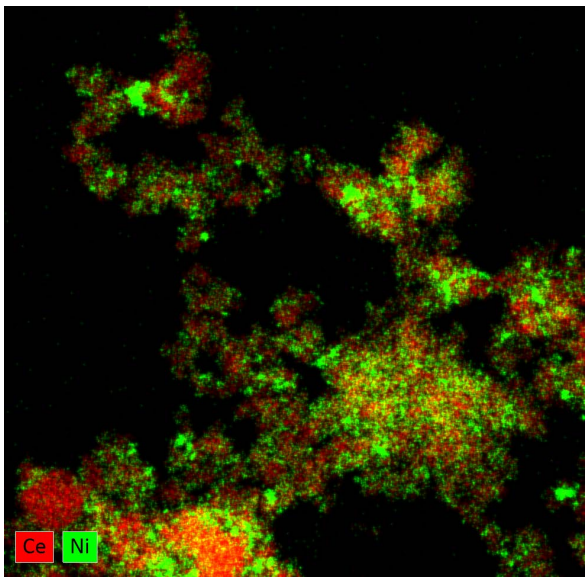

(b) EDX image

Figure B.4: STEM images of Ni/CeO_2-20-O.

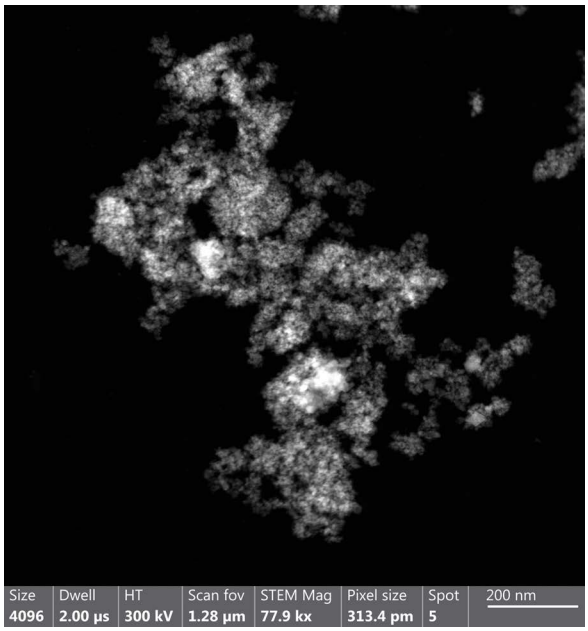

(a) STEM HAADF image

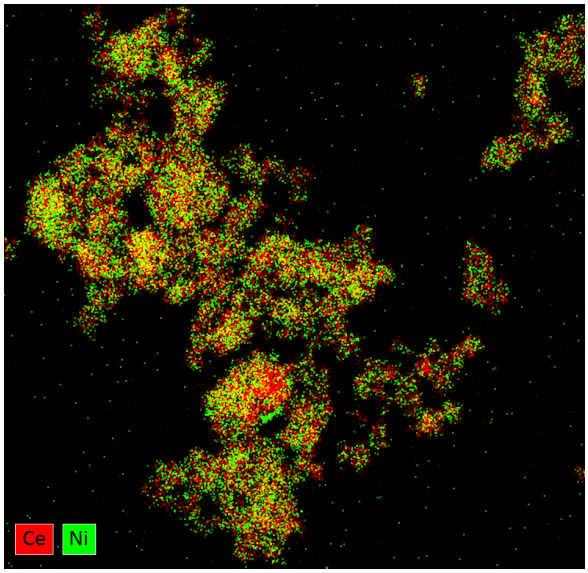

(b) EDX image

Figure B.5: STEM images of Ni/CeO_2-10-O.

B.3 | XRD

Table B.1: XRD Scherrer analysis of the CeO_2 and Ni phases in Ni/CeO_2 catalysts: FWHM, 2θ peak position, and crystallite size.

CeO_2 phase (Lorentz peak fit)

Catalyst	FWHM (°)	2θ (°)	Particle Size (nm)	Method
Ni/CeO_2-10-O	0.795	28.583	10.8	
Ni/CeO_2-20-O	0.436	28.692	19.6	
Ni/CeO_2-29-O	0.300	28.628	28.5	Lorentz
Ni/CeO_2-15-O	0.564	28.662	15.2	
Ni/CeO_2-23-O	0.381	28.558	22.5	

Ni phase (Gauss peak fit)

Catalyst	FWHM (°)	2θ (°)	Particle Size (nm)	Method
Ni/CeO_2-29-O	1.116	42.972	8.0	
Ni/CeO_2-10-O	1.697	42.990	5.3	
Ni/CeO_2-20-O	1.838	42.374	4.8	Gauss
Ni/CeO_2-15-O	1.697	43.344	5.3	
Ni/CeO_2-23-O	1.345	43.169	6.6	

Table B.2: XRD Scherrer analysis of the CeO_2 and Ni phases in Ni/CeO_2 catalysts calcined at 350 °C: FWHM, 2θ peak position, and crystallite size.

CeO_2 phase (PsdVoigt2 peak fit)

Catalyst	FWHM (°)	2θ (°)	Particle Size (nm)	Method
Ni/CeO_2-9-O-350	0.916	28.701	9.3	PsdVoigt2
Ni/CeO_2-17-O-350	0.516	28.573	16.6	
Ni/CeO_2-20-O-350	0.419	28.643	20.4	
Ni/CeO_2-30-O-350	0.285	28.541	29.9	

Ni phase (Gaussian peak fit)

Catalyst	FWHM (°)	2θ (°)	Particle Size (nm)	Method
Ni/CeO_2-9-O-350	—[a]	—[a]	—[a]	Gaussian
Ni/CeO_2-17-O-350	—[a]	—[a]	—[a]	
Ni/CeO_2-20-O-350	1.655	43.481	5.4	
Ni/CeO_2-30-O-350	0.854	43.253	10.5	

[a] Ni crystallites too small for reliable XRD analysis; signal-to-noise ratio insufficient for peak fitting.

Table B.3: XRD Scherrer analysis of the CeO_2 and Ni phases in Ni/CeO_2 catalysts of varying morphology: FWHM, 2θ peak position, and crystallite size.

CeO_2 phase (Lorentz peak fit)

Catalyst	FWHM (°)	2θ (°)	Particle Size (nm)	Method
Ni/CeO_2-9-O	0.908	28.580	9.4	Lorentz
Ni/CeO_2-15-C	0.558	28.539	15.3	
Ni/CeO_2-20-C	0.428	28.759	20.0	
Ni/CeO_2-9-S	0.981	28.824	8.7	
Ni/CeO_2-11-S	0.879	28.706	9.7	

Ni phase (Gauss peak fit)

Catalyst	FWHM (°)	2θ (°)	Particle Size (nm)	Method
Ni/CeO_2-9-O	1.697	42.990	5.3	Gauss
Ni/CeO_2-15-C	0.302	43.354	29.5	
Ni/CeO_2-20-C	0.929	42.926	9.6	
Ni/CeO_2-9-S	—[a]	—[a]	—[a]	
Ni/CeO_2-11-S	—[a]	—[a]	—[a]	

[a] Ni crystallites too small for reliable XRD analysis; signal-to-noise ratio insufficient for peak fitting.

B.4 | ICP-OES

Table B.4: ICP-OES results for Ni loading on Ni/CeO_2 catalysts of varying CeO_2 particle size.

Sample	Nominal Ni (wt%)	Ni 1 (wt%)	Ni 2 (wt%)	Ni 3 (wt%)	Mean Ni (wt%)
Ni/CeO_2-29-O	10	8.54	8.51	8.64	8.56
Ni/CeO_2-23-O	10	9.02	8.99	9.07	9.03
Ni/CeO_2-20-O	10	10.26	10.24	10.33	10.28
Ni/CeO_2-15-O	10	8.94	8.94	9	8.96
Ni/CeO_2-9-O	10	9.09	9.08	9.21	9.13

B.5 | CO Chemisorption

Table B.5: CO chemisorption results for the Ni/CeO_2 particle size series: Ni dispersion, average particle size, and surface Ni content ($M_{Ni} = 58.09$ g/mol). Dispersion uses 1.5:1 assumption for Ni:CO. Values in parentheses denote one standard deviation.

Catalyst	CO chemisorbed ($mmol_{CO}/g$)	Dispersion (%) ($\pm$ std)	Particle Size (nm) ($\pm$ std)	n_{Ni} (mol_{Ni}/g)
Ni/CeO_2-29-O	0.143 ± 0.002	15 ± 0.2	6.6 ± 0.1	2.15×10^{-4}
Ni/CeO_2-23-O	0.249 ± 0.004	24 ± 0.4	4 ± 0.1	3.74×10^{-4}
Ni/CeO_2-20-O	0.311 ± 0.004	27 ± 0.3	3.6	4.67×10^{-4}
Ni/CeO_2-15-O	0.265 ± 0.004	26 ± 0.4	3.7 ± 0.1	3.97×10^{-4}
Ni/CeO_2-9-O	0.250 ± 0.002	24 ± 0.2	4	3.76×10^{-4}

Table B.6: Calculated Ni surface site density based on Ni-CeO_2 interfacial site, assuming hemispherical Ni particles supported on CeO_2 [36, 37].

Sample	d (nm)	n_{Ni} [a] (mol_{Ni}/g)	V_p [b] (cm^3)	m_p [c] (g)	N_p [d]	L_p [e]	L_{tot} [f]	N_{site} [g]	n_{site} [h] (mol_{site}/g_{cat})
Ni/CeO_2-29-O	6.6	2.15×10^{-4}	1.51×10^{-19}	1.35×10^{-18}	6.38×10^{16}	20.768	1.33×10^{18}	5.32×10^{18}	8.55×10^{-6}
Ni/CeO_2-23-O	4.0	3.74×10^{-4}	3.32×10^{-20}	2.96×10^{-19}	3.05×10^{17}	12.532	3.82×10^{18}	1.53×10^{19}	2.47×10^{-5}
Ni/CeO_2-20-O	3.6	4.67×10^{-4}	2.53×10^{-20}	2.26×10^{-19}	4.56×10^{17}	11.448	5.22×10^{18}	2.10×10^{19}	3.37×10^{-5}
Ni/CeO_2-15-O	3.7	3.97×10^{-4}	2.72×10^{-20}	2.42×10^{-19}	3.70×10^{17}	11.721	4.34×10^{18}	1.74×10^{19}	2.80×10^{-5}
Ni/CeO_2-9-O	4.0	3.76×10^{-4}	3.39×10^{-20}	3.02×10^{-19}	3.02×10^{17}	12.617	3.81×10^{18}	1.53×10^{19}	2.46×10^{-5}

[a] Molar Ni content per gram of catalyst, n_{Ni}, from CO chemisorption.

[b] Volume of a single hemispherical Ni particle: $V_p = \frac{\pi}{6} d_{Ni}^3 \times 10^{-21}$ cm^3, with d_{Ni} in nm.

[c] Mass of a single Ni particle: $m_p = \rho_{Ni} V_p$, with $\rho_{Ni} = 8.908$ g/cm^3 [37].

[d] Number of Ni particles per gram of catalyst: $N_p = \frac{n_{Ni} M_{Ni} \chi_{Ni}}{m_p}$, where $M_{Ni} = 58.69$ g/mol and χ_{Ni} is the actual Ni weight fraction per gram of catalyst.

[e] Perimeter (edge) Ni atom count per particle, obtained from the nearest-neighbour coordination factor $\alpha_{NN} = 0.2492$ [36]: $L_p = \frac{1}{\alpha_{NN}(NN)}$.

[f] Total perimeter Ni atom count per gram of catalyst: $L_{tot} = L_p \times N_p$.

[g] Number of active (edge) Ni sites per gram of catalyst: $N_{site} = \frac{L_{tot} \rho_{site}}{g_{cat}}$, where ρ_{site} is the Ni surface site density.

[h] Molar Ni site density: $n_{site} = \frac{N_{site}}{N_A}$, with $N_A = 6.022 \times 10^{23}$ mol^{-1} [37].

Table B.7: CO chemisorption results for the Ni/CeO_2 morphology series: Ni dispersion, average particle size, and surface Ni content ($M_{Ni} = 58.69$ g/mol). Values in parentheses denote one standard deviation.

Catalyst	Y-intercept	Dispersion (%) ($\pm$ std)	Particle Size (nm) ($\pm$ std)	n_{Ni} (mol_{Ni}/g)
Ni/CeO_2-9-O	0.250 ± 0.002	22 ± 0.2	4.4 ± 0.0	3.76×10^{-4}
Ni/CeO_2-15-C	0.158 ± 0.005	14 ± 0.5	7.0 ± 0.2	2.36×10^{-4}
Ni/CeO_2-9-S	0.208 ± 0.004	18 ± 0.3	5.3 ± 0.1	3.11×10^{-4}

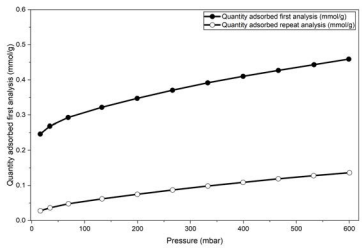

(a) Ni/CeO_2-9-O

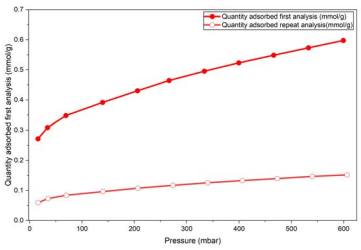

(b) Ni/CeO_2-15-O

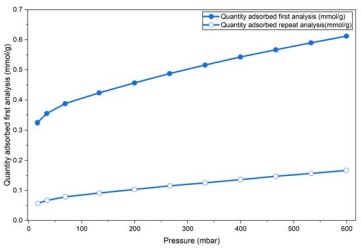

(c) Ni/CeO_2-20-O

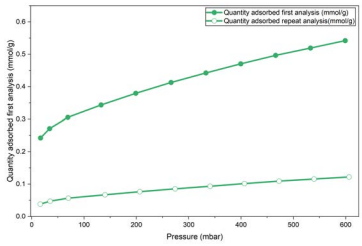

(d) Ni/CeO_2-23-O

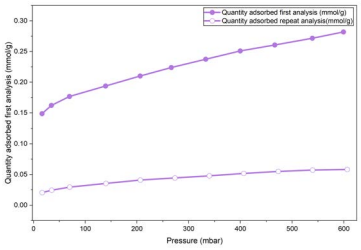

(e) Ni/CeO_2-29-O

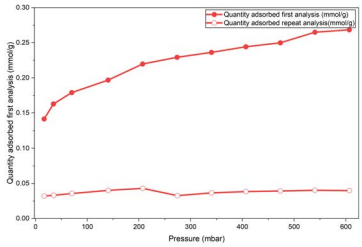

(f) Ni/CeO_2-15-C

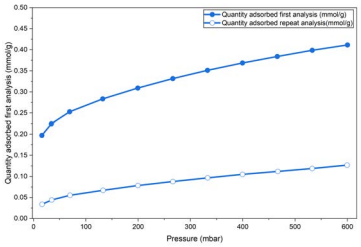

(g) Ni/CeO_2-9-S

Figure B.6: CO chemisorption isotherms (first and repeat analysis) for all Ni/CeO_2 catalysts. The difference between the first and repeat adsorption gives the chemisorbed quantity used to determine Ni dispersion and particle size.

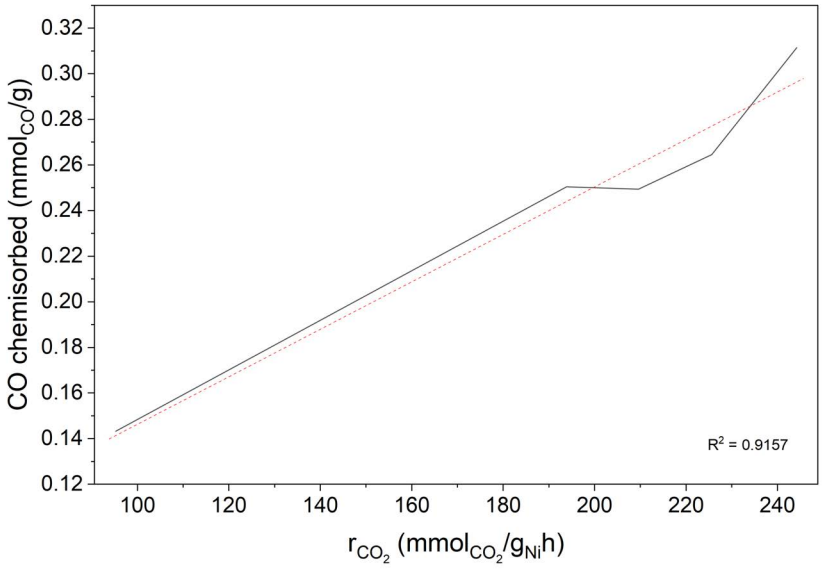

Figure B.7: Correlation using linear regression of CO chemisorbed to CO_2 activity.

B.6 | XPS

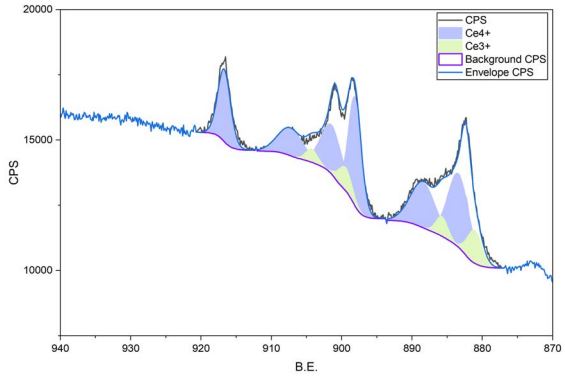

(a) 9-O unreduced (Ce 3d)

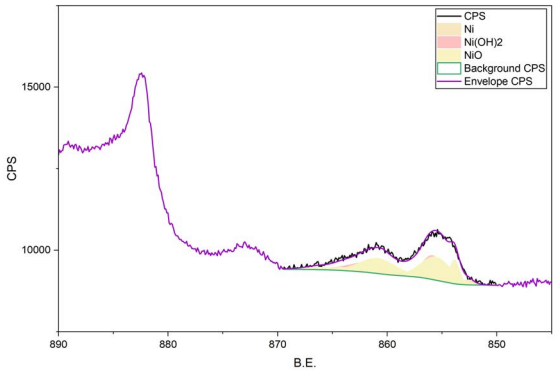

(b) 9-O unreduced (Ni 2p)

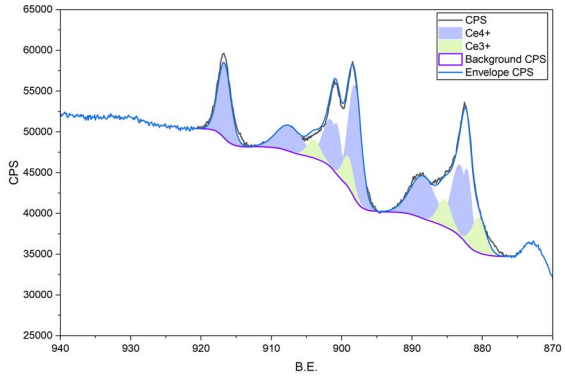

(c) 20-O unreduced (Ce 3d)

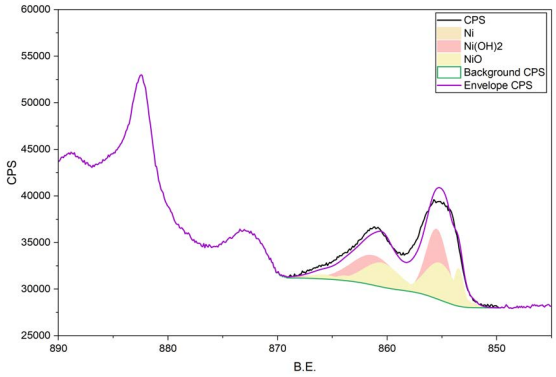

(d) 20-O unreduced (Ni 2p)

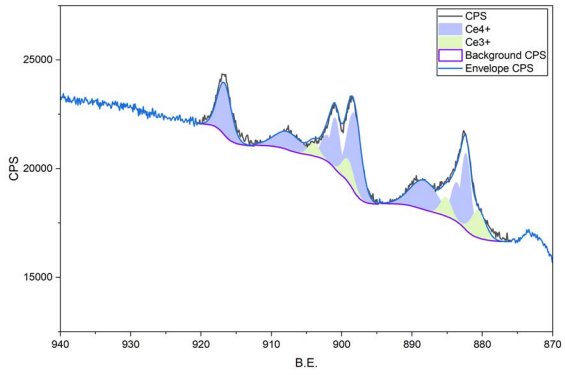

(e) 29-O unreduced (Ce 3d)

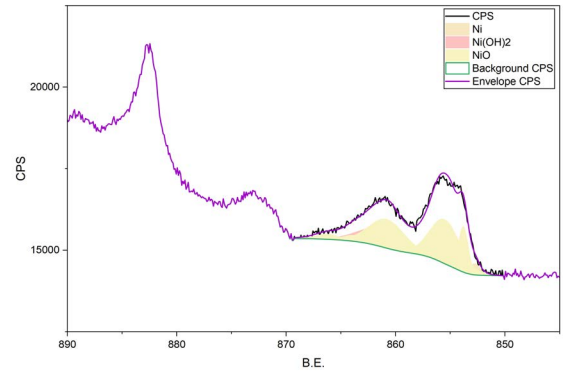

(f) 29-O unreduced (Ni 2p)

Figure B.8: XPS spectra of unreduced Ni/CeO_2 catalysts for all CeO_2 particle sizes. Left column: Ce 3d region; right column: Ni 2p region. Top to bottom: 9-O (smallest), 20-O (medium), 29-O (largest).

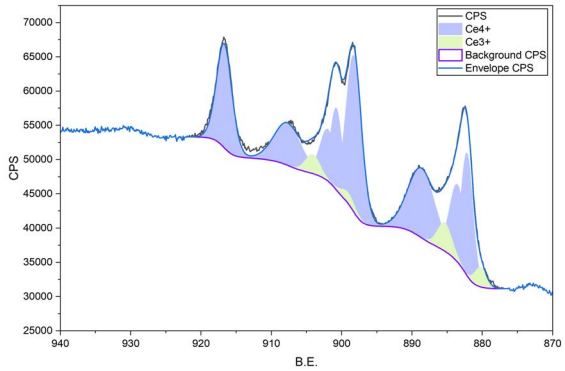

(a) 9-O reduced (Ce 3d)

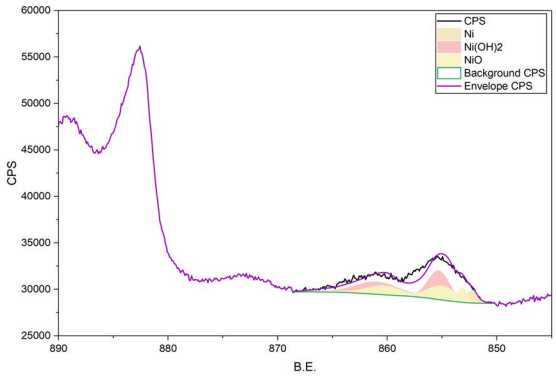

(b) 9-O reduced (Ni 2p)

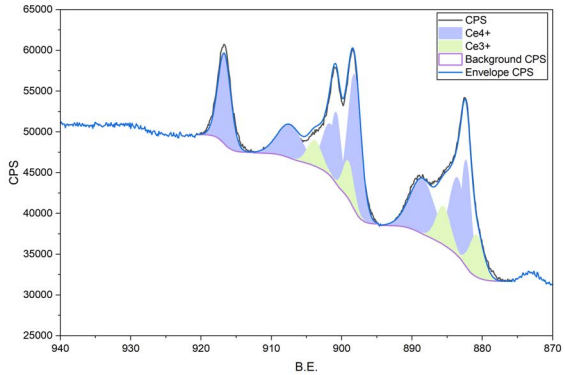

(c) 20-O reduced (Ce 3d)

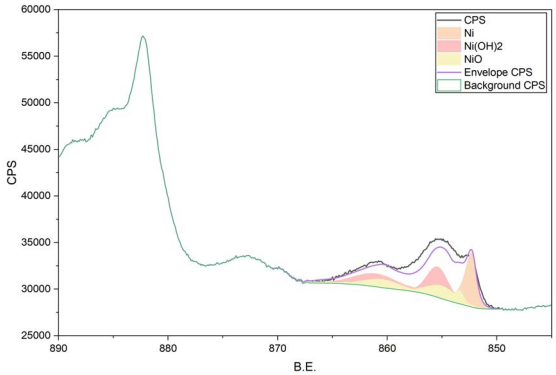

(d) 20-O reduced (Ni 2p)

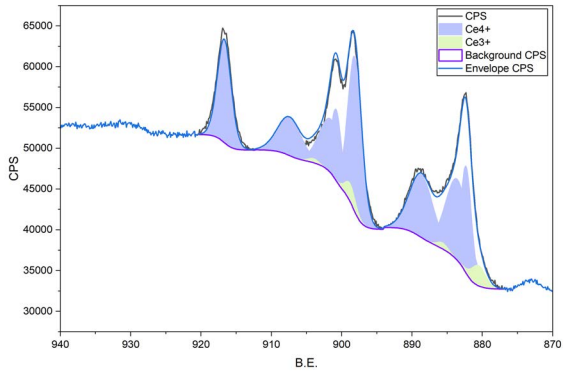

(e) 29-O reduced (Ce 3d)

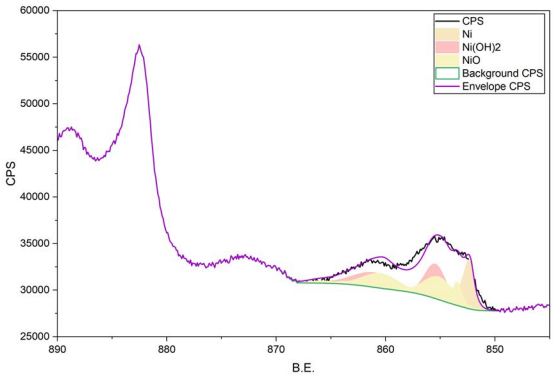

(f) 29-O reduced (Ni 2p)

Figure B.9: XPS spectra of reduced Ni/CeO_2 catalysts for all CeO_2 particle sizes (calcination at 400 °C). Left column: Ce 3d region; right column: Ni 2p region. Top to bottom: 9-O (smallest), 20-O (medium), 29-O (largest).

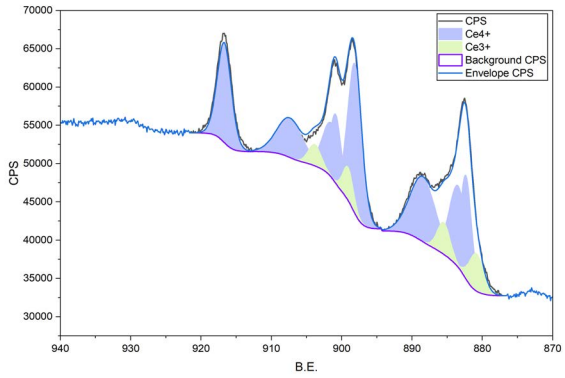

(a) 20-O reduced, 350 °C (Ce 3d)

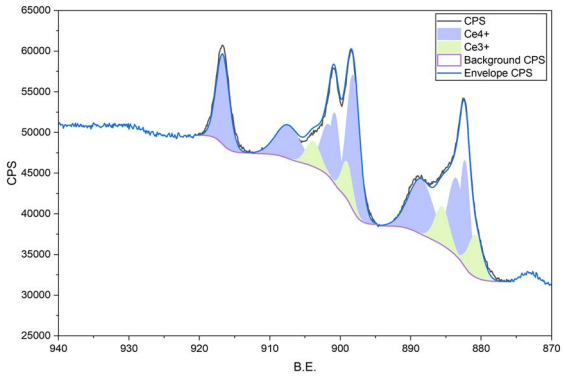

(b) 20-O reduced, 400 °C (Ce 3d)

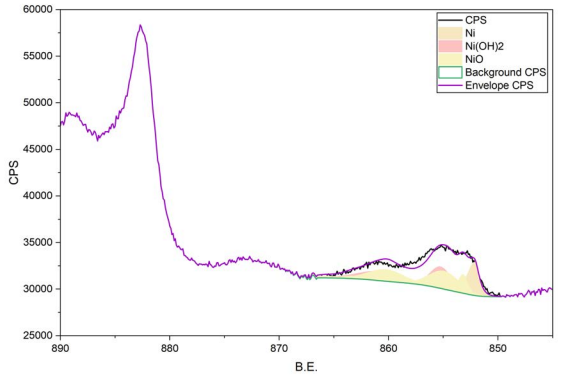

(c) 20-O reduced, 350 °C (Ni 2p)

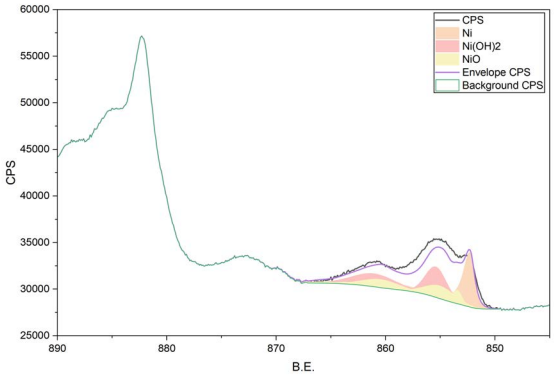

(d) 20-O reduced, 400 °C (Ni 2p)

Figure B.10: Effect of calcination temperature on the XPS spectra of reduced Ni/CeO_2-20-O. Left column: calcined at 350 °C; right column: calcined at 400 °C. Top row: Ce 3d region; bottom row: Ni 2p region.

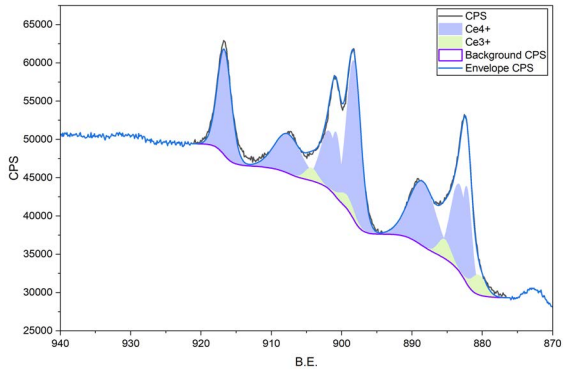

(a) 9-O unreduced (Ce 3d)

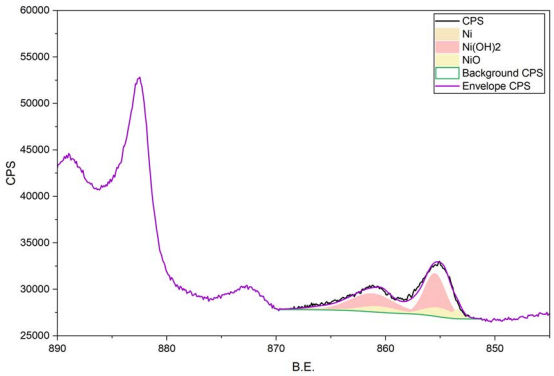

(b) 9-O unreduced (Ni 2p)

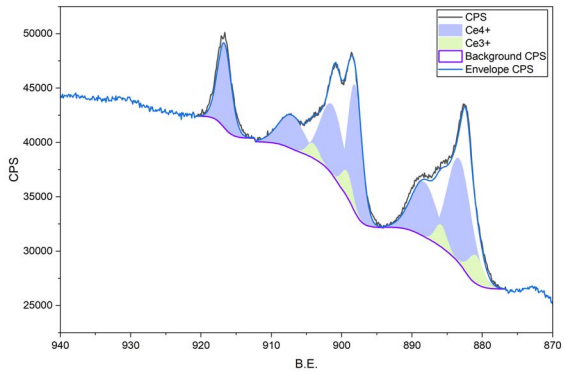

(c) 15-C unreduced (Ce 3d)

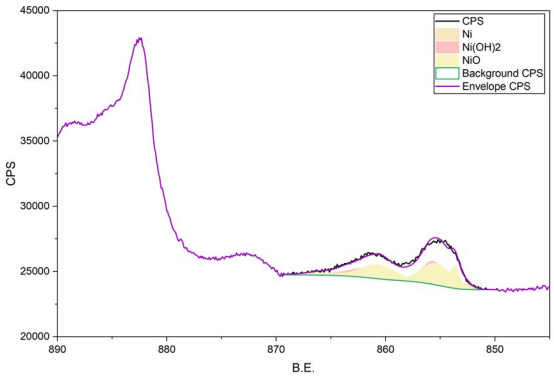

(d) 15-C unreduced (Ni 2p)

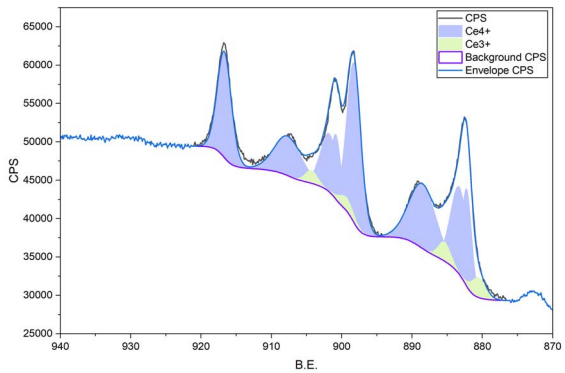

(e) 9-S unreduced (Ce 3d)

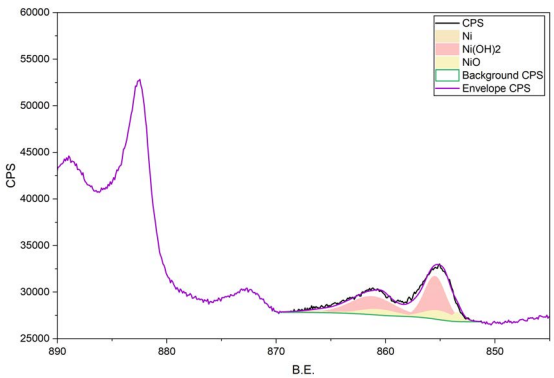

(f) 9-S unreduced (Ni 2p)

Figure B.11: XPS spectra of unreduced Ni/CeO_2 catalysts for samples 9-O, 15-C, and 9-S. Left column: Ce 3d region; right column: Ni 2p region. Top to bottom: 9-O, 15-C, 9-S.

B.7 | FTIR

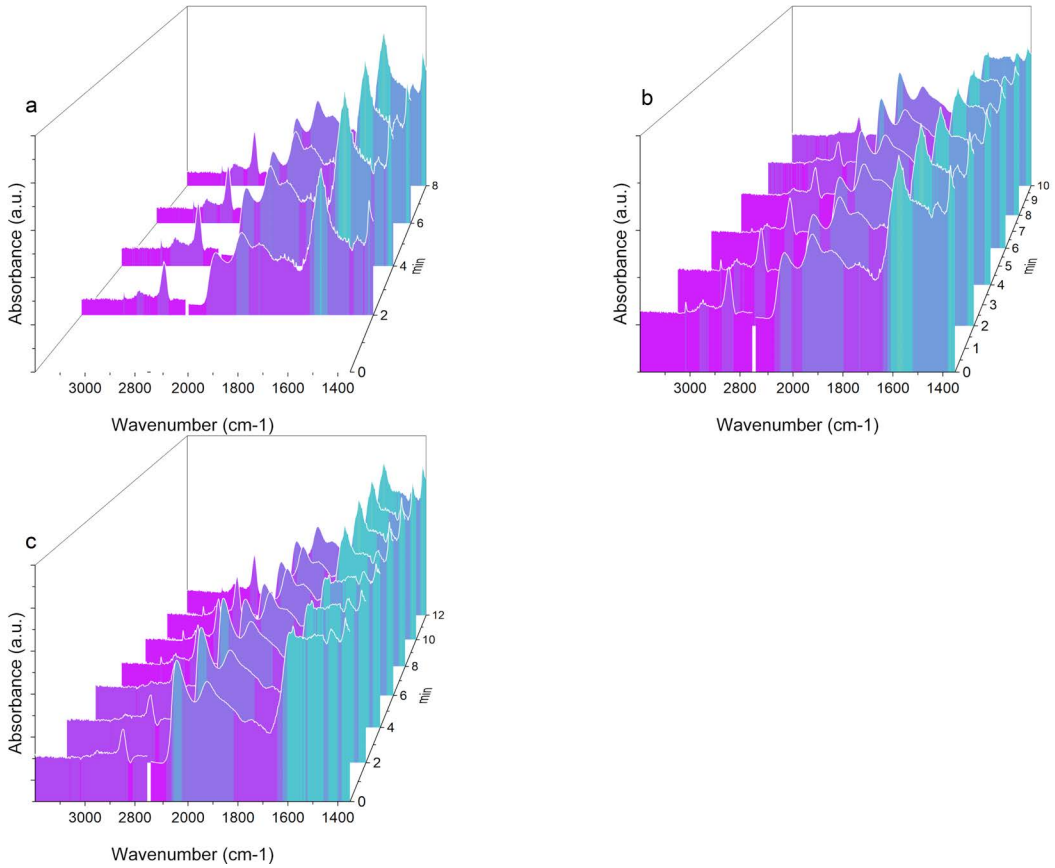

Figure B.12: FTIR of switching of (a) H_2/H_2+CO_2, (b) H_2+CO_2/CO_2, and (c) CO_2/H_2+CO_2 consumed of Ni/CeO_2-9-O

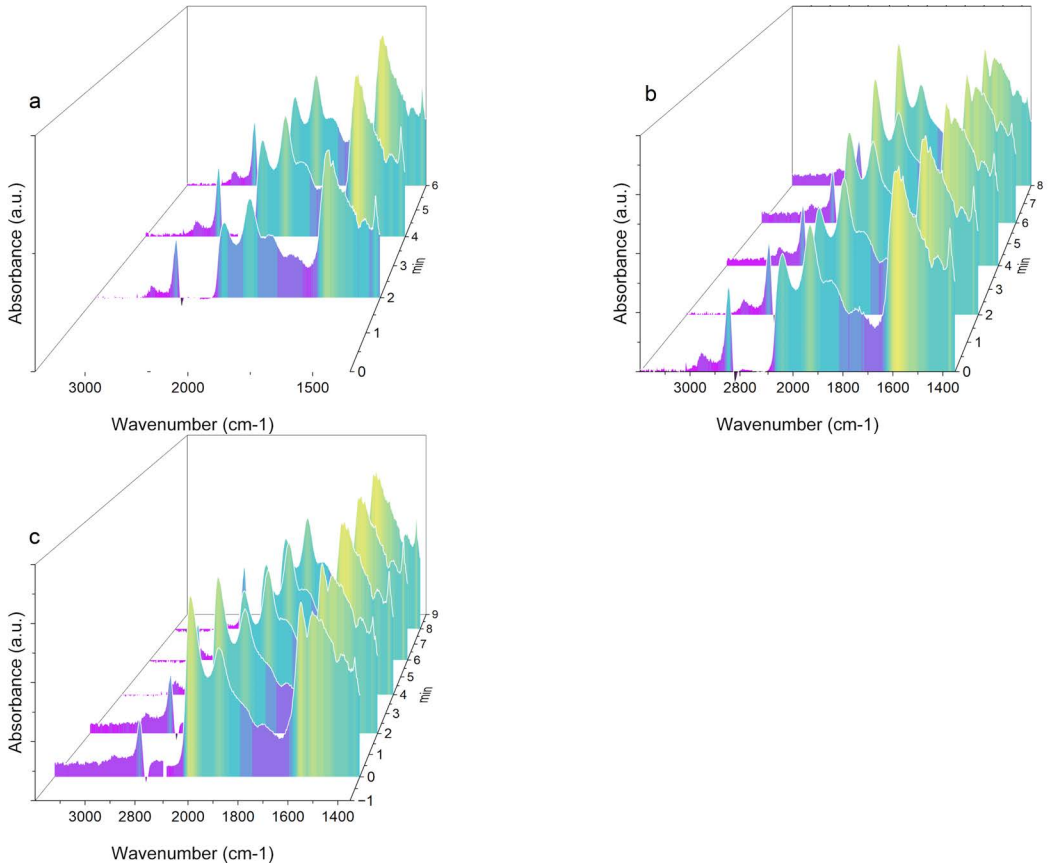

Figure B.13: FTIR of switching of (a) H_2/H_2+CO_2, (b) H_2+CO_2/CO_2, and (c) CO_2/H_2+CO_2 consumed of Ni/CeO_2-15-O

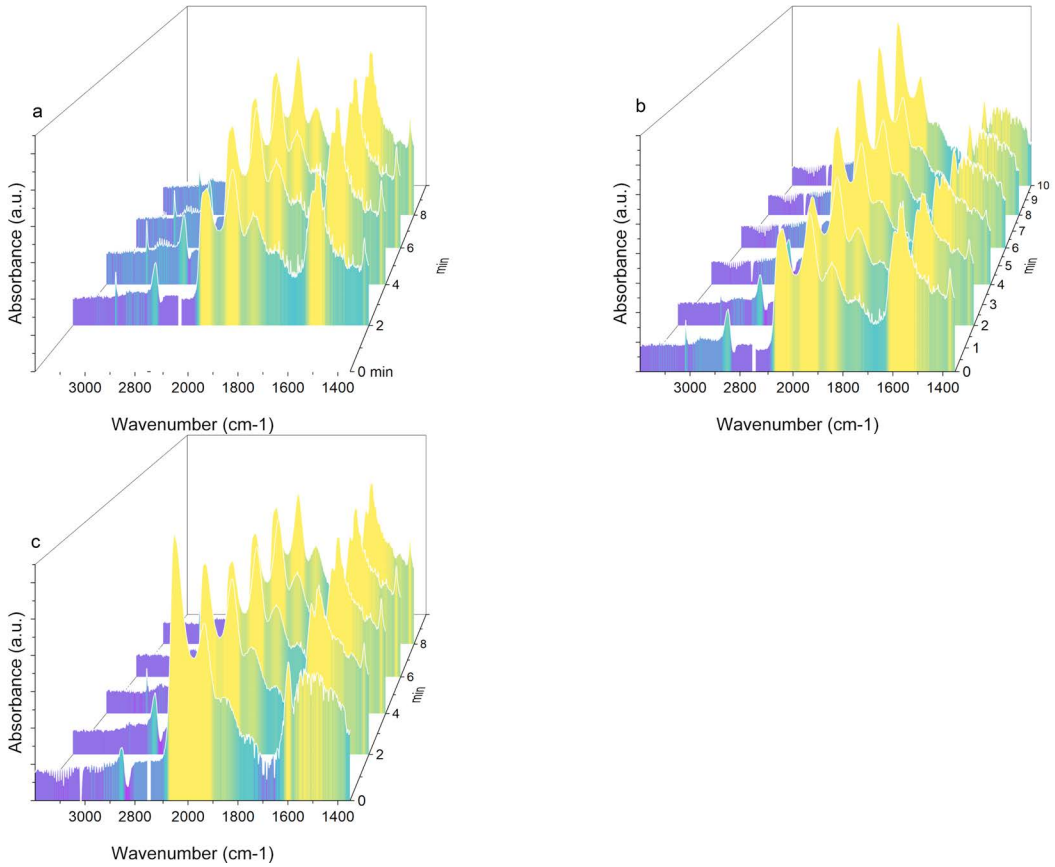

Figure B.14: FTIR of switching of (a) H_2/H_2+CO_2, (b) H_2+CO_2/CO_2, and (c) CO_2/H_2+CO_2 consumed of Ni/CeO_2-20-O

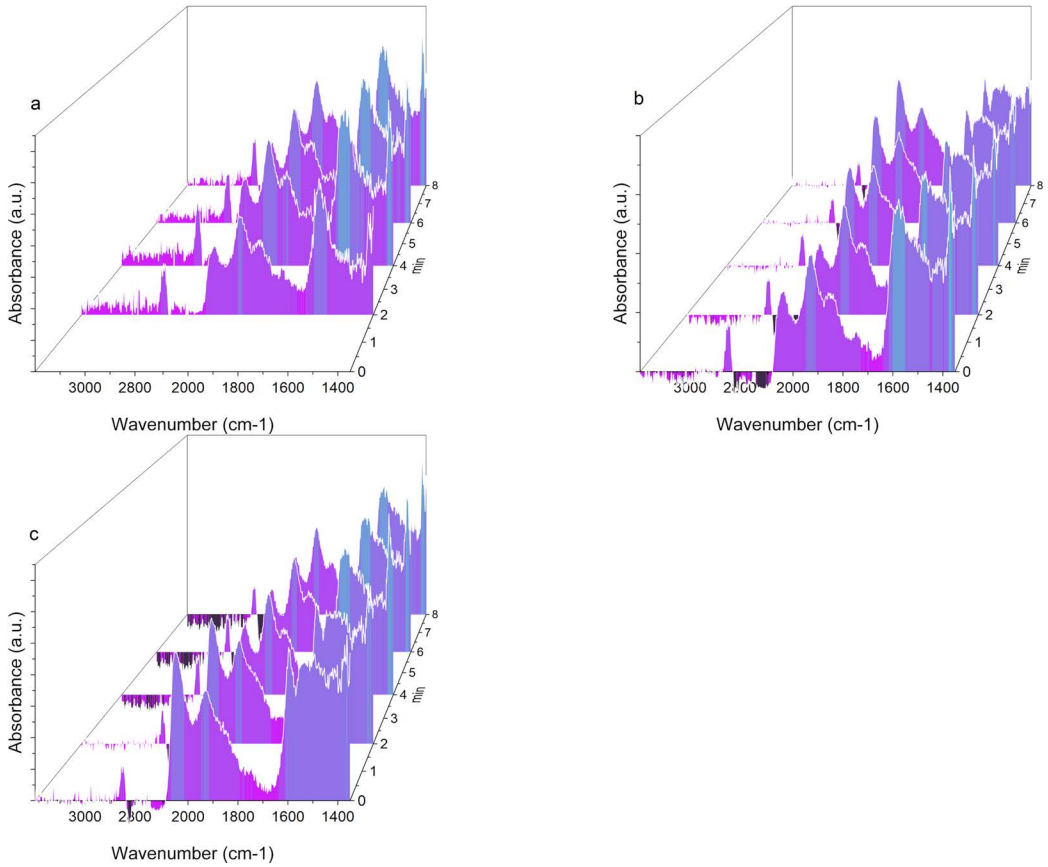

Figure B.15: FTIR of switching of (a) H_2/H_2+CO_2, (b) H_2+CO_2/CO_2, and (c) CO_2/H_2+CO_2 consumed of Ni/CeO_2-23-O

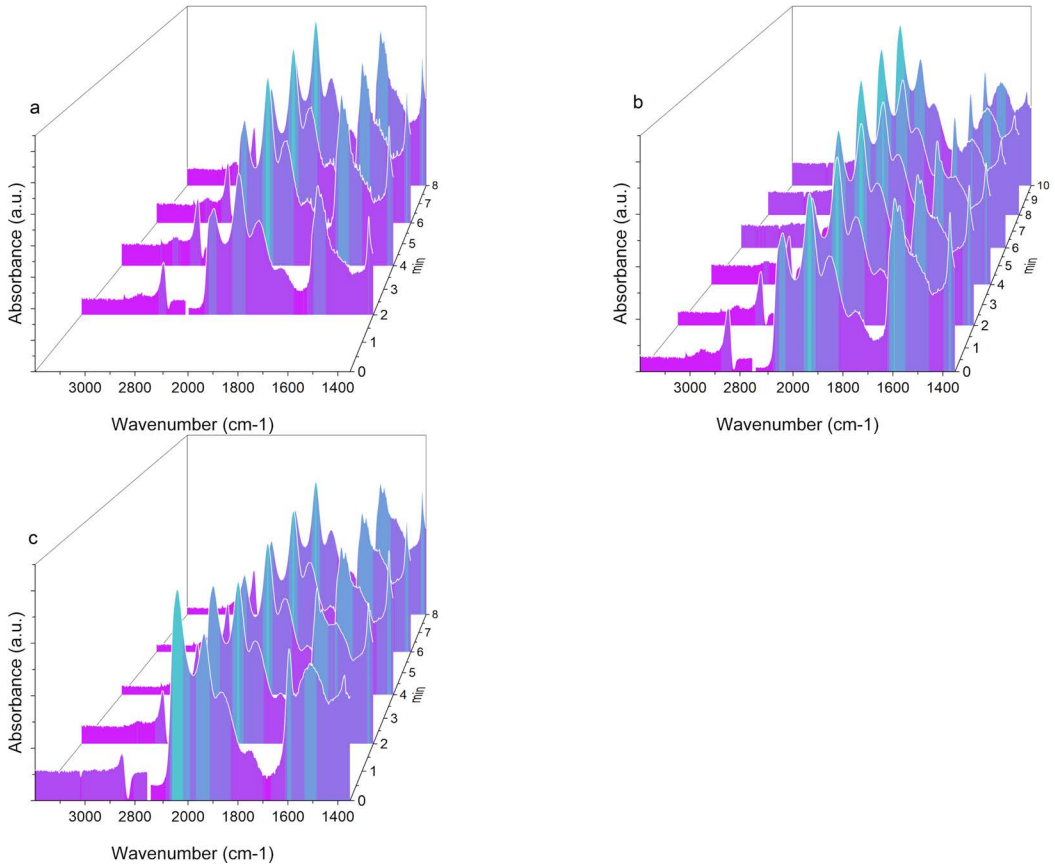

Figure B.16: FTIR of switching of (a) H_2/H_2+CO_2, (b) H_2+CO_2/CO_2, and (c) CO_2/H_2+CO_2 consumed of Ni/CeO_2-29-O

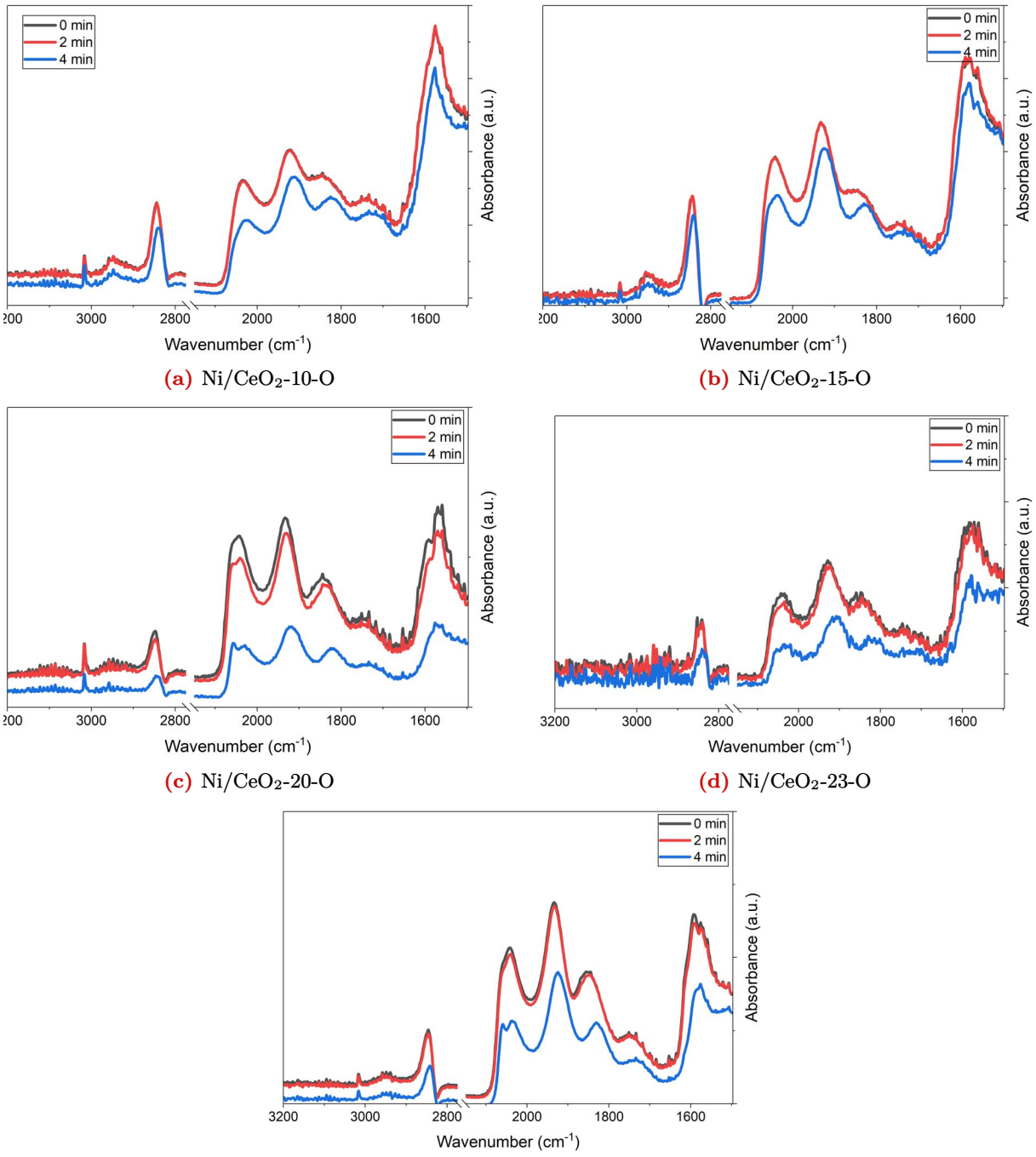

(a) Ni/CeO_2-10-O

(b) Ni/CeO_2-15-O

(c) Ni/CeO_2-20-O

(d) Ni/CeO_2-23-O

(e) Ni/CeO_2-29-O

Figure B.17: FTIR of switching of H_2+CO_2/H_2 of Ni/CeO_2-O catalysts.